Plasmonic Colour Filtering: From Fundamental Principles to Practical Applications

Catherine Sadatnajafi B.S, M.S

This thesis is presented in total fulfilment of the requirements for the degree of

Doctor of Philosophy

College of Science, Health and Engineering

Department of Chemistry and Physics

La Trobe University

Victoria, Australia

November 2020

DECLARATION

"This thesis includes work by the author that has been published or accepted for publication as described in the text. Except where reference is made in the text of the thesis, this thesis contains no other material published elsewhere or extracted in whole or in part from a thesis accepted for the award of any other degree or diploma. No other person's work has been used without due acknowledgment in the main text of the thesis. This thesis has not been submitted for the award of any degree or diploma in any other tertiary institution."

Catherine Sadatnajafi

November 2020

LIST OF PUBLICATIONS

Balaur, E., **C. Sadatnajafi**, S. S. Kou, J. Lin and B. Abbey (2016). "Continuously tunable, polarization controlled, colour palette produced from nanoscale plasmonic pixels." Scientific reports **6**: 28062.

Balaur, E., **C. Sadatnajafi**, D. Langley and B. Abbey (2016). Optimisation of polarization controlled colour tuning using nanoscale cross-shaped apertures in silver films. SPIE BioPhotonics Australasia, International Society for Optics and Photonics.

Balaur, E., **C. Sadatnajafi**, D. Langley, J. Lin, S. S. Kou and B. Abbey (2015). Electron-beam induced diamond-like-carbon passivation of plasmonic devices. Micro+ Nano Materials, Devices, and Systems, International Society for Optics and Photonics.

Langley, D., E. Balaur, **C. Sadatnajafi** and B. Abbey (2016). Dual pitch plasmonic devices for polarization enhanced colour based sensing. SPIE BioPhotonics Australasia, International Society for Optics and Photonics.

Langley, D. P., E. Balaur, Y. Hwang, **C. Sadatnajafi** and B. Abbey (2018). "Optical chemical barcoding based on polarization controlled plasmonic nanopixels." Advanced Functional Materials **28**(4): 1704842.

C. Sadatnajafi, E. Balaur and B. Abbey. "Bimodal plasmonic colour filters enable direct optical imaging of ion implantation in thin films". Advanced Functional Materials. Under review.

ABSTRACT

Plasmonic colour filters are now a well-established technology spanning both optics and solid state physics and utilising the latest tools for fabrication at the nanoscale. The motivation behind using these devices for manipulating light stems from their unique optical properties which cannot be replicated by bulk materials. This new class of 'metamaterials' opens the door to tailoring the optical characteristics of electromagnetic fields through a modification of the size and shape of the sub-structures which make up the devices. Thee research presented within this thesis describes and demonstrates the nanofabrication of arrays of cross-shaped apertures in silver thin-films which constitute 'nanopixles' that act collectively to 'filter' the incident wavefield.

Chapter 3 of this thesis includes a systematic investigation of the performance of plasmonic colour filters fabricated in silver thin films and the relative influence of the underlying device geometry. Chapter 4 meanwhile investigates the long-term stability of silver plasmonic devices and the use of Diamond-like-Carbon as a cheap, reliable, and effective means of passivating the surface of silver plasmonic devices. The modification of the structural and electronic properties of thin-films via implantation is a major area of research in a number of areas including the electronics industry. In Chapter 5 we investigate Ga ion implantation in TiO_2 thin films and look at the characterisation of the implanted layers optoelectronic properties. Finally, in Chapter 6 the use of bimodal plasmonic colour filters in combination with microfluidics for chemical sensing is investigated using self-assembled monolayers (SAMs). We find that these devices are passively able to detect changes in the extent of the SAM owing to their sensitivity to changes in the local dielectric properties of the surrounding media.

ACKNOWLEDGMENTS

First and foremost, this research project would not have been possible if it were not for the guidance and encouragement of my supervisor, the wonderful Dr Eugeniu Balaur for his great support and critical role. Dr Balaur provided me with much needed momentum when I was stagnating also saved me many hours of toil and enabled the prompt complication of this project. Professor Brian Abbe also played a critical role throughout this research. Without the many discussions, diversions and explanations from them, this project would not have succeeded.

A very special thanks go to my lecturers at La Trobe university and my wonderful friend Golrokh Akhgar for her constant encouragement and supports.

I acknowledge the unwavering support and encouragement of my loving husband Abbas. Needless to say, I would not have been in a position to undertake this project if he didn't support me. Your endless patience throughout has underpinned my ability to carry out this project. At the end I take this opportunity to express my profound appreciation and deep regard to my Parents and brother, guidance given by them time to time shall carry me a long way in the journey of life.

TABLE OF CONTENTS

will be reflected. b) for (ω>ω_p) the real part of the dielectric function is positive and for (ω<ω_p) the real part is negative. c) plot describes the role played by the dielectric function in determining the oscillation of conduction electrons as a function of the frequency of the incident light. Figure adapted from Ref [35].

Figure 2.2 *Localised Surface Plasmon (LSP) and Surface Plasmon Polariton (SPP) a) SPPs are EM modes that arise from the interaction between light and the conduction band electrons in a two-dimensional metallic film b) SPP dispersion curve c) Plot showing the SPP angle where prism-coupling is used to generate SPPs d) LSPs are localised EM modes that arise due to geometry confinement e) and f) Scattering and absorption properties for nanoparticles of radius < 15 nm and > 15 nm respectively. The behaviour at the Localised Surface Plasmon Resonance (LSPR) wavelength (λ_{LSPR}) is indicated by the vertical dotted line. Figure adapted from Ref [35].*

Figure 2.3 *Sketches of the oscillating nature of SPPs in a sub-wavelength metallic film with the four key length scales shown. The left-hand side shows the generation of oscillating SPP modes after interaction between incident light with wavevector k_0 and the perforated metallic film. The in-plane wave vector of the SPP along the propagation surface under appropriate boundary conditions gives the SPP wavelength, λspp . The right-hand side of the figure shows the imaginary part of the wavevector for SPP damping in two directions either side of the metal-dielectric interface. The equations describing the penetration (decay length) in the metal (δ_m) and dielectric (δ_d) are given in the two equations in the bottom-right. The sketches also show the SPP mode propagation length i.e. δspp, (top-right equation). Reprinted with permission from Ref [28, 45, 46]*

Figure 2.4 *Schematic of light incident on a metal film perforated by an array of apertures. The surface of the metal is illuminated by a plane wave ($\psi_{PW}^-(k_x)$) which results in 3 distinct components ψ_{SP}^+ , ψ_{SP}^- and ψ_0^- after interaction. The Bloch mode propagates in*

LIST OF TABLES

ACRONYMS

AFM	Atomic force microscopy
ANFF	Australian National Fabrication Facility
ATR	Attenuated total reflection
CVD	Chemical vapour deposition
CPP	Chromatic plasmonic polarizer
DDA	Discrete dipole approximation
DLC	Diamond-like carbon
EBL	Electron Beam Lithography
EM	Electromagnetic
EOT	Extraordinary optical transmission
FIB	Focused Ion Beam
FWHM	Full width at half maximum
FoM	Figure-of-merit
MCN	Melbourne Centre for Nanofabrication
NIL	Nanoimprinting lithography
NIR	Near-infrared region
LSP	Localized Surface Plasmon
LSPR	Localized Surface Plasmon Resonance

P-Pol	P Polarization
PMMA	Polymethyl methacrylate
RI	Refractive Index
SEM	Scanning Electron Microscopy
SNR	Signal-to-noise ratio
S-Pol	S-Polarization
SP	Surface Plasmon
SAM	Self-Assembled Monolayer
SERS	surface-enhanced Raman scattering
SRIM	stopping and range of ions in matter
SPR	Surface Plasmon Resonance
TFE	Thermally assisted field emitter
TE	Transverse Electric
TM	Transverse magnetic
TRIM	Transport of Ion in Matter
QF	Quality factor
UV	Ultraviolet
WA	Wood's anomalies
2D	Two-Dimensional
3D	Three-Dimensional

CHAPTER 1

INTRODUCTION AND FUNDAMENTAL PRINCIPLES
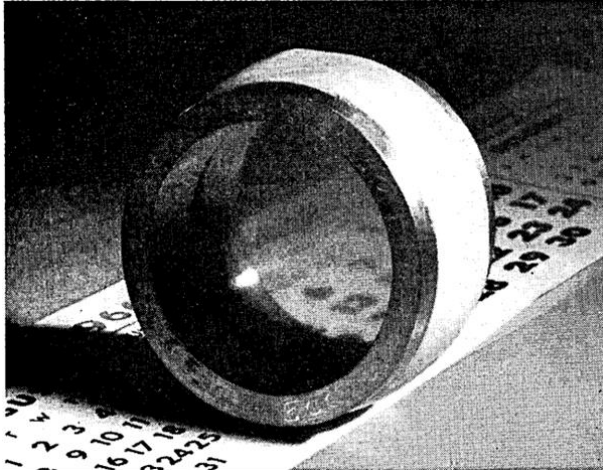
Photograph of the first metallic mesh filter array for visible light built in 1962 by Rawcliffe and Randall. The filter consisted of 250-1000 wire meshes per inch carefully cemented onto a ring. Figure adapted from reference[1].

1. INTRODUCTION

The last few decades has seen a revolution in nanotechnology underpinned by quantum mechanics and driven by technological advances in fabrication at the nanoscale [2]. The physical behaviour of nanoparticles and nanosized structures tends to be different from that of bulk materials owing to the significant increase in the ratio of surface area to volume. Recent developments in the field of nanofabrication such as the introduction of Electron Beam Lithography (EBL), Focused Ion Bram (FIB), and nanoimprinting have opened up new avenues for creating bespoke structures at the nanoscale. These structures can in turn be used to generate phenomena such as Surface Plasmon Resonance (SPR) and Extraordinary Optical Transmission (EOT). SPR describes the resonant interaction of light with free electrons, typically at a metal-dielectric interface [3]. The interaction between light and SPR mediated by sub-wavelength structures in thin films was investigated for the

first time during the 1990s. In 1999 it was experimentally demonstrated by Ebbesen et al. that transmission of light through an array of sub-wavelength apertures is greater than that predicted by classical optics. This was the first reported observation of EOT through thin metal films and has since gone on to be exploited for wide range of different applications [4, 5]. Two of the most common applications reported for devices exhibiting EOT phenomena are colour filtering and chemical sensing [6-10].

The use of nanoapertures as the basis for a chemical sensor offers a number of advantages including high-sensitivity and the ability to be miniaturised. As nanofabrication techniques have continued to advance more complex apertures and structures have been produced resulting in more highly effective manipulation of the EOT phenomenon. The optical and electronic properties of plasmonic devices depend on a number of factors including geometry and the choice of materials. Another critical factor affecting performance is the long-term stability as well as the biocompatibility of plasmonic arrays which needs to be considered when engineering plasmonic devices [8-10].

1.1 The influence of material choice

The properties of the materials used to construct optical plasmonic devices play a significant role in its final performance. The existence of SPR at the interfaces within plasmonic devices depends on the fact that one of the materials at the interface has a negative permittivity. This property is characteristic of metals and semiconductors. Pure metals such as silver and gold are the traditional candidates for plasmonic nanostructures owing to the large number of free electrons. Figure 1.1 shows plots of the real and imaginary parts of the dielectric functions of some common conductive materials used to make plasmonic devices.
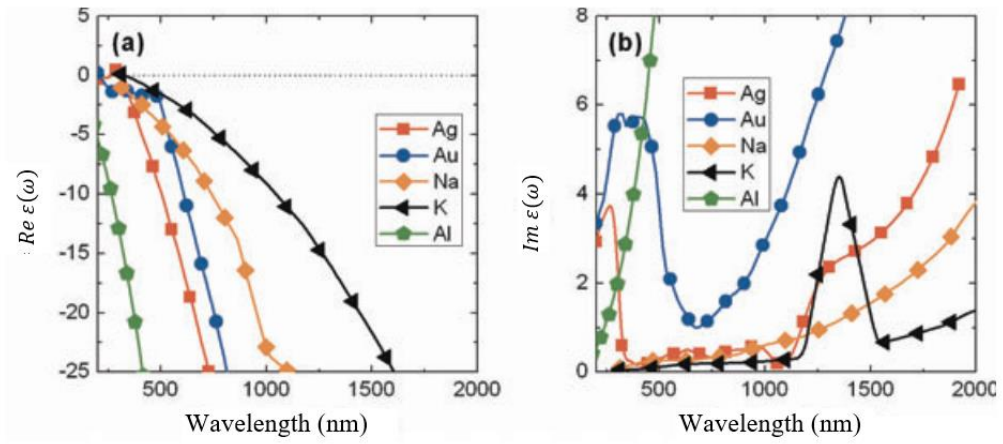
Figure 1.1 *a) Real and b) imaginary parts of the dielectric functions of silver, gold, sodium, potassium, and aluminium. Below 207 nm and 326 nm the value of the real part of the dielectric function for gold and silver are positive whereas above these values it is negative. However, for aluminium, it is negative in that range (UV-Blue). What is striking in these plots is the dramatic decrease in the imaginary component of Ag, Na and K for wavelengths longer than the blue regions of the spectrum. Gold shows a sharp drop in the imaginary component at around 600-750 nm. Adapted from ref [11].*

We see in Figure 1.1 that Au has better performance as a plasmonic device in the Near-Infrared (NIR) region because of its higher negative refractive index. This results in a larger amplitude for the SPR peaks (enhanced local-field) for Au within the NIR region. As a result, Au has been used extensively for surface-enhanced Raman scattering (SERS) [12], nanoscopy [13], Localized Surface Plasmon Resonance (LSPR) sensing, and plasmon waveguides within the infrared regime [14-17]. By contrast, Ag has been used extensively in the visible range for applications including as colour filters [18]. Besides differences in cost, there are several other significant differences between Au and Ag as materials for plasmonic devices. These include the fact that although Ag has superior performance in the visible range it degrades much more quickly in air than Au [19]. Additionally, the thickness

threshold for fabricating a uniform Au film is only around 1.5-7 nm, whereas it is around 12-23 nm for Ag [18, 20]. Platinum and palladium are also potential candidates as alternative metals for plasmonic devices, owing to their catalytic activity which makes them useful for certain chemical sensing applications [21, 22].

After Au, Cu has the best conductivity and exhibits plasmonic resonances at around 600-750 nm within the visible range. Therefore, it is sometimes used as an alternative to Au due to its significantly lower cost. However, the surface of Cu rapidly oxidises in air, which results in challenges during the fabrication processes. Because only oxide-free material exhibits very sharp and narrow SPR resonant peak, the copper surface needs to be covered by a thin protective layer [23].

Along with Ag and Au, it is alkali metals which have the most active free-electron behaviour and relatively low losses (energy dissipation) making them viable candidates as plasmonic devices. In terms of plasmonic losses Na and K are even better candidates as plasmonic materials than Ag and Au. However, due to their extreme reactivity in pure elemental form they have, thus far, been largely considered only from a theoretical standpoint [23].

Aluminium is another material which has been considered for plasmonic applications, however, although it offers advantages in terms of cost, it also exhibits relatively large plasmonic losses for much of the visible range. The inter-band transition in Al is a significant contributory factor increasing the imaginary component of aluminium's dielectric constant within the visible and NIR range which impacts its performance. However, Al is one of the best materials in the UV and blue range (even better than Ag and Au) because of its high negative value in that range [24, 25].

1.2   The influence of device geometry

Localised Surface Plasmon (LSP) polaritons are generated via the resonant interaction of light with individual nanoapertures or nanoparticles, EOT meanwhile, involves the collective interaction of multiple nanoapertures fabricated in a thin metallic film. The maximum amount of transmission is achieved when the nanoapertures are arrayed periodically. The transmission spectrum for such structures which is formed as a result of both LSPs and SPs is extremely sensitive to changes in the local dielectric properties of the surrounding medium. The performance of these structures as sensors depends on how well-defined the plasmon resonance peaks are and their full-width-at-half-maximum (FWHM). However, detection of changes to the transmission spectrum depends not only on the Figure-of-Merit (FOM) for the devices but also on the characteristics of the instrument used to measure the spectra. The influence of aperture shape and structure (termed the 'shape-effect' here) on the optical properties of plasmonic devices for some of the most common aperture shapes is summarised in section 1.2.1 below.

1.2.1 Effect of aperture shape

Due to their ease of fabrication circular apertures aligned in periodic arrays are the most common type of plasmonic colour filter. Circular apertures are able to efficiently convert electromagnetic radiation into SP resonances because they readily satisfy the requirements for momentum coupling. In spite of their ability to easily generate plasmons and the simplicity of the design circular apertures also have several limitations. The first is that they are not inherently sensitive to polarised light which reduces the options available for tailoring the output of the devices. Plasmonic devices based on circular apertures are also very sensitive to variations in the hole diameter to periodicity ratio which can occur due to small errors in fabrication. For example, for a given periodicity if the size of the apertures increases slightly a redshift in the transmitted light

is observed whilst if the size of the apertures decreases slightly the peaks are blue shifted [26]. In contrast to circular apertures which exhibit poor EOT properties when isolated, ring-shaped (annular) apertures can be used as waveguides with excellent SP mediated transmission [27-29].

Optical transmission through elliptical and circular nanoapertures differs not only in terms of their transmission but also in terms of their sensitivity to the polarisation of the incident light. When using elliptically shaped nanoapertures a dramatic change in the main transmission peak is observed when changing from p to s-polarized light. The response of elliptical nanoapertures to polarised light has been studied by monitoring their transmitted intensity as a function of the incident polarisation vector. The p and s polarisation transmission ratio are a function of the ellipse aspect ratio (ratio of the major and minor axis dimeters); a squared dependence of the SP coupling is observed depending on the ellipse aspect ratio [29].

For square and rectangular-shaped apertures the intensity profile of the transmitted light is strongest at the edges. The aspect ratio (width/length) of rectangular apertures is a critical factor in determining the coupling between the incident light and the LSP modes of the device. As the aspect ratio decreases, a redshift of the resonance peak is observed, and the transmission peak broadens. For the square apertures, a polarisation dependant output was not observed when they were placed on an array with equal periodicity in both directions [30-32].

Cross-shaped apertures (which are used extensively in this thesis) share some common elements with the original mesh design (called an "inductive grid") made by Ulrich in the late 1960's. Ulrich's mesh filter was made from a 5 μm thick metal sheet with a spacing of 2000 lines per inch. Figure 1.2 shows the transmission spectra of a

device based on Ulrich's mesh grid. The cross-shaped apertures shown have the same periodicity in both directions. Compared to the optical filters available at the time, Ulrich's filters offered the advantage of being able to operate over a very broad range of wavelengths. However, due to limitations in the fabrication, the construction tolerances were poor leading to substantial losses within the filter [33].
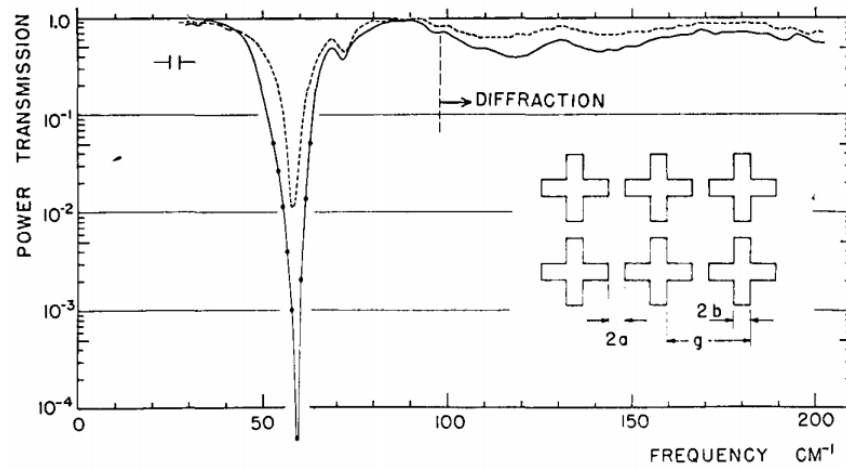
Figure 1.2 *Measured transmission of Ulrich's mesh filter, the periodicity is defined by g =102 μm, and the cross size and smallest distance between openings as a/g=0.13, and b/g=0.06 respectively. The performance of this design was subject to significant losses owing to the poor construction tolerances ref [33].*

Following the discovery of EOT through sub-wavelength apertures by Ebbsen et al. [4, 5], a number of follow up papers have studied the transmission properties of cross-shaped apertures [34-37]. The earliest designs consisted of two orthogonal rectangular holes arranged periodically in the x and y directions on a metal/quartz structure [38-42]. The size of the orthogonal rectangular holes could be varied independently and the periodicity changes in the x and y directions. The resonant wavelength was determined by the localised

charge oscillation around each cross arm. It was found that the transmitted light not only had a strong dependence on the size of the individual rectangles but also on the polarisation of the incident light. Chen et al. systematically investigated this effect using a range of different aperture sizes and by varying the array periodicity in the x and y directions [30].

1.2.2 Polarisation sensitive plasmonic devices

In contrast to the conventional colour filters, which only produce one colour, when the nanoapertures, which make up a plasmonic device, have different array periodicities in the x and y directions, it is possible to have a degree of control over the colour output. As nanofabrication techniques have advanced it has also been possible to control the asymmetry of the nanoapertures themselves adding a further layer of polarisation sensitivity. The easiest method for varying the plasmon resonances, and therefore the colours, which are observed in a plasmonic colour filter with multiple array periodicities or asymmetric nanoaperture shapes, is to change the polarisation vector of the incident light. By doing this, it is possible to access a much wider (i.e. continuously tuneable) range of colours [38, 43, 44]. We here term these types of polarisation sensitive plasmonic colour filters as chromatic plasmonic polarisers (CPPs).

Over the past two decades, researchers have investigated a variety of approaches to obtaining a continuously tuneable colour pallet in transmission. However, the majority of studies have focused on non-polarization sensitive structures, such as circular holes. In this case the colour filtering was performed just by changing the array periodicity, array configuration, the angle of the incident light or the substrate thickness [45, 46]. By incorporating asymmetric nanoaperture structures, such as crosses – where the arm lengths can be varied independently, the flexibility and dynamic range of these devices is significantly increased.

Figure 1.3a illustrates the localised charge distribution around the cross-shaped holes, and 1.3b shows a cross-shaped metallic array used as a chromatic plasmonic polarizer (CPP) with active colour 'pixels'. The associated transmission spectra for this device is shown in Figure 1.3c. The wavelength and polarization-angle dependent transmission, T, through a perforated metallic film is calculated using the following relation:

$$T(\varphi, \lambda) = T_{vertical}(\lambda)\sin^2\varphi + T_{horizontal}(\lambda)\cos^2\varphi \qquad (1.1)$$

here φ is the polarization angle, λ is the free space wavelength of the incident light, and $T_{vertical}(\lambda)$ and $T_{horizontal}(\lambda)$ are the transmitted light contributions associated with the vertical and horizontal axes, respectively [47].
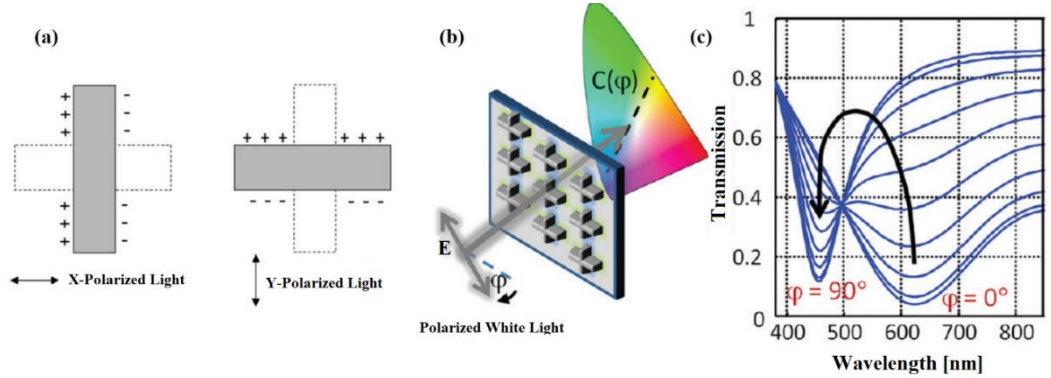
Figure 1.3 a) LSP induced charge distribution around the cross-shaped apertures arms for the X- and Y-polarized light, b) The CPP and c) simulated zero-order transmission spectra of cross-shaped hole arrays illuminated by linearly polarized light for polarisation angles between 0 and 90 degrees (varying in 10 degree increments). Adapted with permission from references [30, 47].

9

The inherent polarisation sensitivity of cross-shaped apertures makes them a good candidate for exploring the effects of the polarisation of the incident light on the optical output of these devices. Recent research has shown that these devices can be optimised for multiple polarisation states without significant loss in plasmon efficiency [48-52]. It is these types of nanoaperture that will form the basis for much of the work presented in this thesis.

1.3   Plasmonic colour filters

Progress in nanofabrication techniques such as EBL and FIB have inspired a number of new approaches to fabricating complex, functional plasmonic devices on the nanometre scale. A large amount of research has been devoted to trying to manipulate colour output via near-surface interactions at sub-wavelength length scales [16, 53-56]. One of the most common approaches for fabricating these types of devices is to use FIB which allows for high-precision milling at length-scales down to just a few nanometeres. Another approach which is routinely used for fabricating plasmonic nanostructures is EBL. In EBL nanolithography nanometre-sized electron beams are used to directly 'write' structures into thin polymer films [20, 57-60]. Both of these manufacturing approaches have been used to produce plasmonic devices that can alter the intrinsic properties of light.

The use of perforated metallic films supported by a dielectric substrate to 'filter' polychromatic light via SP interactions has emerged as one of the most conceptually promising avenues of research [61]. In combination with choosing the right materials and device geometry, plasmonic colour filters can be adapted for a wide rage of different applications. These type of plasmonic device fall under the broad class of metamaterials and as fabrication methods have improved, they have increasingly found applications in the visible range [62]. The SPR phenomena that are present in perforated metallic thin films typically manifest as more than one resonance peak in the frequency-dependant transmission spectrum. In general, both LSPs and SP are generated within these types of

devices. The LSPs are confined to the localised features within the thin film (e.g. nanoapertures or nanoparticles) whilst the longer-range SPs which propagate along the metal-dielectric interface, when initiated via plasmon coupling to the incident light, are known as SPPs. It should be emphasised that SPPs and LSPs are two different classes of SP excitation. Whereas LSPs are confined/localised surface modes, SPPs are propagating modes (these phenomena are explained in further detail in chapter 2) [63-66]. The range of applications for perforated metallic thin films include biosensors [67, 68], plasmonic colour generators [69], spectral filters [70, 71], and active layers within solar cell [72]. As discussed previously, for applications involving colour filtering of visible light, silver is a common choice for a plasmonic material owning to its relatively low plasmonic losses.

1.4 Passivation of plasmonic devices

Silver thin films perforated by sub-wavelength holes and supported on a dielectric substrate exhibit characteristic resonance peaks without any significant diffraction of the zero-order light. The maximum transmission of such an array can be orders of magnitude larger than that predicted by classical optics [4, 5, 73]. However, only oxide-free metallic surfaces give the sharpest and most well-defined SPR peaks. Therefore, for plasmonic devices that are realised in Ag thin films oxidation is a significant practical barrier to real-world application [74]. Hence, despite the excellent results obtained using silver plasmonics, their performance degradation due to their long-term instability is an ongoing challenge [75].

Many approaches have been trailed to address this issue, which includes coating the Ag with a protective layer to stop oxygen from reaching the surface. However, these protective films must be extremely thin so as not to impact the performance of the device. They should also conform precisely to the surface patterning of the plasmonic device in order to avoid any gaps between the active metal layer and the protective coating. One approach we have developed which addresses these requirements is to use extremely thin (several nanometers

thick) layers of Diamond-like Carbon (DLC). In spite of how thin these layers are, we have demonstrated that they successfully protect Ag-based nanoscale plasmonic structures against the effect of oxidative aging. The DLC layers which can be formed via electron-beam induced deposition[76], are both chemically inert and electrochemically stable making the protected devices suitable for a range of different applications[77]. The effectiveness of DLC protection for plasmonic devices was tested by introducing volatile organic molecules to the protected surface. It was discovered that the degree of protection improved as the dose used to deposit the DLC layer was increased.

1.5   Enhancing the performance of plasmonic devices

As more and more applications present themselves the demand for even further improvements to performance in detection and imaging using plasmonics has steadily increased. The three main factors affecting the quality of performance using plasmonic devices can be summarised as [78]:

1.   Sensitivity (S). Sensitivity is a term used to quantify the ratio of a shift in the SPR angle (for monochromatic light) or SPR wavelength (for full-spectrum light) to the corresponding relative change in refractive index (RI) within the sensing region. It can be defined via the following equation $S = \Delta A_{SP}/\Delta n_s$, where A is the angle or the wavelength and n_s the refractive index.

2.   Signal-to-noise ratio (SNR). This ratio is used to quantify the 'background' for the signal of interest (e.g. shift in SPR peak position. In the context of RI sensing using SPR it is often defined as: $SNR = \Delta A_{SP}/SP_{FW}$. Where SP_{FW} denotes the FWHM of the SPR peak.

3.   Quality factor (QF) or Figure of Merit (FoM). This is defined as the ratio of sensitivity to the FWHM of the relevant SPR peak, i.e. $QF = S/SP_{FW}$ [78].

The main approaches used to improve the 3 quality characteristics described above include adding nanoparticles to the device. Typically, the inclusion of Au and Ag nanoparticles has, under certain conditions, been shown the improve the sensitivity of plasmonic devices by amplifying the signal when target molecules are detected. Because of ease of fabrication and the fact that large numbers of these particles can be produced in a colloidal suspension with specific size and composition they offer many options for tailoring the optical and electronic response of plasmonic devices [79].

Exploiting Attenuated Total Reflection (ATR) is another approach used to enhance SPR sensing. ATR involves a combination of the Kretschmann configuration (which results in the production of an evanescent wave) and the energy conservation law. It employs a glass prism in order to satisfy momentum coupling between free electrons at the metal-dielectric interface and the incident light. In the Kretschmann configuration, the metal film is deposited onto one face of the glass prism. When illuminated, an evanescent wave penetrates through the thin metal film resulting in the excitation of plasmons at the outer side of the film. At a specific angle (the SPR angle) there is a maximum amount of energy converted from the incident light into SPPs [80-82]. The use of ATR can magnify the changes in the SPR angle as a function of the local refractive index within the sensing region of the film such that they are easier to detect.

Using bimetallic films to enhance the detection of changes in the SPR peak position has also been explored in the literature. For example, Au is an extremely popular choice as the basis for fabricating plasmonic devices. However, although it exhibits large shifts in the resonant peak position with changes in the refractive index, the FWHM of the SPR peaks is also typically broad. This in turn results in a decrease in the SNR [83]. In contrast to Au, Ag has a narrower SPR peak and possesses a higher SNR value but suffers from being

chemical unstable. To exploit the properties of both materials for SPR sensing, Zynio et al. demonstrated a new method based on bimetallic Ag/Au layers [84]. This was followed up by work from Ong et al. who showed that bimetallic Ag/Au layers have a smaller resonance peak FWHM value and minimum reflectivity compared to Au alone and therefore offer improvements over pure metallic SPR sensors in terms of sensitivity and SNR [83].

Finally, as discussed above, periodic arrays of plasmonic nanostructures are a very common method for enhancing signal strength. Individually or when placed randomly on a surface, plasmonically active structure such as nanoparticles may only produce a weak SPR signal. However, when aligned periodically and acting in concert, the presence and influence of both LSPs and SPPs can have a profound effect on the sensitivity of plasmonic devices and the EOT phenomena [85, 86]. By tailoring the device geometry e.g. nanoaperture shape, size and array periodicity, the sensitivity of these devices to changes in RI can be increased, the QF improved and the SNR maximised.

1.6   The effect of the substrate on SPR properties

Label-free sensing of chemicals and molecules has been a driving motivation for developing a whole range of novel plasmonic devices. Many of these structures exploit EOT phenomena using periodic arrays of metallic nanoapertures to detect tiny changes in the local chemical environment which includes the study of individual binding events [87-91]. Malinsky and Michelle et al. have explored the optical properties of a range of different dielectric substrates (silica, mica and glass) and how this impacts chemical sensing using LSPR extinction in Ag [92]. They monitored the LSPR peak (λ_{max}) associated with Ag nanoparticle arrays and observed a red shift in the peak resonant wavelength as the RI of the substrate increased. In a similar study Duyne's group systematically looked at the change in the LSPR peak position $(\Delta\lambda_{max})$ as a function of the substrate refractive index and found that the LSPR peak moved 87 nm per substrate RIU. However, it was later argued

that the sensitivity factor they had calculated by Discrete Dipole Approximation (DDA) modelling overestimated the sensitivity by a factor of 2 [93].

Kreibig and co-workers have also compared the influence of different types of substrates (dielectric, semiconductor, and metals) had on the SPR absorption within Ag nanoparticles. They observed a much smaller influence on the SPR behaviour when the substrate was changed from a conductor to a dielectric particularly when the evanescent field was probed at distances larger than the Ag nanoparticle diameter [94].

1.7 Modifying the surface chemistry of plasmonic devices

One of the most common uses of plasmonic devices is as sensors, as such, there is a strong interest in being able to tailor the surface chemistry of these devices to target particular compounds or detect specific changes in the local environment. Both inorganic and organic materials have been used to modify the surface of plasmonic devices. Their inclusion in plasmonics has led to a host of new physical [95-97], chemical [98] and electrical [99] properties being realised. Applications for surface-modified plasmonic devices include their use as optical waveguides [100], antireflection coatings [101] and molecular sensors.

Although conventional polymers have shown great promise as optical components, they suffer from limitations in the maximum value of the RI that can be achieved (around 1.6) [101]. In order to overcome this limitation a new range of inorganic materials with very high refractive index, such as ZrO_2, CdS, SNO_2 and TiO_2 have been researched [102-105]. By using such materials as coatings for plasmonic devices researchers hope to be able to push the optical performance of metamaterials even further than is currently possible. Further modification of the surface of thin films is possible via ion implantation with either metal or non-metal ions. For example, TiO_2 has been used as the active layer in

photovoltaics where doping has been found to substantially increase the photosensitivity of the devices [40, 106-108].

1.8 SPR sensing of thin films

Although, in terms of sensing, plasmonic devices have primarily been employed as molecular or chemical sensors there is a substantial interest in using these devices to probe the properties of thin films. For example, probing physical or chemical changes within thin films can be very challenging to do without time-consuming often destructive characterisation tools (e.g. atom probe). Within this thesis we explore the application of plasmonic colour filters for probing the optoelectronic properties of thin films. Specifically, we look at TiO_2 thin films as there is a substantial interest in this material within the electronics industry as well as for a number of optical applications (due to its high RI).

TiO_2 is often doped with Ga ions (for example to increase its photosensitivity) as well as to improve the stability of the lattice [40, 106, 107]. In Chapter 5 we show that it is possible to probe the properties of TiO_2 thin films directly using plasmonic devices. Using FIB we are able to dope different regions of the TiO_2 thin film by different amounts and to then characterise the doped regions using SPR. By using two different array periodicities and employing cross-shaped nanoapertures for the plasmonic array we are able to demonstrate that the sensitivity of the devices to Ga ion doping can be maximised through control over the incident polarisation. Changes in the local dielectric constant of the TiO_2 thin film are directly probed using bright-field microscopy and characterised by a change in the transmitted intensity. This work highlights the potential for bimodal plasmonic devices for characterising thin films – in this case acting as a means for calibrating and characterising ion implantation.

1.9   Chemical sensing using plasmonic devices

The sensitivity of EOT-based plasmonic devices to small changes in the local chemistry have meant that they have found extensive application as chemical sensors. Both changes in the RI of chemicals as well as individual molecular binding events have been studied, predominantly in the red and NIR regions of the visible spectrum [109-113]. Although they have great sensitivity, SNR is often small and there are issues associated with EOT based sensors due to the low levels of light which is transmitted (typically ~ 5% which is nonetheless much higher than predicted classically) [111, 114]. One way to increase the efficiency of EOT plasmonic sensors is by incorporating a prism as the substrate, however this makes them substantially bulkier and less convenient to use [115, 116]. Moreover, non-prism-based devices using white light have the potential for detecting chemical changes readily 'by eye' as a colour change in the transmitted light. A non-prism based approach also opens up the possibility of readily being combined with microfluidics for quick and efficient delivery of the analyte, hence it is this type of EOT structure which is explored in the context of this thesis [117, 118].

1.10 Molecular sensing using plasmonic devices

Organic molecular assemblies which spontaneously form on surfaces, also known as Self-Assembled Monolayers (SAMs), are composed of ordered domains which collectively make up a close-packed 2D system. SAMs have been proven to be a convenient and simple means of tailoring the interfacial properties of material surfaces opening up a range of new opportunities including for both bio and photo-sensitive applications [119-122]. Other common uses for SAMs include the delivery of biomolecules and other types of therapeutic molecules [123]. In spite of the extensive research that has been conducted into SAMs there remain a number of open questions regarding their formation. In order to address these

questions, the development of techniques that enable the direct imaging of SAM formation is highly desirable.

Previous studies have employed nanoscale metallic waveguides [124, 125] and nanoantennas [126] for real-time monitoring of SAM formation on metallic surfaces. More recently plasmonic devices with high FoM in terms of their performance have been researched as a means for probing the surface chemistry of SAM formation. The benefits of using plasmonic devices for studying SAMs include the ability to directly monitor the SAM formation via direct detection of the attachment of molecules to the metallic film making up the active layer of the plasmonic device. The sensitivity of these devices is such that they can detect changes in thickness even at the level of individual molecules via tiny movements in the position of the SPR peaks. In this thesis we explore the use of periodic arrays of cross-shaped nanoapertures in Ag films for the characterisation of SAM formation. These devices show great promise as a molecular sensor due to their high FoM and the fact that the output can be tailored by control over the incident polarisation. Our goal in Chapter 6 is to determine if these types of plasmonic device can be used for the direct detection of SAM formation with the goal of better understanding the underlying chemistry governing self-assembly of monolayers [119, 127, 128].

1.11 Thesis summary

The underlying theme of this thesis is to investigate the properties and applications of plasmonic devices consisting of arrays of cross-shaped nanoapertures in Ag films. The output and functional response of these arrays can be finely tuned by varying the geometrical parameters which include the arm ratio of the individual nanoapertures as well as the overall periodicity in each dimension. In Chapter 2 we review the underlying theory and literature relevant to the work presented in this thesis focusing on the use of plasmonic

devices as colour filters and discussing the motivation for the applications studied as part of the present research.

Chapter 3 demonstrates how it is possible to obtain a continuously tuneable colour pallet using these devices and also looks at the effect of device geometry and incident polarisation. Both experimental and numerical calculations are used to investigate the dependence of the SPR characteristics of these devices on these parameters. Publications describing some of the results presented in these chapters can be found in refs [70, 71].

In Chapter 4, we address the issue of passivation of Ag plasmonic devices and explore the effectiveness of Diamond-like-carbon (DLC) at protecting these devices from the deleterious effects of oxidation. We are able to demonstrate that DLC can form a conformal, biocompatible and chemically stable protection layer which can be conveniently formed by scanning focused beams of electrons across the surface of the device. We find that the presence of nanometre thick layers of DLC does not affect the functionality or performance of the devices and is able to effectively adhere to the complex nanometre scale structure of the apertures. We also investigate how the electron dose influences the effectiveness of DLC to prevent aging with a summary of the results published in ref[19].

Chapter 5 presents a new application, exploiting the dual pitch architecture of cross-shaped nanopixels to characterise small variations of the complex dielectric constant of an ion implanted TiO_2 thin film. Also, it demonstrates the ability to directly monitor the optical contrast of the ion-implanted regions. Monte Carlo simulations were employed to calculate the number of interstitial ions and empirically calculate the complex dielectric constant of implanted regions. Numerical calculations were performed to determine the value of the complex refractive index and, combined with FEM simulations, enable a detailed interpretation of the experimental data to be made.

In Chapter 6, a new approach to analysing the output of bimodal plasmonic devices is investigated, a technique we term "optical chemical barcoding". This approach is used to detect small changes in the RI of analytes for chemical sensing. We find that the sensitivity of the devices within the optical regime can be tuned to the point where small changes in the local RI can be detected 'by eye'. The application of bimodal plasmonic devices composed of cross-shaped nanopixels arrays for label-free detection of SAM formation is also investigated in Chapter 6. The self-organised growth dynamics of thiol-based monolayers on Ag-based plasmonic devices was studied by monitoring the resonant peak shift in the plasmonic spectrum using a high-precision spectrometer. The polarization response of these devices was exploited to further increase the detection sensitivity.

Finally, Chapter 7 presents a summary of the main conclusions and discusses possible avenues for future work as well as the challenges encountered in fabricating and using plasmonic devices whilst conducting research for this thesis.

1.12 References

1.   Rawcliffe, R. and C. Randall, *Metal mesh interference filters for the far infrared.* Applied optics, 1967. **6**(8): p. 1353-1358.

2.   Madou, M.J., *Fundamentals of microfabrication: the science of miniaturization*. 2002: CRC press.

3.   Kelly, K.L., et al., *The optical properties of metal nanoparticles: the influence of size, shape, and dielectric environment*. 2003, ACS Publications.

4.   Ebbesen, T.W., et al., *Extraordinary optical transmission through sub-wavelength hole arrays.* Nature, 1998. **391**(6668): p. 667.

5.   Ghaemi, H., et al., *Surface plasmons enhance optical transmission through subwavelength holes.* Physical review B, 1998. **58**(11): p. 6779.

6.   Zhang, K. and O. Rabin, *Tailoring Localized Surface Plasmon Resonances in Metallic Nanoarcs for Surface Enhanced Infrared Absorption Spectroscopy.* Bulletin of the American Physical Society, 2019.

7.   Halas, N.J., et al., *Nanoparticle-based all-optical sensors*. 2004, Google Patents.

8.   Halas, N., et al., *Nanoparticle-based all-optical sensors*. 2005, Google Patents.

9.   Rodríguez-Fortuño, F.J., et al., *Highly-sensitive chemical detection in the infrared regime using plasmonic gold nanocrosses.* Applied Physics Letters, 2011. **98**(13): p. 133118.

10.   Cui, A., et al., *Directly patterned substrate-free plasmonic "nanograter" structures with unusual Fano resonances.* Light: Science & Applications, 2015. **4**(7): p. e308.

11.   West, P.R., et al., *Searching for better plasmonic materials.* Laser & Photonics Reviews, 2010. **4**(6): p. 795-808.

12.   Kneipp, K. and H. Kneipp, *Non-resonant SERS Using the Hottest Hot Spots of Plasmonic Nanoaggregates.* Frontiers of Surface-Enhanced Raman Scattering: Single Nanoparticles and Single Cells, 2014: p. 19-35.

13.   Liu, Z., et al., *Far-field optical hyperlens magnifying sub-diffraction-limited objects.* science, 2007. **315**(5819): p. 1686-1686.

14.   Shalaev, V.M., et al., *Negative index of refraction in optical metamaterials.* Optics letters, 2005. **30**(24): p. 3356-3358.

15.   Simonsen, I., *Optics of surface disordered systems.* The European Physical Journal Special Topics, 2010. **181**(1): p. 1-103.

16. Maier, S.A. and H.A. Atwater, *Plasmonics: Localization and guiding of electromagnetic energy in metal/dielectric structures.* Journal of applied physics, 2005. **98**(1): p. 10.

17. Schmidt, S., et al., *Adiabatic nanofocusing on ultrasmooth single-crystalline gold tapers creates a 10-nm-sized light source with few-cycle time resolution.* ACS nano, 2012. **6**(7): p. 6040-6048.

18. Oates, T. and A. Mücklich, *Evolution of plasmon resonances during plasma deposition of silver nanoparticles.* Nanotechnology, 2005. **16**(11): p. 2606.

19. Balaur, E., et al. *Electron-beam induced diamond-like-carbon passivation of plasmonic devices.* in *Micro+ Nano Materials, Devices, and Systems.* 2015. International Society for Optics and Photonics.

20. Wei, H. and H. Eilers, *From silver nanoparticles to thin films: Evolution of microstructure and electrical conduction on glass substrates.* Journal of Physics and Chemistry of Solids, 2009. **70**(2): p. 459-465.

21. Tobiška, P., et al., *An integrated optic hydrogen sensor based on SPR on palladium.* Sensors and Actuators B: Chemical, 2001. **74**(1-3): p. 168-172.

22. Baldelli, S., et al., *Surface enhanced sum frequency generation of carbon monoxide adsorbed on platinum nanoparticle arrays.* The Journal of Chemical Physics, 2000. **113**(13): p. 5432-5438.

23. Chan, G.H., et al., *Plasmonic properties of copper nanoparticles fabricated by nanosphere lithography.* Nano Letters, 2007. **7**(7): p. 1947-1952.

24. Blaber, M., et al., *Plasmon absorption in nanospheres: A comparison of sodium, potassium, aluminium, silver and gold.* Physica B: Condensed Matter, 2007. **394**(2): p. 184-187.

25.   Langhammer, C., et al., *Localized surface plasmon resonances in aluminum nanodisks.* Nano letters, 2008. **8**(5): p. 1461-1471.

26.   Degiron, A., et al., *Optical transmission properties of a single subwavelength aperture in a real metal.* Optics Communications, 2004. **239**(1-3): p. 61-66.

27.   Baida, F. and D. Van Labeke, *Light transmission by subwavelength annular aperture arrays in metallic films.* Optics communications, 2002. **209**(1-3): p. 17-22.

28.   Orbons, S. and A. Roberts, *Resonance and extraordinary transmission in annular aperture arrays.* Optics express, 2006. **14**(26): p. 12623-12628.

29.   Kofke, M.J., et al., *The effect of periodicity on the extraordinary optical transmission of annular aperture arrays.* Applied Physics Letters, 2009. **94**(2): p. 023104.

30.   Chen, C.-Y., et al., *Extraordinary transmission through a silver film perforated with cross shaped hole arrays in a square lattice.* Applied Physics Letters, 2007. **91**(6): p. 063108.

31.   Inoue, D., et al., *Polarization independent visible color filter comprising an aluminum film with surface-plasmon enhanced transmission through a subwavelength array of holes.* Applied Physics Letters, 2011. **98**(9): p. 093113.

32.   Gordon, R. and A.G. Brolo, *Increased cut-off wavelength for a subwavelength hole in a real metal.* Optics Express, 2005. **13**(6): p. 1933-1938.

33.   Ulrich, R., *Interference filters for the far infrared.* Applied Optics, 1968. **7**(10): p. 1987-1996.

34.   Lin, L., et al., *Plasmonic lenses formed by two-dimensional nanometric cross-shaped aperture arrays for Fresnel-region focusing.* Nano letters, 2010. **10**(5): p. 1936-1940.

35.   Girard-Desprolet, R., et al., *Angular and polarization properties of cross-holes nanostructured metallic filters.* Optics express, 2013. **21**(24): p. 29412-29424.

36.   Chen, X., et al., *Dual-polarity plasmonic metalens for visible light.* Nature communications, 2012. **3**: p. 1198.

37.   Bouillard, J.-S., et al., *Optical transmission of periodic annular apertures in metal film on high-refractive index substrate: the role of the nanopillar shape.* Applied Physics Letters, 2010. **96**(20): p. 201101.

38.   Li, Z., A.W. Clark, and J.M. Cooper, *Dual color plasmonic pixels create a polarization controlled nano color palette.* ACS nano, 2016. **10**(1): p. 492-498.

39.   Si, G., et al., *Annular aperture array based color filter.* Applied Physics Letters, 2011. **99**(3): p. 033105.

40.   Yu, Y., et al., *Transmissive/reflective structural color filters: theory and applications.* Journal of Nanomaterials, 2014. **2014**: p. 6.

41.   Lee, T., et al., *Plasmonic-and dielectric-based structural coloring: from fundamentals to practical applications.* Nano Convergence, 2018. **5**(1): p. 1-21.

42.   Mahani, F., A. Mahanipour, and A. Mokhtari. *Optimization of plasmonic color filters for CMOS image sensors by genetic algorithm.* in *2017 2nd Conference on Swarm Intelligence and Evolutionary Computation (CSIEC)*. 2017. IEEE.

43.   Mahros, A.M. and M.M. Tharwat, *Investigating the fabrication imperfections of plasmonic nanohole arrays and its effect on the optical transmission spectra.* Journal of Nanomaterials, 2015. **2015**: p. 4.

44.   Lin, L. and A. Roberts, *Light transmission through nanostructured metallic films: coupling between surface waves and localized resonances.* Optics express, 2011. **19**(3): p. 2626-2633.

45.   Si, G., et al., *Reflective plasmonic color filters based on lithographically patterned silver nanorod arrays.* Nanoscale, 2013. **5**(14): p. 6243-6248.

46.   Yokogawa, S., S.P. Burgos, and H.A. Atwater, *Plasmonic color filters for CMOS image sensor applications.* Nano letters, 2012. **12**(8): p. 4349-4354.

47.   Ellenbogen, T., K. Seo, and K.B. Crozier, *Chromatic plasmonic polarizers for active visible color filtering and polarimetry.* Nano letters, 2012. **12**(2): p. 1026-1031.

48.   Xu, T., et al., *Plasmonic nanoresonators for high-resolution colour filtering and spectral imaging.* Nature communications, 2010. **1**: p. 59.

49.   Chen, Q., et al., *A CMOS image sensor integrated with plasmonic colour filters.* Plasmonics, 2012. **7**(4): p. 695-699.

50.   Xue, J., et al., *Scalable, full-colour and controllable chromotropic plasmonic printing.* Nature communications, 2015. **6**: p. 8906.

51.   Rajasekharan, R., et al., *Filling schemes at submicron scale: Development of submicron sized plasmonic colour filters.* Scientific reports, 2014. **4**: p. 6435.

52.   Zeng, B., Y. Gao, and F.J. Bartoli, *Ultrathin nanostructured metals for highly transmissive plasmonic subtractive color filters.* Scientific reports, 2013. **3**: p. 2840.

53.   Lezec, H.J., et al., *Beaming light from a subwavelength aperture.* Science, 2002. **297**(5582): p. 820-822.

54.   Laref, S., et al., *Size-dependent permittivity and intrinsic optical anisotropy of nanometric gold thin films: a density functional theory study.* Optics express, 2013. **21**(10): p. 11827-11838.

55.   Maier, S.A., *Plasmonics: The promise of highly integrated optical devices.* IEEE Journal of selected topics in Quantum Electronics, 2006. **12**(6): p. 1671-1677.

56.   Betzig, E. and J.K. Trautman, *Near-field optics: microscopy, spectroscopy, and surface modification beyond the diffraction limit.* Science, 1992. **257**(5067): p. 189-195.

57.   Reyntjens, S. and R. Puers, *A review of focused ion beam applications in microsystem technology.* Journal of micromechanics and microengineering, 2001. **11**(4): p. 287.

58.   Ventra, M., S. Evoy, and J.R. Heflin, *Introduction to nanoscale science and technology*. 2006: Springer Science & Business Media.

59.   Ziegler, J.F. and J.P. Biersack, *The stopping and range of ions in matter*, in *Treatise on heavy-ion science*. 1985, Springer. p. 93-129.

60.   Ziegler, J.F., J. Biersack, and U. Littmark, *The stopping and range of ions in solids, vol. 1*. 1985, Pergamon, New York.

61.   Tanriover, I. and H.V. Demir, *Broad-band polarization-insensitive all-dielectric metalens enabled by intentional off-resonance waveguiding at mid-wave infrared.* Applied Physics Letters, 2019. **114**(4): p. 043105.

62.   Pratsinis, S.E., *Aerosol-based technologies in nanoscale manufacturing: from functional materials to devices through core chemical engineering.* AIChE journal, 2010. **56**(12): p. 3028-3035.

63.   Huber, R., et al., *How many-particle interactions develop after ultrafast excitation of an electron–hole plasma.* Nature, 2001. **414**(6861): p. 286.

64.   Van Exter, M. and D. Grischkowsky, *Optical and electronic properties of doped silicon from 0.1 to 2 THz.* Applied Physics Letters, 1990. **56**(17): p. 1694-1696.

65.   Yang, X., et al., *Breaking the feature sizes down to sub-22 nm by plasmonic interference lithography using dielectric-metal multilayer.* Optics express, 2009. **17**(24): p. 21560-21565.

66.   Müller, R., V. Malyarchuk, and C. Lienau, *Three-dimensional theory on light-induced near-field dynamics in a metal film with a periodic array of nanoholes.* Physical Review B, 2003. **68**(20): p. 205415.

67.   Donda, K.D. and R.S. Hegde, *Optimal design of beam-deflectors using extended unit-cell metagratings.* Progress In Electromagnetics Research, 2019. **77**: p. 83-92.

68.   Xiong, K., et al., *Active control of plasmonic colors: emerging display technologies.* Reports on Progress in Physics, 2019. **82**(2): p. 024501.

69.   Vashistha, V., et al., *All-dielectric metasurfaces based on cross-shaped resonators for color pixels with extended gamut.* ACS photonics, 2017. **4**(5): p. 1076-1082.

70.   Balaur, E., et al., *Continuously tunable, polarization controlled, colour palette produced from nanoscale plasmonic pixels.* Scientific reports, 2016. **6**: p. 28062.

71.   Balaur, E., et al. *Optimisation of polarization controlled colour tuning using nanoscale cross-shaped apertures in silver films*. in *SPIE BioPhotonics Australasia*. 2016. International Society for Optics and Photonics.

72.   Paci, B., et al., *Enhanced structural stability and performance durability of bulk heterojunction photovoltaic devices incorporating metallic nanoparticles.* Advanced Functional Materials, 2011. **21**(18): p. 3573-3582.

73.   Bethe, H.A., *Theory of diffraction by small holes.* Physical review, 1944. **66**(7-8): p. 163.

74.   Choudhury, S.A. and M.H. Chowdhury. *The Promise and Challenges of Enhancing Solar Cell Efficiency Using Patterned Nanostructures*. in *1st International Conference on Advanced Information and Communication Technology*. 2016.

75.   Dasgupta, A., et al., *Directional Fluorescence Emission Mediated by Chemically-Prepared Plasmonic Nanowire Junctions.* The Journal of Physical Chemistry C, 2016. **120**(31): p. 17692-17698.

76.   Djenizian, T., E. Balaur, and P. Schmuki, *Direct immobilization of DNA on diamond-like carbon nanodots.* Nanotechnology, 2006. **17**(8): p. 2004.

77.   Djenizian, T., et al., *Electron beam induced carbon deposition used as a negative resist for selective porous silicon formation.* Surface science, 2003. **524**(1-3): p. 40-48.

78.   Maurya, J., et al., *Sensitivity enhancement of surface plasmon resonance sensor based on graphene–MoS 2 hybrid structure with TiO 2–SiO 2 composite layer.* Applied Physics A, 2015. **121**(2): p. 525-533.

79.   Tabasi, O. and C. Falamaki, *Recent advancements in the methodologies applied for the sensitivity enhancement of surface plasmon resonance sensors.* Analytical methods, 2018. **10**(32): p. 3906-3925.

80.   Hatta, A., Y. Suzuki, and W. Suëtaka, *Infrared absorption enhancement of monolayer species on thin evaporated Ag films by use of a Kretschmann configuration: Evidence for two types of enhanced surface electric fields.* Applied Physics A, 1984. **35**(3): p. 135-140.

81.   Bera, M. and M. Ray, *Parametric analysis of multi-layer metallo–dielectric coupled plasmonic resonant structures using homo and hetero-bimetallic nanofilms.* Optics Communications, 2013. **294**: p. 384-394.

82.   Shalabney, A. and I. Abdulhalim, *Electromagnetic fields distribution in multilayer thin film structures and the origin of sensitivity enhancement in surface plasmon resonance sensors.* Sensors and Actuators A: Physical, 2010. **159**(1): p. 24-32.

83.   Ong, B.H., et al., *Optimised film thickness for maximum evanescent field enhancement of a bimetallic film surface plasmon resonance biosensor.* Sensors and Actuators B: Chemical, 2006. **114**(2): p. 1028-1034.

84.   Zynio, S., et al., *Bimetallic layers increase sensitivity of affinity sensors based on surface plasmon resonance.* Sensors, 2002. **2**(2): p. 62-70.

85.   Yin, L., et al., *Surface plasmons at single nanoholes in Au films.* Applied Physics Letters, 2004. **85**(3): p. 467-469.

86.   Xu, T., et al., *Structural colors: from plasmonic to carbon nanostructures.* Small, 2011. **7**(22): p. 3128-3136.

87.   Feng, J., et al., *Nanoscale plasmonic interferometers for multispectral, high-throughput biochemical sensing.* Nano letters, 2012. **12**(2): p. 602-609.

88.   Yanik, A.A., et al., *Integrated nanoplasmonic-nanofluidic biosensors with targeted delivery of analytes.* Applied physics letters, 2010. **96**(2): p. 021101.

89.   Craighead, H., *Future lab-on-a-chip technologies for interrogating individual molecules*, in *Nanoscience And Technology: A Collection of Reviews from Nature Journals*. 2010, World Scientific. p. 330-336.

90.   Prikulis, J., et al., *Optical spectroscopy of nanometric holes in thin gold films.* Nano Letters, 2004. **4**(6): p. 1003-1007.

91.   Schuller, J.A., et al., *Plasmonics for extreme light concentration and manipulation.* Nature materials, 2010. **9**(3): p. 193.

92.   Duval Malinsky, M., et al., *Nanosphere lithography: effect of substrate on the localized surface plasmon resonance spectrum of silver nanoparticles.* The Journal of Physical Chemistry B, 2001. **105**(12): p. 2343-2350.

93.   Draine, B.T., *The discrete-dipole approximation and its application to interstellar graphite grains.* The Astrophysical Journal, 1988. **333**: p. 848-872.

94.   Sherry, L.J., et al., *Localized surface plasmon resonance spectroscopy of single silver nanocubes.* Nano letters, 2005. **5**(10): p. 2034-2038.

95.   Zhang, J., et al., *Study on the optical properties of PPV/TiO2 nanocomposites.* Synthetic metals, 2001. **118**(1-3): p. 181-185.

96.   Nakane, K., et al., *Properties of poly (vinyl butyral)/TiO2 nanocomposites formed by sol–gel process.* Composites part B: engineering, 2004. **35**(3): p. 219-222.

97.   Camargo, P.H.C., K.G. Satyanarayana, and F. Wypych, *Nanocomposites: synthesis, structure, properties and new application opportunities.* Materials Research, 2009. **12**(1): p. 1-39.

98.   Boccaccini, A.R., et al., *Polymer/bioactive glass nanocomposites for biomedical applications: a review.* Composites science and technology, 2010. **70**(13): p. 1764-1776.

99.   Su, S.-J. and N. Kuramoto, *Processable polyaniline–titanium dioxide nanocomposites: effect of titanium dioxide on the conductivity.* Synthetic metals, 2000. **114**(2): p. 147-153.

100.   Yoshida, M. and P.N. Prasad, *Sol− gel-processed SiO2/TiO2/poly (vinylpyrrolidone) composite materials for optical waveguides.* Chemistry of materials, 1996. **8**(1): p. 235-241.

101.   Nakayama, N. and T. Hayashi, *Preparation and characterization of TiO2 and polymer nanocomposite films with high refractive index.* Journal of applied polymer science, 2007. **105**(6): p. 3662-3672.

102.   Lester, S.D., J.N. Miller, and D.B. Roitman, *High refractive index package material and a light emitting device encapsulated with such material*. 1998, Google Patents.

103.   Tom, R.T., et al., *Freely dispersible Au@ TiO2, Au@ ZrO2, Ag@ TiO2, and Ag@ ZrO2 core− shell nanoparticles: one-step synthesis, characterization, spectroscopy, and optical limiting properties.* Langmuir, 2003. **19**(8): p. 3439-3445.

104.   Knez, M., K. Nielsch, and L. Niinistö, *Synthesis and surface engineering of complex nanostructures by atomic layer deposition.* Advanced Materials, 2007. **19**(21): p. 3425-3438.

105.   Hashim, A. and Q. Hadi, *Synthesis of novel (polymer blend-ceramics) nanocomposites: structural, optical and electrical properties for humidity sensors.* Journal of Inorganic and Organometallic Polymers and Materials, 2018. **28**(4): p. 1394-1401.

106.   Amraoui, R., et al., *The electronic structure and optical properties of rutile TiO2 co-doped with nickel and cerium.* Chinese journal of physics, 2017. **55**(6): p. 2393-2399.

107.   Liu, Z.-M., L. Peng, and A.-W. Tang, *Fluoride-assisted synthesis of anatase TiO2 nanocrystals with tunable shape and band gap via a solvothermal approach.* Chinese Chemical Letters, 2016. **27**(12): p. 1801-1804.

108.   Fang, Y.-z., et al., *Role of dopant Ga in tuning the band gap of rutile TiO2 from first principles.* Chinese Journal of Physics, 2018. **56**(4): p. 1370-1377.

109.   Singh, P., *SPR biosensors: historical perspectives and current challenges.* Sensors and actuators B: Chemical, 2016. **229**: p. 110-130.

110.   Grande, M., et al., *Asymmetric plasmonic grating for optical sensing of thin layers of organic materials.* Sensors and Actuators B: Chemical, 2011. **160**(1): p. 1056-1062.

111.   Shalabney, A. and I. Abdulhalim, *Sensitivity-enhancement methods for surface plasmon sensors.* Laser & Photonics Reviews, 2011. **5**(4): p. 571-606.

112.   Jakšić, Z., *Optical metamaterials as the platform for a novel generation of ultrasensitive chemical or biological sensors.* Metamaterials: Classes, Properties and Applications, 2010: p. 1-42.

113. Huang, N.-T., et al., *Recent advancements in optofluidics-based single-cell analysis: optical on-chip cellular manipulation, treatment, and property detection.* Lab on a Chip, 2014. **14**(7): p. 1230-1245.

114. Im, H., et al., *Nanohole-based surface plasmon resonance instruments with improved spectral resolution quantify a broad range of antibody-ligand binding kinetics.* Analytical chemistry, 2012. **84**(4): p. 1941-1947.

115. Guo, T., *Fiber grating-assisted surface plasmon resonance for biochemical and electrochemical sensing.* Journal of Lightwave Technology, 2017. **35**(16): p. 3323-3333.

116. Caucheteur, C., T. Guo, and J. Albert, *Review of plasmonic fiber optic biochemical sensors: improving the limit of detection.* Analytical and bioanalytical chemistry, 2015. **407**(14): p. 3883-3897.

117. Langley, D.P., et al., *Optical chemical barcoding based on polarization controlled plasmonic nanopixels.* Advanced Functional Materials, 2018. **28**(4): p. 1704842.

118. Langley, D., et al. *Dual pitch plasmonic devices for polarization enhanced colour based sensing*. in *SPIE BioPhotonics Australasia*. 2016. International Society for Optics and Photonics.

119. Malinsky, M.D., et al., *Chain length dependence and sensing capabilities of the localized surface plasmon resonance of silver nanoparticles chemically modified with alkanethiol self-assembled monolayers.* Journal of the American Chemical Society, 2001. **123**(7): p. 1471-1482.

120. Yonzon, C.R., et al., *A comparative analysis of localized and propagating surface plasmon resonance sensors: the binding of concanavalin A to a monosaccharide functionalized self-assembled monolayer.* Journal of the American Chemical Society, 2004. **126**(39): p. 12669-12676.

121.   Abdelghani, A., et al., *Study of self-assembled monolayers of n-alkanethiol on a surface plasmon resonance fibre optic sensor.* Thin Solid Films, 1996. **284**: p. 157-161.

122.   Ma, L., et al., *Electrically modulated localized surface plasmon around self-assembled-monolayer-covered nanoparticles.* Langmuir, 2017. **33**(6): p. 1437-1441.

123.   Vashist, S.K., et al., *Delivery of drugs and biomolecules using carbon nanotubes.* Carbon, 2011. **49**(13): p. 4077-4097.

124.   Anker, J.N., et al., *Biosensing with plasmonic nanosensors*, in *Nanoscience and Technology: A Collection of Reviews from Nature Journals*. 2010, World Scientific. p. 308-319.

125.   Kalyuzhny, G., et al., *Transmission surface-plasmon resonance (T-SPR) measurements for monitoring adsorption on ultrathin gold island films.* Chemistry–A European Journal, 2002. **8**(17): p. 3849-3857.

126.   Chapman, R.G., et al., *Preparation of mixed self-assembled monolayers (SAMs) that resist adsorption of proteins using the reaction of amines with a SAM that presents interchain carboxylic anhydride groups.* Langmuir, 2000. **16**(17): p. 6927-6936.

127.   Gao, H., et al., *Screening plasmonic materials using pyramidal gratings.* Proceedings of the National Academy of Sciences, 2008. **105**(51): p. 20146-20151.

128.   Mark, S.S., et al., *Dendrimer-functionalized self-assembled monolayers as a surface plasmon resonance sensor surface.* Langmuir, 2004. **20**(16): p. 6808-6817.

CHAPTER 2

THEORETICAL BACKGROUND AND EXPERIMENTAL METHODS
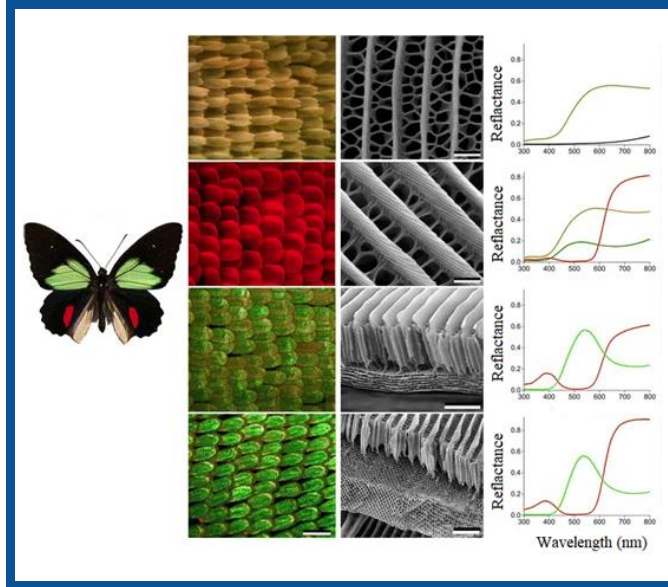
Photograph of the "parides butterfly". The different colours present are shown by the optical images in the second column, the corresponding scanning electron microscopy (SEM) images showing the microstructure are in the third column. The fourth column shows the reflectance spectra. **Reproduced with permission from[1].**

2   INTRODUCTION

This chapter summarises the basic theoretical concepts and background literature underpinning this thesis. A brief introduction to the optical theory of light-matter interactions at the nanoscale is given prior to an in-depth discussion of surface plasmons, both propagating and localised. A particular emphasis is placed on plasmonic colour generation and the propagation and penetration of surface plasmons in these structures. Finally, the main approaches to the fabrication of plasmonic devices for colour filtering are summarised.

2.1 Optical theory of light-matter interactions

Optical interactions with nanoscale structures are mediated by absorption or scattering phenomena which can be understood in terms of Maxwell's equations and quantum mechanics [2]. These concepts have been developed in order to derive the basic theory describing the excitation of surface plasmons (SP). Surface plasmons are two-dimensional delocalised electron oscillations; the electric field amplitude associated with these waves decays exponentially in the direction perpendicular to the propagation direction. Surface plasmon resonance (SPR) occurs when the incident photons have a momentum which is matched to the resonant frequency of the SP. This coupling is governed by both the dielectric properties of the material and any structure of the medium supporting the SP which is on the scale of the wavelength of the incident light [3-5].

When visible light interacts with nanoparticles, both 'size effects' and 'diffractive effects' come into play. An initial theory was developed to try to explain these effects in the early part of the 20th century. In 1908, Gustav Mie developed a model to explain the distinct colours which were observed in the resulting spectrum of light produced by scattering from a colloidal suspension of sub-wavelength particles. From the point-of-view of scattering theory, light scattering by metamaterials can be modelled by considering them as homogeneous media. The electromagnetic properties of such media can be represented by an effective polarizability [6-8]. Over the past few decades Mie theory has been extended to account for details such as the size, shape, and density of the nanoparticles. Mie's solution of diffraction problem is not an independent physical phenomenon but rather is based on the Drude model which describes the transport properties of free electrons in conduction bands [4, 9, 10].

In a dense electron gas, each electron individually interacts with all other electrons and any positive charges; typically, the equations of motion for such a system are extremely complicated. A simpler approach is to try to develop a collective description of electron motion, a starting point for which is to consider the oscillations of each pair of particles interacting through the Coulomb force as contributing to fluctuations in the electron density. In this approach it is possible to describe the motion of the electron gas in terms of the Fourier components of the electron density fluctuations. The density fluctuations can be decomposed into a thermal motion (having no collective behaviour) and Coulomb interactions which act to produce long-range collective behaviour which can be characterised through the 'plasma frequency' [11-15].

According to the Drude model, the intra-band electronic transitions are defined by a dielectric function, ε. The optical response of a non-homogenous medium, can then be determined from the complex dielectric function (electric permittivity) of that medium. In principle, the dielectric properties of materials depend on the induced polarisation of the metal/dielectric and thus is a complex function. The electrical permittivity describes how strongly charge carriers become polarized in response to an external electromagnetic field. The optical response of a non-homogenous, complex medium can then be inferred from knowledge of the electric permittivity of that medium [16-18]. The electric permittivity can be adequately described by:

$$\varepsilon(\omega) = \varepsilon'(\omega) + i\varepsilon''(\omega) \tag{2.1}$$

here $\varepsilon'(\omega)$ and $\varepsilon''(\omega)$ represent the real and imaginary part of the dielectric function respectively. The complex electrical permittivity function, $\varepsilon(\omega)$, is frequency dependent. It is crucial to consider both the real and imaginary parts of the dielectric function together because according to the Kramers-Kronig relation, they affect one another [16, 19]. The real part of the equation describes how strongly a material is polarized by an external

electric field, whilst the imaginary part shows the ohmic losses due to conduction electron losses (electron-electron interaction) and "intraband" electronic transitions. Despite the real part being negative in metals, standard metals' performance suffers from significant ohmic losses, especially at optical and ultraviolet frequencies. Compared to ordinary metals, nanometric scale metallic structures have the potential for the sub-wavelength manipulation and control of optical energy [17, 20, 21].

2.1.1   Basic theory of plasmonic devices

The word "plasmon" denotes a quasiparticle which refers to the quantisation of the collective oscillations of a free electron gas (usually in conduction bands) which has an associated frequency (the plasmon frequency) of oscillation and energy [22, 23]. The SP wave vector is always larger than that of the incident light and thus cannot be directly excited and instead requires a grating or a prism at a specific angle to enable momentum coupling. The primary theory of 'plasmons' is based on charge density oscillations of the electrons associated with the individual atoms which make up the object. The distribution of electrons can be decomposed into bound and free electron components [24]. The basic theory required to understand SPR phenomena is now reviewed.

2.1.2   Surface Plasmon Resonance (SPR)

The plasma frequency (ω_p) is a physical property associated with bulk metals. If the dimensions of the metal are reduced to the sub-wavelength scale, mobile electrons within the conduction band oscillate at the surface of the metal (i.e. at the metal/dielectric interface). Because in this scenario the electron density is effectively shared between two ion lattices the resulting net electric force is halved within each of the media. The surface plasmon oscillations (associated with the surface electron cloud) have a quantized frequency with a corresponding energy of $\hbar\omega_{sp}$ [8]. Under these conditions the free electron density oscillates at a frequency given by

$$\omega_{sp} = \sqrt{\frac{e^2 n_e}{2\varepsilon_0 m_e}} \tag{2.2}$$

here n_e is the density of the metal's free electrons within the conduction band, and m_e is electron's mass [4, 25-28].

The relationship between the SP frequency and the bulk plasma frequency is given by:

$$\omega_{sp} = \frac{1}{\sqrt{2}} \omega_p \tag{2.3}$$

Equation 2.3 implies that if the oscillation frequency of the electrons is less than the bulk plasma frequency then the electrons cannot penetrate the metal.

In 1968 SP waves were classified into two main categories by Otto and Kretschmann [27, 29]:

1) Radiative: known as the intrinsic wave mode owing to the excitation of SP directly by plane electromagnetic (EM) waves. The exited SPs re-radiate photons with new resonance modes called plasma radiation which propagates in almost all directions.

2) Non-radiative: Although the non-radiative mode cannot intrinsically re-radiate, it is able to radiate under specific conditions such as coupling with incident light on a grating surface. The SP associated with non-radiative mode has a phase velocity smaller than the speed of light [10, 22, 30].

It is important to note that, the name "non-radiative SP wave" is derived from the evanescent characteristics of SP. The evanescent SP waves undergo exponential decay as a function of distance from the metal-dielectric interface and are not excited by transverse magnetic (TM) waves [2, 31].

2.1.3   Propagation of electromagnetic waves in the presence of scatterers

The SPR properties of bulk metal is not characterised by a single resonant frequency and depends on the frequency of the incident EM field. If the driving force provided by the incident light is insufficient, electrons do not undergo significant collective oscillation. In this case, $\omega > \omega_p$ and the dielectric function is positive, hence light will be transmitted (or absorbed) in intraband transitions (see Figure 2.1a) left side of the cube). The combination of the ω_p and intraband transmission or absorption gives rise to the metal's colour. However, if the incident light has a frequency which is smaller than the plasma frequency ($\omega < \omega_p$) the mobile electrons oscillate 180° out of phase with the incident EM radiation. In this case, the light-matter interaction is described by a negative dielectric function resulting in reflection (Figure 2.1a right side of the cube).

The frequency of incident light is only one of the many factors that affect the behaviour of the bulk metal's conduction electrons. As discussed previously, the complex dielectric function is also a critical factor. In contrast to light-bulk metal interactions, the interaction of an electromagnetic field with surface plasmon oscillations in a grating or prism structure is significantly different. This is particularly true if the frequency of incident light is less than the plasma frequency of the metal, in which case the real part of the dielectric function is negative (Figure 2.1b and c). At a specific angle of incidence, the incident photons will be absorbed, resulting in a dip in the transmission or reflection spectrum. Surface plasmon resonance may be classified as occurring in two distinct forms: SPP and LSP which are discussed in sections 2.1.4 and 2.1.5 respectively [32-34].
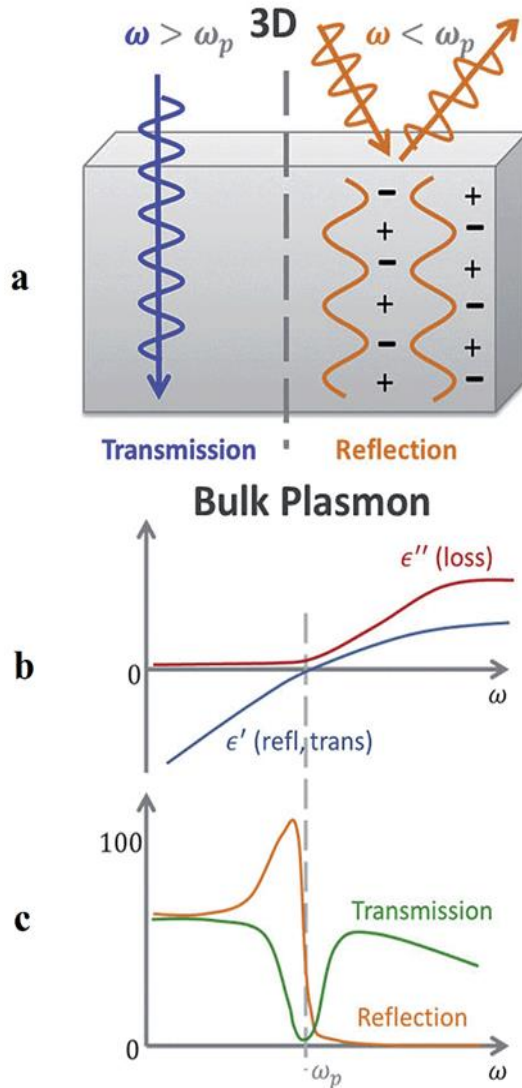
Figure 2.1 *a) schematic of bulk plasmon generation. Left side of cube: frequency of the incident light is above the plasma frequency, conduction electrons do not oscillate, and incident light is transmitted or absorbed. Right side of cube: the frequency of the incident light is smaller than metal plasma frequency, and the majority of the incident light is reflected. b) for ($\omega > \omega_p$) the real part of the dielectric function is positive and for ($\omega < \omega_p$) the real part is negative. c) plot describes the role played by the dielectric function in determining the oscillation of conduction electrons as a function of the frequency of the incident light. Figure adapted from Ref[35].*

2.1.4   The Surface Plasmon Polariton (SPP)

If one of the dimensions of a bulk of metal is reduced to the sub-wavelength scale (i.e. a thin metallic film on the order of nm), the oscillations of the free electrons will only occur at the metals surface. As discussed previously, if these oscillations are the result of coupling to an incident electromagnetic wave they are collectively described as surface plasmon polaritons (see Figure 2.2a). The word "polariton" refers to the propagation of the SP at the

film surface and interface (where $z = 0$). The SPP waves have considerable momentum compared to other waves of the same frequency. As a consequence, the associated SP waves are confined to the surface and the strength of the corresponding induced electric field decays exponentially in the direction of the surface normal. Therefore, SPP modes in thin metallic films are bound to the metal-dielectric interface and propagate along the interface until their energy is completely dissipated as heat in both media. At a specific angle, the incident photon will be absorbed, resulting in a dip in the transmission or reflection spectrum (Figure 2.2c) [35-38]. The resulting dispersion curve is shown in Figure 2.2b and is given by:

$$k_{spp} = \frac{\omega}{c} \sqrt{\frac{\varepsilon_m \, \varepsilon_d}{\varepsilon_m + \varepsilon_d}} \qquad (2.4)$$

where k_{spp} gives the resonance condition necessary to excite SPP at a metal-dielectric interface with permittivity of ε_m and ε_d respectively [37]. Here it is assumed that the incident field is *p*-polarized, and the z component is normal to the interface [29, 33, 39, 40].

The corresponding decay of the SPP field perpendicular (i.e. in the z-direction) to the interface is described by:

$$k_z^2 = k_{sp}^2 - \left(\frac{\omega}{c}\right)^2 \begin{cases} \varepsilon_d \\ \varepsilon_m \end{cases} . \qquad (2.5)$$
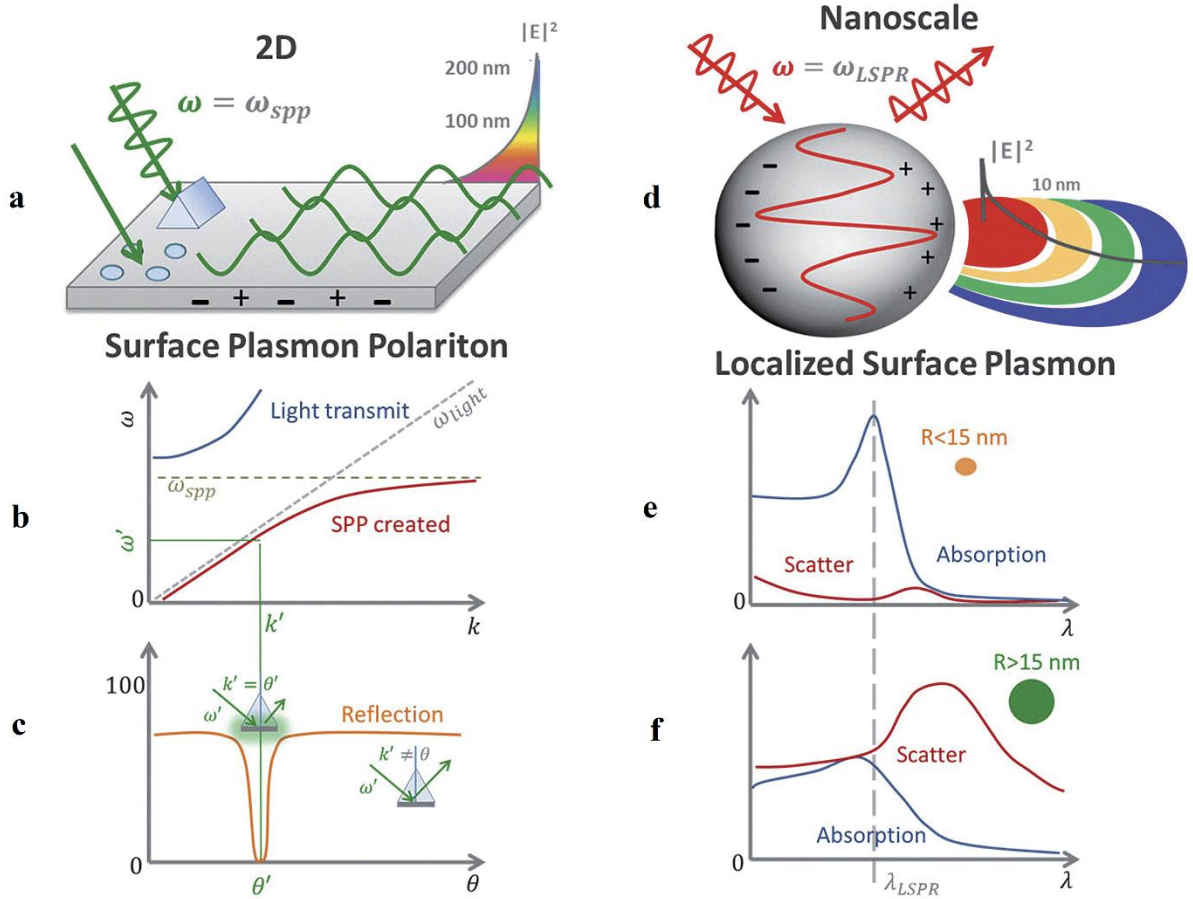
Figure 2.2 *Localised Surface Plasmon (LSP) and Surface Plasmon Polariton (SPP) a)*
SPPs are EM modes that arise from the interaction between light and the conduction band
electrons in a two-dimensional metallic film b) SPP dispersion curve c) Plot showing the
SPP angle where prism-coupling is used to generate SPPs d) LSPs are localised EM modes
that arise due to geometry confinement e) and f) Scattering and absorption properties for
nanoparticles of radius < 15 nm and > 15 nm respectively. The behaviour at the Localised
Surface Plasmon Resonance (LSPR) wavelength (λ_{LSPR}) is indicated by the vertical dotted
line. Figure adapted from Ref [35].

2.1.5   Localized Surface Plasmons (LSP)

In addition to a 2D metallic surface, SP excitation can be achieved using other geometries such as 0D particles or topologies with sizes smaller than the wavelength of the incident light. The electric field is approximately constant across features smaller than the wavelength of the incident light and therefore able to exert a uniform displacement force on the free electrons (Figure 2.2d). Due to the strong restoring force from the positively charged atomic nuclei, the electrons in the metal oscillate in a manner similar to a harmonic oscillator and cause the excited SPs to be confined to the local nanoscale features (i.e. LSPs) [41-43].

It should be emphasised that SPP and LSP polaritons are two different types of SP excitation. Whereas LSP is a confined/localised surface mode, an SPP is a propagating mode. The key characteristic of LSP resonance is that it depends on the size and shape (geometry) of individual sub-wavelength particles or features (e.g. pillars or apertures). By contrast, SPP field modes depend on the radiative losses associated with a metal film's thickness and surface roughness. If a metal film is thick, the SPP field has two independent enhancement modes. These enhancement modes degenerate if the metal is placed between two identical environments. The SPP wave is excited when both the frequency and wavevector of the incident light match the frequency and wavevector of the SPP resonance mode and decays exponentially from the surface. In contrast to SPPs, it is straightforward to excite LSP modes with the appropriate light frequency regardless of the incident light wavevector. The LSP mode typically decays via light emission.

The LSP frequency is given by:

$$\omega_{LSPR} = \frac{\omega_p}{\sqrt{(1+2\varepsilon_d)}} \tag{2.6}$$

As Eq. 2.6 shows, the LSP frequency may be shifted by changing the surrounding environment. Figure 2.2e shows how, at the LSPR wavelength (λ_{LSPR}), the absorption cross-section is several orders of magnitude larger than the individual particles size (given by $V = 4/3\,\pi R^3$). While Figure 2.2f shows for particles with R larger than 15 nm, the absorption cross section is almost smaller than scattering [41-43].

2.1.6   SP evanescent waves

As surface plasmons propagate, their associated electric field decreases exponentially in the direction perpendicular to the metal-dielectric interface. Because of this, SP are known as "evanescent" waves. In order to establish a frame of reference for EM wave propagation for this concept, we assume that the metal surface lies in the *x-y* plane and that the EM wave only travels in the *x-z* plane at a $\theta°$ angle of incidence. The transverse electric field (TE) and the transverse magnetic field (TM) components are thus parallel and perpendicular to the *x-y* plane, respectively.

The equation governing the propagation of an evanescent wave is:

$$E_{ev} = E_0 e^{-i(k_{spp}x-\omega t)}\, e^{-k_z z} \tag{2.7}$$

where the real part, $e^{-i(k_{spp}x-\omega t)}$, represents the propagation of the wave along the *x*-direction and the imaginary part, $e^{-k_z z}$, represents the evanescent decay in the *z*-direction. From the well-known dispersion relation, $k = \frac{\omega n}{c}$, the wavenumber for the transported wave k_T (assuming the SPP is travelling in the *x*-direction) within any media is given by:

$$k_T = \frac{\omega}{c}\begin{cases} n_d \\ n_m \end{cases} \tag{2.8}$$

where n_d and n_m are the refractive index for the dielectric and metal respectively. The *x*-component of the transported wave can be written as [29, 44]:

$$k_{(T,x)} = k_T \sin\theta \tag{2.9}$$

The corresponding *z*-component of the transported wave is given by:

$$k_{(T,z)} = k_T \, cos\theta_T.$$

(2.10)

These LSP modes have a narrow energy dispersion within the short wavelength regime, which is given by the relation [43]

$$E \cong \frac{E_0}{\pi} \frac{L}{t} \, cos\left(k_{spp}t + \frac{\pi}{2}\right)$$

(2.11)

where E_0 is the incident electric field, t is metal thickness, and L is the characteristic size of the subwavelength features.

2.1.7   SPP Length Scales

From the perspective of sub-wavelength optical components, SPPs can be represented by four dispersion length scales. These length scales are based on dielectric functions of media in contact with the metallic nanoscale particles or apertures. The oscillating nature of SPP mode and the E-field distributions corresponded to that are shown schematically in Figure 2.3 [28].

$$\delta_{spp} \approx \lambda_0 \frac{(\varepsilon'_m)^2}{2\pi\varepsilon''_m}$$

$$\lambda_{spp} = \lambda_0 \sqrt{\frac{\varepsilon_d + \varepsilon'_m}{\varepsilon_d \varepsilon'_m}}$$

$$\delta_m = \frac{1}{k_0} \left| \frac{\varepsilon'_m + \varepsilon_d}{\varepsilon'^2_m} \right|^{\frac{1}{2}}$$

$$\delta_d = \frac{1}{k_0} \left| \frac{\varepsilon'_m + \varepsilon_d}{\varepsilon_d^2} \right|^{\frac{1}{2}}$$

Figure 2.3 *Sketches of the oscillating nature of SPPs in a sub-wavelength metallic film with the four key length scales shown. The left-hand side shows the generation of oscillating SPP modes after interaction between incident light with wavevector k_0 and the perforated metallic film. The in-plane wave vector of the SPP along the propagation surface under appropriate boundary conditions gives the SPP wavelength, λ_{spp} . The right-hand side of the figure shows the imaginary part of the wavevector for SPP damping in two directions either side of the metal-dielectric interface. The equations describing the penetration (decay length) in the metal (δ_m) and dielectric (δ_d) are given in the two equations in the bottom-right. The sketches also show the SPP mode propagation length i.e. δ_{spp}, (top-right equation). Reprinted with permission from Ref [28, 45, 46].*

2.1.7.1 Energy propagation and penetration length

The SPP mode, characterised by its wavevector, k_{spp}, is complex ($k_{spp} = k'_{spp} + k''_{spp}$). The SPP wavelength can be derived from the real part of the dispersion relation:

$$\lambda_{spp} = \lambda_0 \sqrt{\frac{\varepsilon_d + \varepsilon'_m}{\varepsilon_d \varepsilon'_m}} \qquad (2.12)$$

The imaginary part of the SPP wave-vector describes the propagation length of the SPP i.e. δ_{spp}. This length scale is defined as the distance that the SPP travels before its power/intensity drops to $\frac{1}{e}$ of the initial value. The total energy, which is stored in an SPP wave is [28]:

$$U \sim |E|^2$$

$$= E_0^2 \, e^{2i(k_{spp}x - \omega t)}$$

$$= E_0^2 \, e^{2i(Re[k_{spp}]x - \omega t)} \, e^{2i^2 \, Im[k_{spp}]x}$$

$$= e^{-2 \, Im(k_{SPP})x} . E_0^2 \, e^{2i \, (Re(k_{spp})x - \omega t)}$$

where, $e^{-2Im[k_{spp}]x} = e^{-1}$, at the SPP propagation length giving

$$\delta_{spp} = \frac{1}{2Im[k_{spp}]} \qquad (2.13)$$

The corresponding imaginary part of the SPP wave vector is

$$k''_{spp} = k_0 \frac{\varepsilon''_m}{2(\varepsilon'_m)^2} \left(\frac{\varepsilon'_m \varepsilon_d}{\varepsilon'_m + \varepsilon_d}\right)^{\frac{3}{2}} \qquad (2.14)$$

and

$$\delta_{spp} = \frac{1}{2} k''_{spp} \qquad (2.15)$$

If the metal has minimal losses, and $|\varepsilon'_m| \gg |\varepsilon_d|$, then δ_{spp} can be approximated as:

$$\delta_{spp} \approx \lambda_0 \frac{(\varepsilon'_m)^2}{2\pi \varepsilon''_m} \qquad (2.16)$$

2.1.7.2 SPP skin depth (decay length)

Perpendicular to the propagation direction, i.e. the *z*-direction (in both metal and dielectric), the wavevector k_z may be defined in both media i.e. $k_{d,z}$ and $k_{m,z}$ for the dielectric or metal respectively. The penetration depth of the field into the metal and dielectric media are found by considering the SPP dispersion relation. Here the z-direction is the orthogonal direction to the plane in which the SPP propagates. The wave-vector of light travelling in materials with a relative dielectric function ε_i is given by $\varepsilon_i k_0$ (in the metal $\varepsilon_i = \varepsilon_m$ and in the dielectric $\varepsilon_i = \varepsilon_d$) [28, 47]:

$$\varepsilon_i k_0^2 = k_{(spp,x)}^2 + k_{(z)}^2$$

$$k_d = k_0 \sqrt{\varepsilon_d - \frac{\varepsilon_d \varepsilon_m}{\varepsilon_d + \varepsilon_m}}$$

$$= k_0 \sqrt{\frac{\varepsilon_d^2}{\varepsilon_d + \varepsilon_m}} \tag{2.17}$$

Similarly,

$$k_m = k_0 \sqrt{\frac{\varepsilon_m^2}{\varepsilon_d + \varepsilon_m}} \tag{2.18}$$

The z component of the field in both the dielectric and the metal is imaginary and describes the exponential decay of the field intensity in both media. The corresponding decay lengths are:

$$\delta_m = \frac{1}{2Im[k_z]}$$

$$= \frac{1}{2k_0 Im \left[\sqrt{\frac{\varepsilon_m^2}{\varepsilon_d + \varepsilon_m}} \right]}$$

$$= \frac{\lambda_0}{4\pi} \; Im \; [\sqrt{\frac{\varepsilon_d + \varepsilon_m}{\varepsilon_m^2}}]$$

$$\delta_d = \frac{\lambda_0}{4\pi} \; Im \; \left[\sqrt{\frac{\varepsilon_d + \varepsilon_m}{\varepsilon_d^2}}\right] \approx \frac{\lambda_0}{4\pi} \; [\sqrt{\frac{|\varepsilon_m|}{\varepsilon_d^2}}] \qquad (2.19)$$

where δ_m and δ_d are the field skin depth (decay length) in the metal and dielectric, respectively [28].

2.1.8   Extraordinary optical transmission of light (EOT) theory

At the end of the twentieth century Ebbesen at al. observed a higher transmitted signal from light propagating through a periodic array of sub-wavelength apertures in thin metallic films than was predicted classically. This phenomenon was termed Extraordinary Optical Transmission (EOT) and could be understood by considering the SPs generated within the structure by coupling of free electrons and incident photons [48]. Since the first experimental demonstration EOT, a vast amount of experimental and theoretical work has been devoted to researching a range of novel applications based on photonic devices that exhibit this phenomenon. Two applications in particular which are most relevant for this thesis are plasmonic optical colour filters [49-54] and chemical and molecular sensors [55-57].

2.1.8.1 Microscopic theory of EOT and derivation of SPP coupled mode equation

Extraordinary Optical Transmission involves the excitation of a surface electromagnetic (EM) Bloch mode (modes of Bloch waves) at a metal-dielectric interface perforated by 2D holes [58, 59]. The result of this excitation is the enhanced transmission of light through the apertures which make up the periodic array of 2D holes [49, 50, 55, 60-64]. Figure 2.4 displays the elementary scattering events which occur within a periodic 2D array of sub-

wavelength apertures with a fixed periodicity assumed in both the x- and y-directions. The metal-dielectric interface is illuminated by light represented by an incident plane wave $(\psi_{PW}^{-}(k))$. This incident plane wave has an associated wave vector, $k = k_x x - k_z z$, as shown, the y component of k is null ($k_y = 0$). During interaction of the incident light and the perforated metallic film (which has a dielectric constant $= \varepsilon_m$) a portion of the light is reflected or scattered, a portion is transmitted, and some of the light is absorbed and induces excitation of SP within the nanohole array. The coupled-mode equations (characterised by scattering coefficients, A_n and B_n, and excitation coefficient, C_n) for the nth hole are calculated by using the "Lorentz reciprocity theorem" and "vectorial method" [63]:

$$A_n = M_n \beta(k_x) + u_n \tau A_{n-1} + u_{n+1} \rho B_{n+1} \qquad (2.20)$$

$$B_n = M_n \beta(-k_x) + u_{n+1} \tau B_{n+1} + u_n \rho A_{n-1} \qquad (2.21)$$

$$C_n = M_n t(-k_x) + u_n \propto A_{n-1} + u_{n+1} \propto B_{n+1} \qquad (2.22)$$

where ρ and τ are the reflectance and transmittance coefficients respectively and $u_n = \exp(ik_{SPP}a_n)$ describes the phase delay and $M = w_1 w_2 \ldots w_n$ $(n > 0, M_0 = 1)$ the phase retardation for incident light at the nth hole with $w_n = \exp(ik_x a_n)$. Also, $\propto$ and β are scattering coefficients of the fundamental Bloch mode and outgoing plane wave, respectively [65]
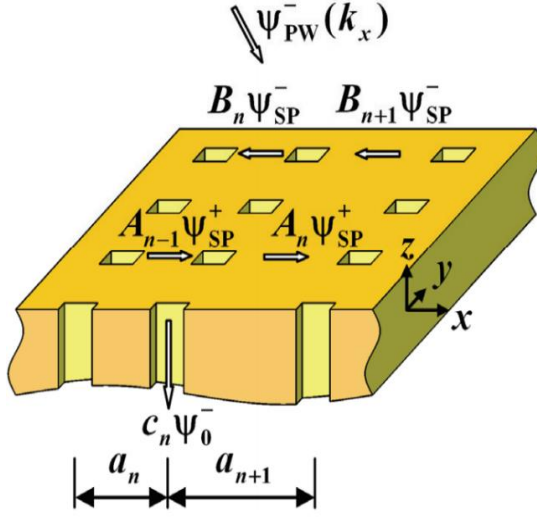
Figure 2.4 *Schematic of light incident on a metallic aperture array. The metal surface is illuminated by a plane wave ($\psi_{PW}^-(k_x)$) which results in 3 distinct components ψ_{SP}^+, ψ_{SP}^- and ψ_0^- after interaction. The Bloch mode propagates in the negative z-direction. A_n and B_n are the scattering coefficients of the surface waves, C_n is the excitation coefficient [65].*

Interestingly, EOT phenomena associated with light propagating through 2D subwavelength holes causes non-radiative SPRs to re-radiate photons in visible range [10, 22]. In Figure 2.5(a-c) six elementary scattering process are shown as being involved in the interaction between the EM wave and the "pure" SPP coupled mode. These occur on the surface and at the front and rear face of the metal film which is perforated by the periodic array. These six scattering coefficients characterising the SPP modes involved in EOT are [65]:

- ρ, the SPP modal reflectance coefficient
- τ, the SPP model transmittance coefficient
- $\propto$, the scattering coefficient from the SPP mode to the fundamental Bloch mode (and vice versa)
- $t(k_x)$, the transmission coefficient of the fundamental Bloch mode
- $r(k_x)$, the reflection coefficient of the fundamental Bloch mode
- $\beta(k_x)$, the scattering coefficient from the SPP mode to the outgoing plane wave
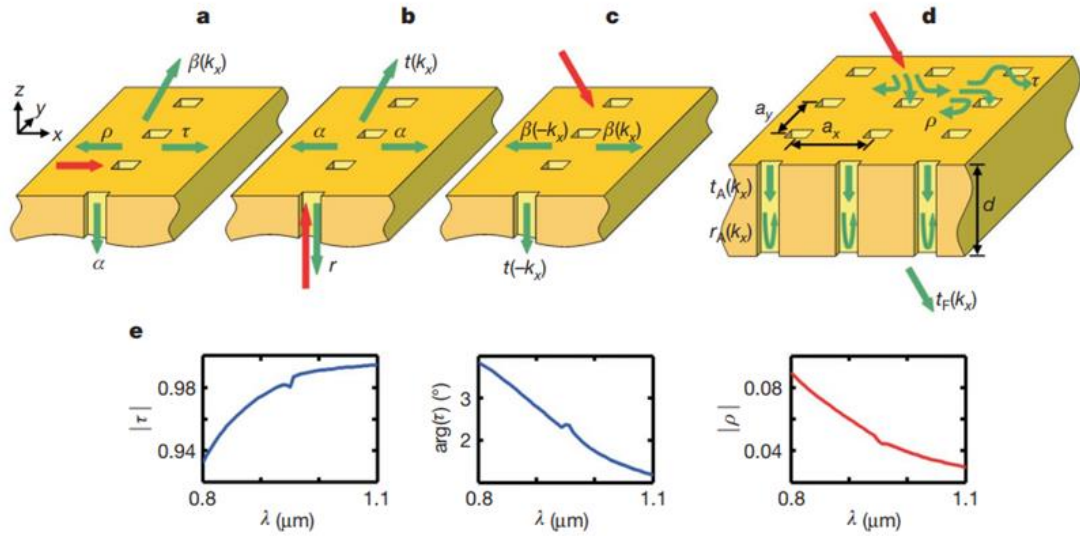
Figure 2.5 *The elementary scattering process (optical transmittance (τ) and reflectance (ρ)) from a "pure" SPP coupled-mode for a periodic 1D array of holes involved in EOT. The red arrows refer to incident light direction, and the green arrows show the scattered mode direction on the surface and at the front and rear of the interface: a) Scattering (τ or ρ) from the SPP mode due to the interaction of a normal incidence EM wave and SPP in a 1D hole chain and scattering coefficient, β, to the outgoing plane wave b) The transmittance and reflectance coefficients $t(k_x)$ and $r(k_x)$ for the fundamental Bloch mode at the front and rear of the interface c) Scattering according to the reciprocity theorem d) Fully periodic structures with the same periodicity in both the x and y-directions for the scattering of the fundamental Bloch model e) Wavelength dependence of the transmission and reflectance coefficients of a single chain under normal incidence light. Adapted from Ref [65].*

The combination of these six scattering coefficients results in a closed-form expression for the scattering process of the fundamental Bloch mode (see Figure 2.5d). For simplicity, consider a fully periodic structure with an infinite number of holes ($N = \infty$) and equal periodicity in both the x and y-directions ($a_x = a_y = a$) irradiated by a normal incidence plane wave ($k_x = 0$). In this case: $A_n = wA_{n-1}$, $B_n = wB_{n-1}$ and $C_n = wAC_{n-1}$. Therefore, considering the pseudo-periodic conditions for the SPP-coupled mode, the transmittance and reflectance coefficients, $t_A(k_x)$, and $r_A(k_x)$ of the fundamental Bloch mode supported by the 2D hole array are given by:

$$t_A(k_x = 0) = t + \frac{2\propto\beta}{u^{-1}-(\rho+\tau)} \tag{2.23}$$

$$r_A(k_x = 0) = r + \frac{2\propto^2}{u^{-1}-(\rho+\tau)} \tag{2.24}$$

where $u = \exp(ik_{SPP}a)$ is the phase delay, $t = t(k_x = 0)$, $\beta = (k_x = 0)$, and $k_{SPP} = k_0\sqrt{\frac{\varepsilon_m\varepsilon_d}{\varepsilon_m+\varepsilon_d}}$ defines the complex propagation constant of the SPP at the metal-dielectric interface. Figure 2.5e, shows the dependency of the transmission and reflectance coefficients of a single chain under normal incidence light on the wavelength [65].

2.1.9   Theory of WOOD'S anomalies

Grating anomalies (discovered by R.M. Wood in 1902) can be observed as a pattern of unusual dark and light bands in the reflected spectrum of a metallic diffraction grating using a white light source. This phenomenon appears over a range of wavelengths that were smaller than the grating pitch when the magnetic field is parallel to the grating line, i.e. P-polarization [66-68].

Figure 2.6 shows the dark bands in a reflected spectrum collected using a continuous light source for different angles of incidence obtained by Wood. Two dark bands are

observed in all the diffracted spectra; as the incident angle decreases, these dark bands

begin to merge, and finally, at normal incidence, a uniform illumination appears [69].
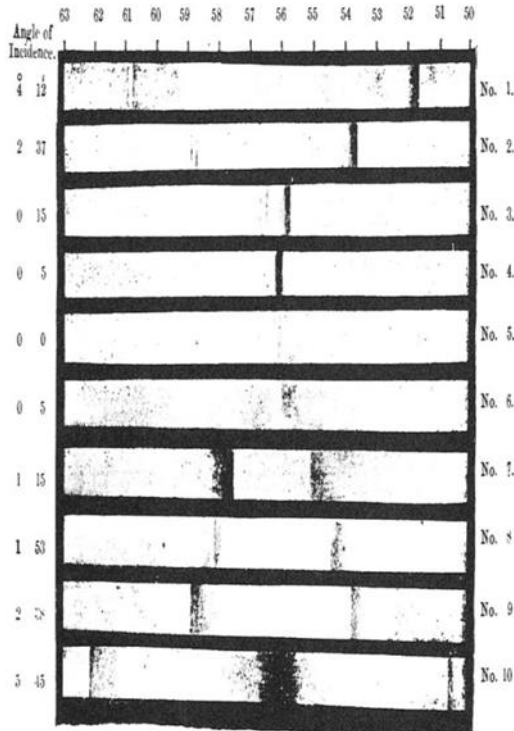
Figure 2.6 Diffracted spectra of the continuous light source reflecting off a metallic grating, pitch = 1760 nm, images obtained by Wood. The left-hand side numbers indicate the angle of incidence and the top numbers the reflected wavelength in nanometres. Reprinted with permission from Taylor & Francis Ltd (http://www.informaworld.com).

Initial efforts to interpret these anomalies began in 1907 by Rayleigh starting with his

famous grating formula [70]:

$$\sin(\theta_n) = \sin(\theta) + \frac{n\lambda}{d} \qquad (2.25)$$

where θ_n and θ are the angle of diffraction and incidence respectively, λ is wavelength in

vacuum, d is the distance between the groves (also known as the pitch) and n is the

scattering order. Rayleigh's "dynamical theory of the grating" was based on an expansion

of the scattered electromagnetic field by only considering the outgoing waves. Rayleigh's

theory was a success in that it successfully predicted the major experimental observations of the time. However, a major limitation of Rayleigh's theory was that it did not account for the shape of the dark bands which were observed to correspond to the anomalies. To address this an in-depth theoretical treatment of Wood's anomalies was proposed by Fano [49, 50, 71-73]. This theory successfully predicted the following features:

- A sharp anomaly dependant on the wavelength, governed by Rayleigh formula

- A diffuse anomaly related to "leaky" (complex) waves — which consisted of both a minimum (near red wavelength regime) and a maximum of intensities. This type of anomaly was observed by Wood and is shown in Figure 2.6.

Palmer later classified these anomalies as 'S-type' (*E*-mode incidence) and 'P-type' (*H*-mode incidence), with P-type anomalies only appearing when the metallic grating had deep grooves and S-type appearing when the grating had shallow grooves [74]. The availability of new sources of light such as the laser at the beginning of the 1970s, offered opportunities to make more accurate, submicron size, holographic gratings for investigation of Wood's anomalies in both the visible and near-infrared regions [55]. This in turn led to further refinements in the theory of Wood's anomalies including an expression describing the "excitation of electromagnetic evanescent waves" for metallic gratings surface by Rudolph and Schmahl at the beginning of the 1970s. Further research conducted by Maystre in 1972 was able to more accurately quantitatively predict the experimental observations [62, 75]. The theory of Wood's anomalies is still being investigated today with modern fabrication techniques permitting the investigation of SPPs in microscopic structures produced via nanofabrication [76-78].

2.1.10   The microscopic SPP model and phase matching (Fabry- Pérot equation)

The microscopic SPP model and phase-matching condition explains how EOT resonant peaks are formed for a periodic array of apertures and their position in the transmission spectrum. In order to determine the location of these SPP resonant peaks, Lalanne et al. derived the zeroth-order of the transmittance coefficient, $t_F(k_x)$ based on the Fabry-Pérot equation [65, 79]. This coefficient can be conveniently expressed as a wavelength dependant function, $T(\lambda)$, as:

$$T(\lambda) = |t_F(k_x)|^2 \tag{2.26}$$

where $k_x = \left(\frac{2\pi}{\lambda}\right) \sin \theta$. In comparison to normally incident EM waves ($k_x = 0$), waves which are incident from an oblique angle ($k_x \neq 0$) incorporate an additional phase-shift term. For each of these two conditions resonance is achieved when:

$Re\left(k_{sp}\right)a_x + \arg(\rho + \tau) = 0$ for normal incidence condition

$Re\left(k_{sp}\right)a_x + \arg(\rho + \tau) \approx k_x a_x$ for general phase-matching condition

where a_x is the hole periodicity and $k_x a_x$ describes the phase shift, also the function '$arg(\rho + \tau)$' refers to the argument of $(\rho + \tau)$ which is slightly positive but not zero. The positive phase delay in the SPP mode is due to the metal having a slightly lower effective conductivity, i.e. $n_{eff}^2 \approx \frac{D}{a_y}\varepsilon_{air} + (1 - \frac{D}{a_y})\varepsilon_{metal}$, where D is the film's thickness. The weak phase delay is then described by:

$$\arg(\tau) = [k_0 Re\left(n_{eff}\right) - Re\left(k_{spp}\right)]D \tag{2.27}$$

Lalanne et al. compared the results from the SPP model and "rigorous coupled-wave analysis" (RCWA) for a gold film perforated by hole chains with equal periodicity on both the x and y-directions. Despite some differences between the results from the SPP model and computational RCWA the SPP model was able to quantitatively predict the resonance peaks in the transmission spectrum oblique incidence [65].

2.2 Experimental background

Having reviewed some of the theoretical concepts underpinning this thesis, this section describes some of the main concepts behind the experimental techniques employed in this thesis.

2.2.1   Ion implantation

Ion implantation (Chapter 5) can be defined in terms of two key quantities: dose (amount of dopant implanted) and ion energy (the final depth of the dopant from the surface of the substrate). There are two primary stopping mechanism when the ion enters the target; the first one involves the transfer of the ion's energy to the target's nuclei (which results in a deflection of the projectile ions and displacement of the nuclei) and the second one is the interaction of the ion with the target's free and bound electrons. Nuclear stopping causes physical damage and produces defects in the lattice whilst electronic stopping results in vacancy-interstitials being formed. The number of displacements per target atom per unit time is described by the Kinchin-Pease relation [80-83]

$$P(x) = \frac{0.8}{2NE_d} \left(\frac{dE}{dx}\right)_n \Phi \tag{2.28}$$

where Φ is the ion flux, N is the target density, E_d is effective threshold displacement

energy and $\left(\frac{dE}{dx}\right)_n$ is the ion energy per unit depth. It is important to note that replacement

reduces the number of vacancies that remain after the collision with the recoil atoms. The

total distance travelled by the ion before stopping is called ion range (ion implantation

depth) and is determined by

$$R = \int_0^R dx = \frac{1}{N} \int_0^{E_0} \frac{dE}{S_n(E) + S_e(E)} \qquad (2.29)$$

where N is the density of the target, E_0 is the initial energy of the ion (known as the

acceleration voltage in keV), and S_n and S_e are nuclear and electric stopping power

respectively. In the current study, the total displacement and range of the ion in the target

lattice was calculated by using the stopping and range of ions in matter (SRIM) software

[82, 83]. The SRIM program is based on Monte Carlo simulations and can give insights

into the ion implantation area both parallel and perpendicular to the targets surface (see

Chapter 5).

The ion fluence can be calculated using:

$$\Phi = \frac{Dose\ [\frac{pC}{cm^2}]}{e\ [C]} \qquad (2.30)$$

The corresponding dependence of the density of implantation-induced defects,   C

($defects/cm^3$), on the ion fluence ϕ ($ions/cm^2$) is given by [84]:

$$C = A\phi^n \qquad (2.31)$$

where n is 1 for a linear accumulation of the damage and A is the concentration of impurities

(both ions and vacancies).

2.2.2   Maxwell Garnett mixing formula

Traditionally Lorentz molecular theory is derived from the macroscopic Maxwell's equation, and therefore it cannot directly be employed for calculating macroscopic quantities such as the permittivity of a composite. However, The Maxwell Garnett mixing formula considers both the electric and magnetic dipole moments inside a composite material. The starting point for modelling a complex, homogeneous, electromagnetic medium is 'homogenization theory'. Within this theory the effective permittivity, ε_{eff_G}, of such the composite is giving by the following mixing formula [85, 86]:

$$\varepsilon_{eff_G} = \varepsilon_h \frac{1+2f\frac{\varepsilon_i-\varepsilon_h}{\varepsilon_i+2\varepsilon_h}}{1-f\frac{\varepsilon_i-\varepsilon_h}{\varepsilon_i+2\varepsilon_h}} = \varepsilon_h \frac{\varepsilon_h+\frac{1+2f}{3}(\varepsilon_i-\varepsilon_h)}{\varepsilon_h+\frac{1-f}{3}(\varepsilon_i-\varepsilon_h)} \tag{2.32}$$

This equation is used to predict the dielectric properties of ion implanted TiO_2 in chapter 5.

2.2.3   Self-Assembled Monolayers (SAM) on metallic surfaces

Self-assembled monolayers (Chapter 6) are of immense importance and interest in surface science in part due to their ability to tailor the surface chemistry of metals. However, the direct characterisation and detection of self-assembled monolayers (SAMs) is often challenging because of the inherently small dimensions of these systems (typically only several nm). Techniques and methods, such as atomic force microscopy (AFM) [87], Fourier transmission infrared spectroscopy (FTIR) or ellipsometry [88, 89] that have historically been used to observe SAM formation, for example, are typically invasive, costly, and cumbersome. Therefore, there is significant interest in the research and development of alternative techniques that are both passive and provide rapid results. Plasmonic devices for sensing SAMs have gained significant attention due to their ease of operation and extreme sensitivity to changes in the near-surface dielectric properties of the surrounding media [90-93].
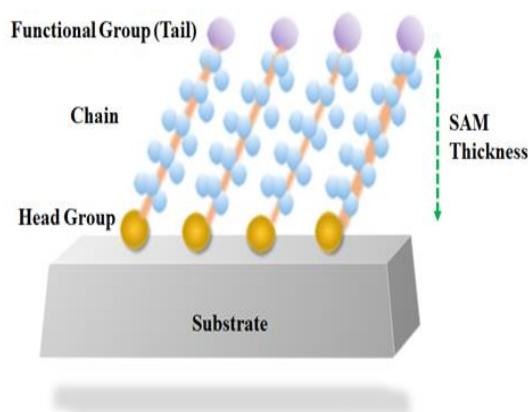
Figure 2.7 *Schematic of a fully assembled thiol-SAM on a metallic surface, showing the attached head group, carbon chain, and the functional group. Due to the asymmetry of the CH_2- distribution in the carbon chain, the molecules are slightly tilted with respect to the surface.*

Formation of SAMs on surfaces usually takes place from solutions or from vapor phases that contain a carrier (solution) with the molecules of interest and is considered to be a stochastic, dynamic process [94]. The chemical group responsible for the attachment of a SAM to a surface is called the "head group" whilst the chemical group at the other end of the carbon chain which can be chemically altered is called the "functional group". At the end of the self-assembly process, a close-packed layer with a thickness of ~ molecule length × *sin* (tilt angle) is formed. This is often slightly tilted with respect to the surface due to the mechanism of head-group reaction and the asymmetry of the CH_2- radicals in the carbon chain [95-97]. Figure 2.7 shows a schematic of a fully assembled SAM on a metallic substrate.

In nature, the most important driving force for monolayer formation by self-assembly is the interaction force between molecules or atoms of surfactant and the surface. Surfactants, also known as "surface active agents", are a special kind of molecule with both a hydrophobic tail group and a hydrophilic head group. They play a critical role in the formation of self-assembled monolayers. Surfactants are able to absorb on a surface, even

at relatively low concentrations, due to special properties of their hydrophilic tail. When surfactants are present on a surface or interface, the hydrophobic interactions between the tail group and the surface causes the surface energy to be drastically reduced. On the other hand, the surfactants' head group plays a critical role in the function of SAM as a sensor. The large variety of available head groups, each having a different charge, size, and chain length makes SAMs an attractive option for surface engineering.

In general, depositing a self-assembled monolayer on a metal's surface creates a protective barrier between the environment and the metallic surface as well as introducing additional functionality. The thiolate alkyl chains comprise both a hydrophobic tail group to create a monolayer onto the metal substrate and a hydrophilic head group. Although the functionality of the monolayer is largely determined by the hydrophilic head group, several different functional groups also contribute. Examples of functional groups which chemically react with head groups are carboxylic acid, phosphate and sulphate.

2.2.3.1 The Effective Refractive Index of SAMs

The effective refractive index, n_{eff}, of SAMs can be determined by calculating the integrated RI through the structure with respect to depth from the surface, i.e.[98, 99]

$$n_{eff} = \left(\frac{2}{\delta z}\right) \int_0^\infty n(z) \exp\left(\frac{-2z}{\delta z}\right) dz$$

where

$$n(z) = n_T \quad \text{for} \quad 0 < Z < d_T$$

and

$$n(z) = n_s \quad \text{for} \quad d_T < Z < \infty .$$

This results in a final effective RI of the SAM of:

$$n_{eff} = (n_T - n_s)[1 - \exp\left(\frac{-2t_{SAM}}{\delta z}\right)] + n_s \tag{2.33}$$

here n_T is the thiol refractive index and n_s is the refractive index of the dilute thiol solution (usually thiol dissolved in ethanol); t_{SAM} is the thickness of SAM which is less than or equal to the length of the thiol.

During SAM formation, the dielectric function of the adlayer (the thiol which is assembled on the metal substrate) changes as a function of time. These changes can be detected using plasmonic sensors by measuring the intensity of the transmitted light or by measuring the shift of the resonance peaks at different time points. The dielectric constant will continue to change until complete coverage is achieved on the surface.

2.2.3.2 SPR Response and Sensitivity Factor

SPR response, R, is a term which is often used to describe the sensitivity of a plasmonic device based on the SPR wavelength shift, $\Delta\lambda$. We note that R is also often used to denote reflectivity in optics; however, in context of SPR sensors, it represents the shift in the wavelength of the resonant peak positions. R depends on both the sensitivity, S, (see Chapter 1, section 1.5) and refractive index variation (ΔRI) of the medium in contact with the metal surface [99]:

$$R = S\Delta RI \tag{2.34}$$

Through the sensitivity, R varies as a function of the shift in the wavelength of the resonant peak position (i.e. $R \propto \lambda_2 - \lambda_1 = \Delta\lambda$). If the peak shift is linear with changes in the RI then R associated with the SAM can be defined as

$$R = S\,(n_{eff} - n_d\,)$$

$$R = S\left((n_{Thiol} - n_d)[1 - \exp\left(\frac{-2t_{SAM}}{\delta z}\right)]\right) \tag{2.34a}$$

If the peak shift is quadratic (nonlinear) then R is defined as

$$R = S_1 \left(n_{eff} - n_d\right) + S_2 \left(n_{eff} - n_d\right)^2$$

$$R = S_1 \left((n_{Thiol} - n_d)[1 - \exp\left(\frac{-2t_{SAM}}{\delta z}\right)]\right) + S_2 \left((n_{Thiol} - n_d)[1 - \right.$$

$$\left. \exp\left(\frac{-2t_{SAM}}{\delta z}\right)]^2\right) \qquad\qquad (2.34b)$$

here n_{eff} is the properly weighted average of the refractive index of the thiol

(n_{Thiol}) which is attached to the metal surface plus the refractive index of the medium

(n_d). The constants, S_1 and S_2, can be determined from the calibration curve. In this study,

the medium, d, was air/water/ethanol or a dilute solution of SAM. During the experiment

studying SAM formation, $\Delta\lambda$ was frequently measured at different time intervals to

characterise variations in R [99]. In the case of highly-ordered SAMs, at full coverage, the

thickness of the monolayer (t_{SAM}) is similar to the length of the thiol. For partial coverage,

t_{SAM} is smaller than the length of the thiol.

2.2.3.3 Determining SAM Thickness from the SPR Response

To estimate the thickness of the SAM (assuming t_{SAM} is very small compared to δz) we

can use the following equation based on the SPR response [99]:

$$t_{SAM} = -\left(\frac{\delta_z}{2}\right) \ln\left(1 - \frac{R}{R_{max}}\right) \qquad\qquad (2.35)$$

where R_{max} is the maximum response which for thiols is defined as:

$$R_{max} = S(n_{Thiol} - n_d). \qquad\qquad (2.36)$$

2.2.3.4 Determining the Thiol coverage from the SPR response

Equation 2.35 can be used to estimate the average SAM thickness within the area of the sensor. Once t_{SAM} is calculated, it can be converted to surface concentration or coverage, C_{Thiol}, normally quoted as molecules/nm^2 [100]. To convert from t_{SAM} to C_{Thiol} it is necessary to multiply the former by the thiol density, N, which should be in units of molecules/nm^3, i.e.

$$C_{Thiol} = t_{SAM} \times N \tag{2.37}$$

where

$$N = \frac{\rho}{m} \times N_A \tag{2.38}$$

where ρ is the thiol density in g/cm^3, m, is the molecular weight and N_A is Avogadro's constant.

2.3 Overview of experimental methods

This section focuses on the nanofabrication tools used for this thesis and describes the procedures and methods for generating a wide range of metallic nanostructures.

2.3.1   Nanofabrication via Focused Ion Beam (FIB)

During the late 1970's Levi-Setti, Orloff and Swanson, developed the focused ion beam (FIB) based on field emission technology. Development continued during the early 1980s and the first commercial FIB setup was introduced in the early 1990s for use in the semiconductor industry. Gradually FIB has become increasingly widespread and is now used for research in a large range of different areas including material science, failure analysis, and for chip design. The FIB enables localized milling at high precision ranging from a few nanometres to hundreds of microns by using a focused beam of ions.

In FIB nanofabrication, appropriate gases are localised at the sample surface to carry out either subtractive or additive lithography through sputtering or decomposition respectively without using any mask. The chemical reactions between the ion beams and the target surface generate both secondary electrons and ions; therefore, FIB can be used for imaging, milling or deposition progress during nanofabrication [101]. What follows is a description of the essential elements in the FIB system and a description of its basic operation.

The FIB setup system looks and operates in a way which has many similarities with the scanning electron microscope (SEM). Whereas SEM relies on a focused electron beam for imaging the target surface, FIB utilises an ion beam. The essential components of the FIB setup are shown in Figure 2.8. A liquid-metal ion source (LMIS) is used to emit ions and focus them onto the surface of the target. Typically, an ion beam is generated from liquid gallium by application of a high electric field ($10^8 \, V/cm$). The use of gallium is in part due to its low melting point which means it exists in the liquid state at room temperature. This reduces the need for high temperatures to heat the source and increases the source lifetime. A substantial voltage ($7000 \, V$) extracts positively charged ions from a reservoir of liquid gallium. Ga^+ ions are emitted towards a very sharp tungsten needle (radius ~ 5-10 nm). The final focused ion beam diameter at the target surface depend on (i) the extraction voltage, (ii) the strength of the electrostatic lenses, (iii) lens aberration, (iv) the lateral ion repulsion effect, and (v) the aperture size. The ion beam energy and current can be varied by changing the aperture size. These apertures control the beam size to achieve either a low current for high-resolution, non-destructive imaging or slow sample milling, or a high-current for rapid sample milling. An upper magnetic octupole is used for controlling the beam astigmatism and a lower one for raster scanning the beam in a user-defined pattern [102].

65
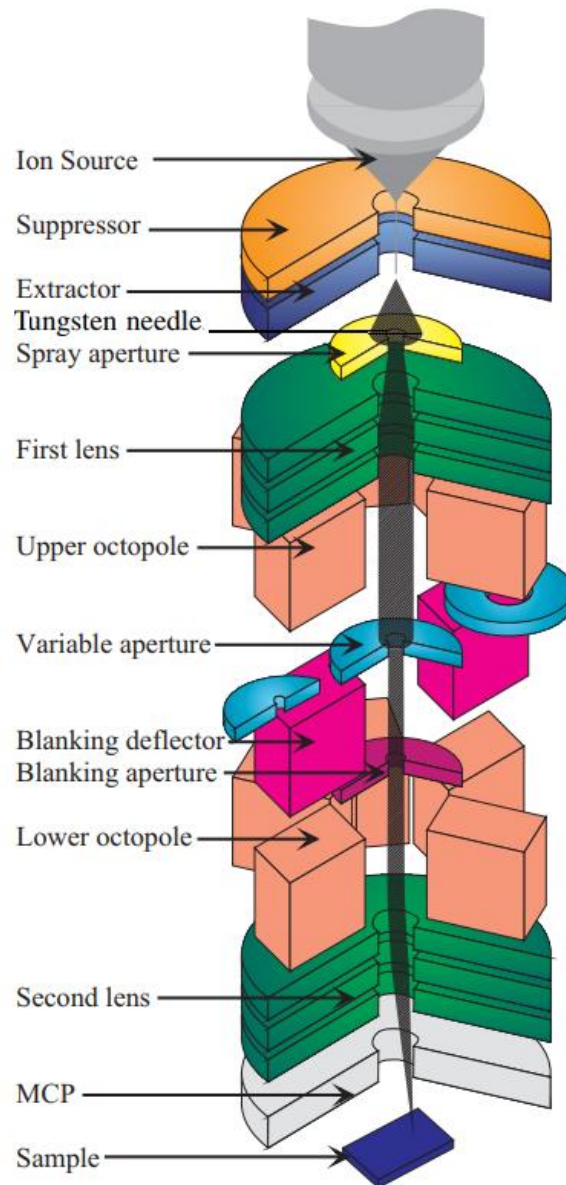
Figure 2.8 *Schematic diagram of the essential elements of the FIB. Adapted from Ref [102].*

2.3.2   Fundamental principle of FIB imaging, milling and deposition

The most important physical effects of the incident energetic ion stream on the substrate are:

I.   Electron emission (used for imaging). The transfer of energy from the final focused ion beam to atoms at the sample surface cause secondary particles (electron, ion, neutral atom) to be ejected from the substrate. The multichannel plate (MCP) collects secondary electrons and ions for imaging. The measured signal directly depends on the ion beam energy, current, and the incident angle of the beam. In addition, the imaging efficiency also depends on the targets' atomic structure (chemical bonding) and orientation. Figure 2.9a shows how the target is raster scanned whilst the MCP collects the secondary particles. The resolution of FIB images is determined by the final focused ion beam diameter. It should be noted that the quality of FIB images can be impacted by damage to the sample caused by the LMIS and by unwanted Ga^+ ion implantation during raster scanning for imaging. To ameliorate these issues during FIB imaging a fine ion beam (low ion current) is used to scan the target.

II.   Substrate atoms are sputtered from the target surface (ion milling). In contrast to FIB imaging, milling uses a high ion current beam as shown in Figure 2.9b. Energy from the incident ion is transferred to the target atoms and causes physical sputtering of material from the substrate. An arbitrary pattern is then etched during raster scanning across the surface. The sputtering yield refers to final focused ion beam energy, beam current, and target chemical structure. For instance, it is shown in table 2.1 the sputtering yields are different for various materials (data obtained by using Monte Carlo simulations[101]). The minimum dimensions of the milled pattern is equal to the size of the ion beam diameter.

	Implantation Depth (nm)			Sputtering Yield (atoms/ion)			
Ga$^+$ ion energy	Si	SiO$_2$	Al	Si	SiO$_2$		Al
					Si	O	
10 keV	13 ± 5	12 ± 4	11 ± 4	1.46	0.62	2.23	2.59
20 keV	20 ± 7	19 ± 6	17 ± 6	1.89	0.64	2.34	2.98
30 keV	27 ± 9	25 ± 8	23 ± 8	1.98	0.67	2.25	2.91
40 keV	33 ± 11	31 ± 10	29 ± 10	2.04	0.77	2.54	2.54
50 keV	39 ± 14	38 ± 11	35 ± 12	2.01	0.67	2.39	2.48

Table 2.1 *Sputtering yields for Si, SiO$_2$ and Al. Adapted from Ref [101]*

III.　　Molecular dissociation (deposition). FIB can be used to induce deposition of both metals and insulators at high spatial resolution. Typically, platinum and tungsten are deposited as the metal and SiO$_2$ as the insulator. The deposition process is completely maskless and utilises chemical vapour deposition (CVD). In Figure 2.9c, a simple schematic of the deposition process is shown. Inside the chamber, an organic precursor gas (in the case of tungsten, W(CO)$_6$, and for SiO$_2$ usually oxygen or water) is sprayed by a nozzle onto the target surface (silicon for SiO$_2$). In the second step, the precursor gas adsorbed on the target surface is decomposed using focused ion beam resulting in volatile reaction products being released and removed from the surface via the vacuum system. Finally, a thin layer of the desired reaction product (Pt, W or SiO$_2$) is deposited on to the target surface [101-104].
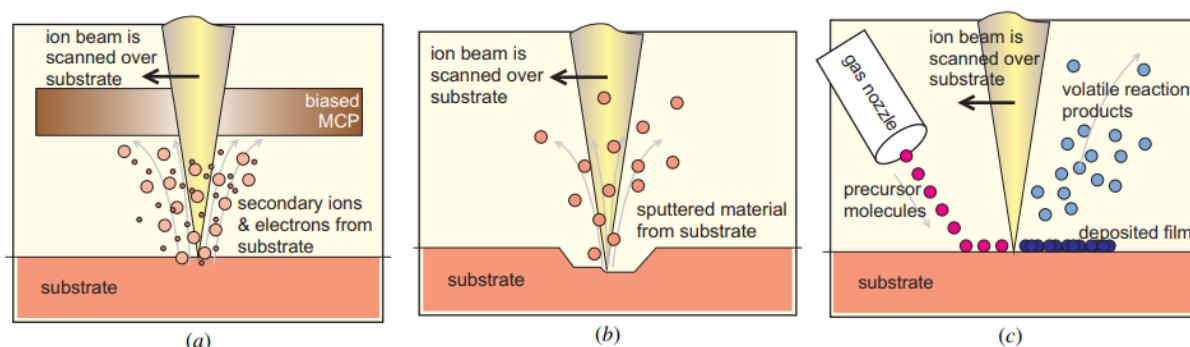
Figure 2.9 *Basic principle of FIB. a) Electron emission (imaging), b) Substrate atom sputtering (milling) c) Molecule dissociation (deposition). Adapted from Ref [102].*

2.4 Electron Beam Lithography

Electron beam lithography (also known as E-beam lithography or simply EBL) is a high-performance nanolithography technique, which offers a wide range of solutions for creating nanoscale size patterned samples. EBL has the benefit that it affords extremely high, diffraction-limited resolution, and versatile pattern formation over relatively large areas. The EBL system consists of two distinct fabrication methods: direct writing and projection printing.

The first fabrication method using the electron microscope mainly developed during the early 1960s with the first useful structures fabricated and tested in 1964 [105]. The first commercial EBL instrument with linewidths beyond the resolution of conventional optics was introduced in 1969 [106]. What follows is a description of the EBL process, which include direct writing and projection printing techniques as well as an outline of the basic components of the EBL system [105-108].

EBL exploits the high charge-to-mass ratio of electrons in order to focus and to ensure deposition deep within the target material. In Figure 2.10 a schematic of the EBL

instrument is shown[109]. The electron source (gun) is located at the top of the column and contains several subparts. It consists of a polycrystalline tungsten wire filament with an emitting plate. Recent research has revealed that thermally assisted field emitters (TFE) operate better and produce a more controlled exposure/electron dose. The TFE (commonly ZrO or W) is heated to about 1800K in the presence of an extremely high electric field. This causes electrons to accelerate and be removed from the source material. The accelerated electrons pass through an aperture, and a blanker is used to stop the electron beam entering the optical column. The beam current is aligned and steered by using electrostatic lenses [109-111].
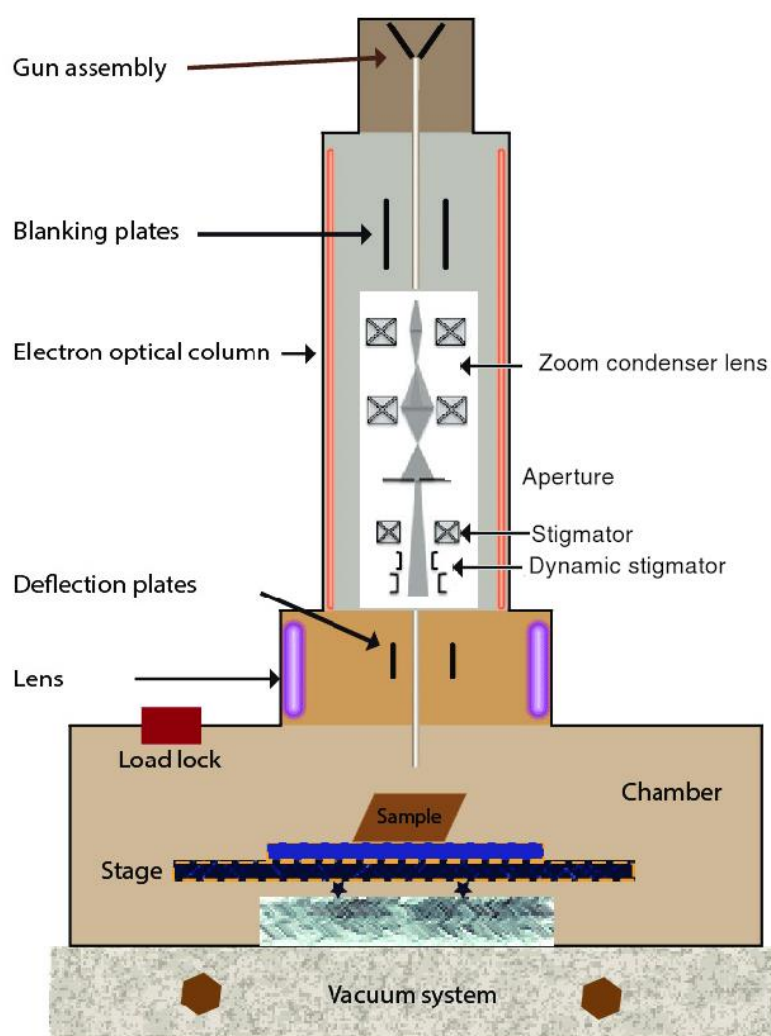
Figure   2.10

Schematic diagram of an EBL instrument. Adapted from Ref [107,108] [110, 111].

The optical column contains a magnetic mirror cylinder, consisting of: (i) a zoom condenser lens for controlling the beam size, (ii) a stigmator to produce equal linewidths for the beam, (iii) a dynamic focus stigmator to eliminate height variations during exposure. A deflector for high-speed scanning over a large field-of-view. A high precision digital-to-analogue converter to guide the electrons to achieve the desired sub and primary field size [109-111].

2.4.1   *Projection printing and direct writing*

The main advantages of high-voltage EBL over conventional photolithography techniques or wet chemical synthesis is its incredibly high resolution and increased functionality. EBL can precisely control both a patterns' dimensions and alignment and is very versatile for nanoimprinting of dense arrays. Moreover, EBL systems are designed for long-term stability and can be automated. over the past few decades, the "projection printing" and more recently " direct writing" methods have been used with EBL. The main difference between these two distinct methods is how the electron beam is projected on to the resist-coated substrate. In projection printing, a parallel electron beam passes through a mask and then exposes a substrate, however for indirect writing, a finely focused Gaussian electron beam directly exposes the substrate. Recently considerable effort has been made to improve the contrast of the direct writing technique and find new types of sensitive resist. In general, modern EBL consists of the following steps (see Figure 2.11):

I.   Deposition of a high resolution, sensitive resist, appropriate to the specific environment of a given process. Typically, two groups of resists are used based on their working principle. One of the most commonly used is PMMA, whilst another type of resist which is often used, is known as a chemically amplified resist. The first group of resists are categorised as a positive resist and can be either organic or inorganic. The second group are negative resists, such as SU-8 [103].

II.   Exposure of the resists. A focused electron beam is used in one of two ways to expose the resist: either one pixel at a time or in a vector or raster scan. Once exposed, the resist is developed to remove either the exposed or unexposed parts [112].

III.   Deposition of a thin layer of the desired metal. The metal material which forms the structure is deposited via a PVD process [112].

IV.   Removal, also known as a 'lift-off'. Removal is the final step in the EBL process and is accomplished by soaking the sample in an appropriate liquid solvent (e.g. PMMA removal or acetone) and removing the remaining resist along with the unwanted material [103].
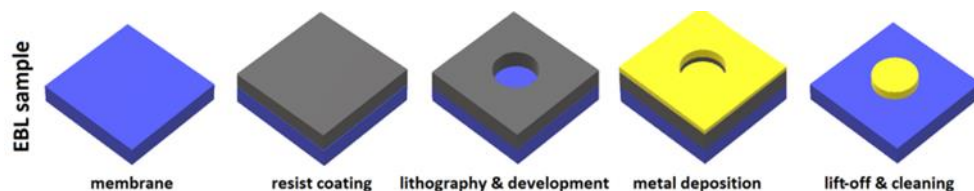
Figure 2.11 *Schematic overview of the individual fabrication steps using EBL. Adapted from Ref [112].*

2.5 Nanoimprint lithography

Nanoimprint lithography (NIL) is a low cost, nonconventional method of nanofabrication for high throughput patterning that has the ability to fabricate nanostructures with great precision. In contrast to conventional lithography that uses electrons or photons, NIL relies on direct mechanical contact for patterning. Consequently, NIL has a spatial resolution

beyond the optical diffraction or electron beam scattering limit. In 1995 Chou et al. published the first demonstration of thermal imprinting using a silicon dioxide compression mould (as the rigid material) and a thin layer of thermoplastic polymer. They were able to fabricate a border and trenches with 25nm features at a depth of 100nm in PMMA[101]. Soon after (in 1996) Hasim et al. demonstrated mould lithography in a two-step process by spin coating a thin layer of UV-curable monomer on the surface of the sample. These monomers were a photoinitiator, meaning that they absorb UV light and then start the photopolymerization process. In their approach the monomer was solidified through UV exposure, and after removing the mould, the unexposed parts of the monomer were etched [113].

In 2003, the Massachusetts Institute of Technology declared that NIL was one of the ten emerging technologies that would influence the world. NIL based mechanical moulding uses a pre-defined mould (typically made via EBL) and a suitable resist (with both high strength and durability) applied on top of the substrate. In general, the resists can be categorised into two groups: (i) thermal monomer and (ii) UV-photo initiator monomer. Typically the material used for moulds are metals such as nickel, or a dielectric such as silicon dioxide and silicon [114-116].

2.5.1   Fundamental principles of T-NIL and UV-NIL

In recent years various new attempts have been made to find economical solutions for nanoscale size patterning. NIL can be used for low-cost sub-10nm resolution production and can be replicated over large areas through repeated application of a template stamp. This section briefly introduces the essential elements in the imprint process, which have evolved recently. In general, NIL relies on two distinct imprint processes:

I.   Thermal NIL (T-NIL). In a standard T-NIL process, a single layer of polymer (typically PMMA) is spin-coated on a substrate which normally is very thin to ensure high fidelity pattern transfer. High mechanical pressures are required for pressing the mould onto the coated substrate. The topological patterns on the mould are then transferred to the resist polymer after heating it to the above the glass transition temperature. Note that the process parameters, pressure, temperature and time can vary depending on the resist material, resist thickness, and imprinted area. A possible consequence of this is that lower pressure can be compensated by increasing the fabrication time.

II.   UV-NIL. Whereas in T-NIL a solid resist needs to be heated up, in UV-NIL a liquid or droplets of resist (such as Nanonex, MII, AMO) are used at room temperature prior to imprinting. A transparent mould placed either at a constant distance from the surface of the resist or plunged into the dense droplet of resist. Patterning is done by curing resist with UV light owing to the low viscosity of the UV-curable monomer.

In both processes, after imprinting, the mould is separated from the substrate. Although both techniques involve entirely different mechanical steps and materials, still they deal with the same challenges during the process of imprinting such as; resist deformation by displacement or squeezing. Figure 2.11 shows the necessary steps used for patterning of a surface by thermal NIL (see Figure 2.12b and 2.12d) [115, 117].
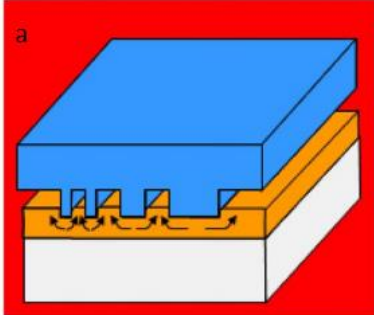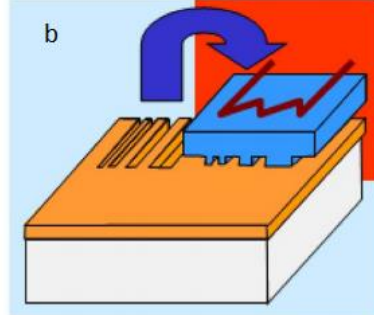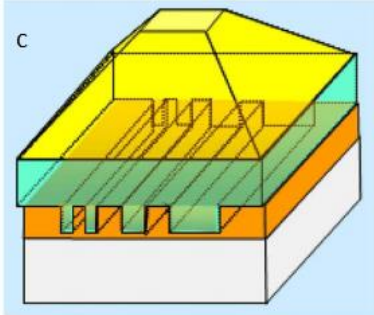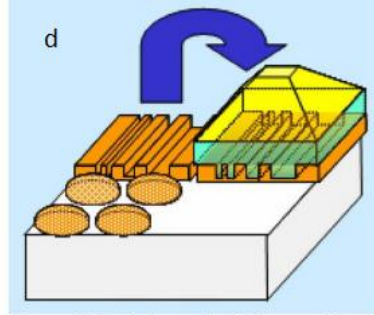
Process	Patterning scheme	Step & repeat (S&R) variant
Thermal nanoimprint lithography (NIL, T-NIL) – also called **Hot embossing lithography (HEL)**	a **Process:** Compression of thin thermoplastic film between hard stamp and substrate and molding by squeeze flow	b **Step&stamp imprint lithography (SSIL):** Similar to standard stepping lithography using small stamps (dies): only local heating over T_g
UV-nanoimprint lithography (UV-NIL) (a) Hard stamp lithography (b) Soft (stamp) lithography (SL)	c **Process:** Low pressure filling of liquid resin at room temperature by capillary action and hardening by UV-exposure through the stamp; coating by dispensing or spin coating of precursor	d **Stamp&flash imprint lithography (SFIL/O):** SSIL using a negative resist: coating and UV-exposure only locally **SFIL/R (reverse tone SFIL):** Patterning of planarization layer + overcoating enables imprint over intrinsic substrate topology

Figure 2.12 *The NIL Process. a) A thermoplastic resist and patterns coat the Si surface at 100 kV. The topological mould patterns (which were written by EBL) were transferred to the resist by compressing and heating the resist above the glass transition temperature, b) The step and stamp process to enlarge the imprinted area, c) Very thin layers of liquid UV-curable resist coated over the surface of a Si substrate. A transparent mould sinks into resist at room temperature and after hardening by UV light the resist separates from the mould, d) The pattern was repeated over different areas of the sample by a 'step and stamp' process [117].*

2.6 Experimental methods for device fabrication

The information given in this section provides an overview of the nanofabrication methods for the research presented in this thesis. As some details of sample preparation and fabrication protocol varied between different experiments, additional information is given in section 2.7 on the specific approaches used for each chapter of this thesis. The plasmonic devices used in this study were all fabricated at the Melbourne Centre for Nanofabrication (MCN) a Victorian Node of the Australian National Fabrication Facility (ANFF).

2.6.1   Preparation of substrates

Developments in FIB technology have enabled patterns with exceptional repeatability at some of the highest spatial resolutions to be produced. The plasmonic devices for this research were fabricated on top of a quartz substrate. The substrate (whose thickness was 0.5 – 1.0 mm) was cleaned in acetone and isopropanol via sonication for 5 minutes and rinsed using distilled water. Drying of the substrate was carried out with N_2 gas. Before deposition, the quartz wafer was dipped into piranha solution (a mixture of H_2O_2 and H_2SO_4 3:1) to remove any organic residues. Note, the piranha treatment was an important step in cleaning the substrate for the SAM experiments and in other experiments was also used to promote adhesion between the quartz surface and the deposited metal layer.

The nanofabrication of plasmonic devices consisted of the deposition of 3 nm of Ge, 25 nm of Cr and between 150 to 160 nm of Ag via e-beam evaporation (Nanochrome II, Intlvac) at a base pressure of approximately 5×10^{-7} Torr. The deposition rate (for all deposited metals) started at 0.3 Å/s for the first 2 minutes and then was slowly increased to 0.5 Å/s. Prior to deposition of the first Cr layer the substrate was plasma cleaned for 2 minutes (using an argon ion source inside the chamber). After the Cr, the Ge thin film was deposited which changed the grain-size and created a smoother surface, leading to improved adhesion of the top Ag layers.

Focused Ion Beam (FIB) lithography (Helios NanoLab 600 Dual Beam FIB-SEM, FEI) was used for nanofabrication of plasmonic devices with a beam current of $9.7\ pA$. The design of the plasmonic device which is based on cross-shaped apertures is shown in Figure 2.13a. The FIB system also incorporated a patterning package (Nanobuilder) to produce more precise and complex milling patterns. The input for the Nanobuilder software were 2D CAD designs produced using a software package called KLayout (see Figure 2.13b).
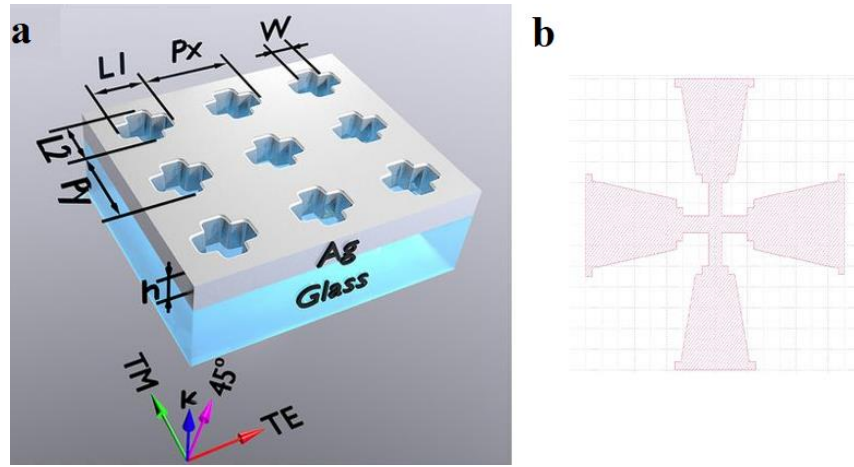
Figure 2.13 *a) Schematic of the plasmonic device structure for all experiments. The arm lengths and widths are denoted by* $L1, L2$ *and* w *respectively. Linearly polarized light (TM, 45°, and TE) shown from the substrate side. b) Schematic of one single cross aperture designed using the KLayout software.*

Patterns comprised asymmetric, cross-shaped nanoapertures, each cross has a long arm L_1 and short arm L_2 with a fixed arm width, w. The periodic subwavelength arrays (with square-lattice rows) placed with asymmetric distances across the x and y-axis that will be referred to as P_x and P_y, respectively. Each sample comprises one or more patterns with different pitches sizes (an average number of 40×40 patterns were perforated for each array). The sputtering yield is a function of the substrate material (Ag) and incident ion energy as well as the ion current. A variety of designs with varying aspect ratio between

arms, different periodicities in the *x* and *y* directions, or different arm width sizes were produced. A vital characteristic of the design was the ability to tune the spectral output by varying the device geometry and to be able to excite different resonance peaks by changing the incident polarisation.

During fabrication of the plasmonic devices using FIB Ga ions sputtered material from the thin Ag films to produce the desired structures. During fabrication a number of artifacts needed to be considered and, in particular, the redeposition of sputtered material (both Ga and Ag) onto the walls of the apertures. The effect of the redeposited material mixture resulted in a 'halo' around the aperture walls. The size of the halo is a function of the projected depth of the aperture [48]. In order to investigate this effect a number of different patterns were milled each having a different projected depth. Both a surface view of these arrays and cross-sections taken using SEM at a 52° tilt angle with a trench cut using FIB are shown in Figure 2.14. The values in the white boxes represent the actual milled thickness into the glass substrate.
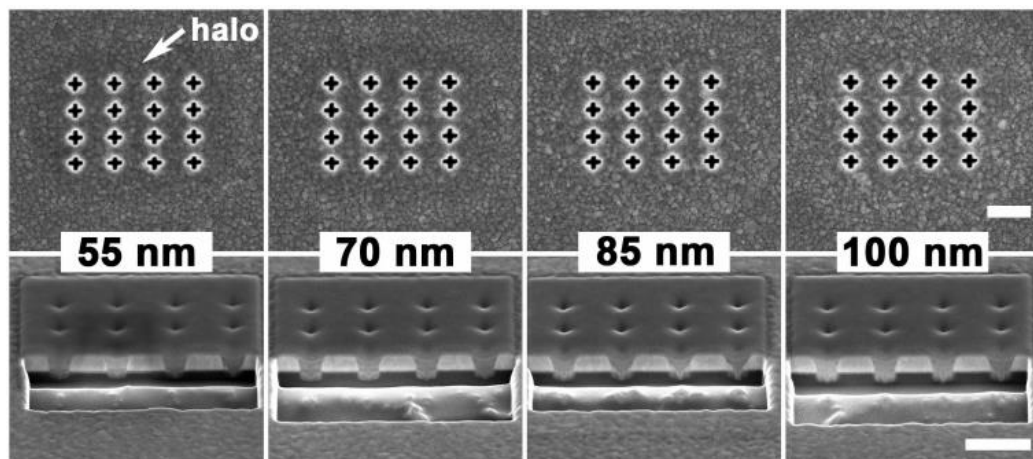
Figure 2.14 SEM images of apertures milled using a 55 nm, 70 nm, 85 nm and 100 nm projected depth. Bottom: The stage was tilted by $52°$ for the corresponding cross-sectional images. The scale bar on the image on the right is 500 nm.

2.7 Optical Characterisation

An inverted optical microscope was used to capture high resolution transmission brightfield images. The microscope was equipped with a bright-field condenser lens, a spectrometer and a cooled CCD camera. The transmitted light was coupled to the spectrometer to enable the acquisition of a complete spectrum in visible regime. The samples were illuminated by a plane-polarized white light source (halogen bulb). For this research, two different spectrometer systems were used, one based at the MCN and the other at LTU. Spectra presented in chapters 3 and 4 were collected at MCN whilst spectra presented in chapters 5 and 6 were acquired at LTU.

2.7.1   Micro spectrometry (MCN)

The MCN instrument is mounted on a Nikon Ti-U Microscope equipped with dark-field condenser lenses and illuminated sample by a polarized white light. A unique feature of the MCN spectrometer is its ability to measure a wide spectral range, 190nm to 1000 nm. The spectrometer was a Princeton Instruments Isoplane 320 High performance spectrometer with a diffraction grating of 150 g/mm and 1200 g/mm and a "Deep Cooled CCD" camera. It can be used in both transmission and reflection brightfield and transmission darkfield modes. Prior to analysis the spectra were normalised with respect to the white field (WF) illumination measured through the bare quartz substrate. The WF was collected at the same polarization angle and through the same sample surface area.

2.7.2   Micro spectrometry (LTU)

The LTU instrument is mounted on a Nikon ECLIPS Ti-E inverted microscope that was equipped with a perfect focus system (PFS) as well as a dark-field condenser lenses. The LTU spectrometer was an Ocean optics spectrometer coupled via an optical fibre to the transmission port. The spectrometer is anchored by high definition optics. The LTU instrument had great thermal stability and sufficient working distance to incorporate

microfluidics enabling measurement in solution. It also has the ability to measure a wide spectral range, 200 nm to 1100 nm. This instrument was ideal for studying in-situ dynamics such as was required for some of the chemical and molecular sensing work.

2.8 Summery of Experimental Method

The nanoscale cross-shaped aperture structure that was used for the plasmonic devices was similar for all experiments. However, the measurements and applications for these devices are quite different for the different chapters. In order to clarify these differences a brief summary of the relevant methods for each measurement is now given with further details provided in the relevant chapter.

2.8.1   Experimental method for chapter 3

For the nanoscale colour filter fabrication, prior to deposition, the quartz surface underwent a final cleaning process using a broad beam of Ar ion source for 5 minutes. The first deposited layer was Ge (note that no Cr layer was used for the devices presented in this chapter). The periodic arrays of cross-shaped apertures were fabricated with either a varying arm size or a varying periodicity. A number of different arrays with periodicity varying in the y-direction whilst keeping the aperture dimensions constant were fabricated. After these devices were fabricated and characterised the effect of a varying arm-to-width ratio was also investigated.

In order to evaluate the spatial resolution (quality) of the milled patterns the sputtering yield of the FIB was characterised by considering the grain size of the thin films based on images taken in cross-section. Finally, the optical performance of the devices was evaluated using optical microscopy. Both transmission spectra and optical images were collected under TE, 45^0 and TM incident polarisation. The TE-polarization of the incident light was aligned with the x-axis of the array and the TM-polarization with the y-axis.

2.8.2   Experimental method for chapter 4

Evaluation of the performance of Diamond-like carbon (DLC) as a protection layer against Ag oxidating aging was the main focus of chapter 4. During imaging using the FIB-SEM system, hydrocarbon molecules inside the chamber react with the surface of the plasmonic device as the electron beam is rastered across the surface. This leads to the local deposition of a conformational film of only a few nanometers in thickness. This deposited material is mainly composed of an amorphous layer of carbon in a sp2/sp3 hybridisation state, known as DLC. In chapter 4, the DLC protection layer deposited immediately after milling the plasmonic structures is investigated. Different exposure dosages (0.3, 1.4, 3, 24, 41, 265 $\mu C/cm^2$) were used when depositing the DLC.

2.8.3   Experimental method for chapter 5

In chapter 5 the behaviour of the complex refractive index is characterised in Ga-ion implanted TiO_2 thin film deposited by electron beam evaporation on top of a plasmonic device. Plasmonic devices were used to probe the ion-implanted thin films by depositing 50 nm of TiO_2 directly onto the devices. Following TiO_2 deposition, Ga ions at an acceleration voltage of 16 keV were implanted into the thin films at a range of different doses using a focused ion beam radius of 5 nm. During implantation, the beam was continuously raster scanned over the area of interest to achieve a homogenous dose within the implanted zone.

2.8.4   Experimental method for chapter 6

In this experiment, dual-pitched cross-shaped arrays fabricated in 150 nm thick Ag films were combined with microfluidic devices fabricated in polydimethyl siloxane (PDMS). The microfluidic devices had 200 μm wide inlet channels and a 5 mm^2 'sensing window' (see the conceptual design in Figure 2.15a). The microfluidic device was cast from a CNC fabricated aluminium mould. The PDMS was then attached to the Ag plasmonic device.

The samples of interest were optically characterised by collecting optical images and full spectra. The experimental setup and the illumination direction are shown in Figure 2.15.
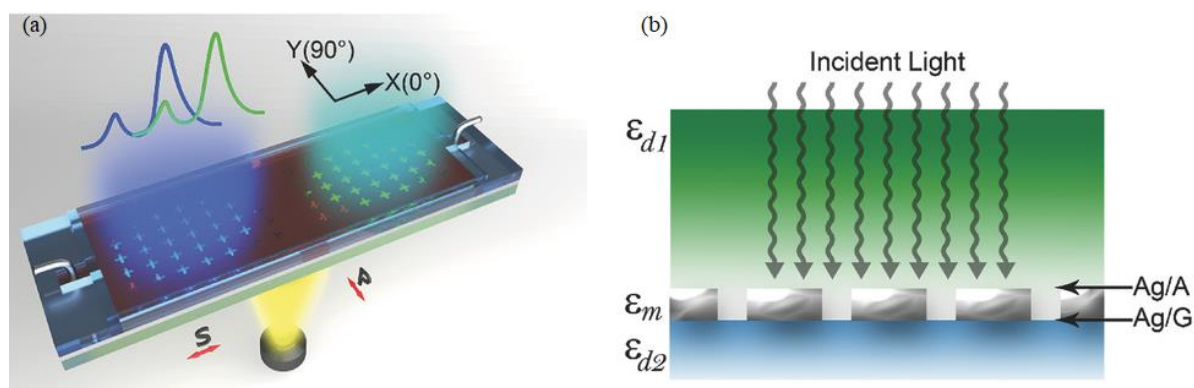
Figure 2.15 *Design for the plasmonic sensor integrated into a microfluidic device. a) Conceptual device design producing a bimodal transmission spectrum which is used for the detection of changes in the surrounding RI b) The experimental setup and illumination direction for the incident light.*

For the SAM experiments contamination was found to be a significant issue therefore it was important to protect the active surface of the sample from any dirt, dust or contamination. Samples were stored either in a desiccator or under pure ethanol. Also, for some of the experiments samples were encapsulated in a microfluidic system which kept the surface of the sensor free of contaminants. Prior to and between each measurement ethanol was used to remove any residual sample. After completion of a set of measurements the device was cleaned by ethanol followed by deionised water and finally nitrogen gas to dry the device's surface. In addition, for SAM formation, the devices were directly immersed in the dilute thiol solution for a given time (e.g. 24 hours for complete coverage). This was followed by washing with ethanol and deionised water before finally drying using N_2.

2.9 Summary

In this thesis, the performance of plasmonic-based structures is investigated for a range of colour filtering, sensing and imaging applications. This chapter has presented the basic background and theory required to understand the function and output of EOT based plasmonic devices utilising periodic arrays of apertures. In addition, some of the relevant experimental methods have been described and are expanded on in each individual chapter. In the following chapter we will see how the geometrical parameters of bimodal plasmonic devices play a critical role in determining their output and hence their performance.

2.10 References

1.   Wilts, B.D., N. IJbema, and D.G. Stavenga, *Pigmentary and photonic coloration mechanisms reveal taxonomic relationships of the Cattlehearts (Lepidoptera: Papilionidae: Parides).* BMC evolutionary biology, 2014. **14**(1): p. 160.

2.   Reider, G.A. *Light–Matter Interaction.* in *Photonics*. 2016. Springer.

3.   Benson, Z.A., C. Gong, and M.S. Leite, *Optical Response of Nanostructures: From Pure to Alloyed Metals*, in *Metal Nanostructures for Photonics*. 2019, Elsevier. p. 83-99.

4.   Lindquist, N.C., et al., *Engineering metallic nanostructures for plasmonics and nanophotonics.* Reports on Progress in Physics, 2012. **75**(3): p. 036501.

5.   Jensen, T.R., et al., *Nanosphere lithography: effect of the external dielectric medium on the surface plasmon resonance spectrum of a periodic array of silver nanoparticles.* The Journal of Physical Chemistry B, 1999. **103**(45): p. 9846-9853.

6.   Zhao, Q., et al., *Mie resonance-based dielectric metamaterials.* Materials today, 2009. **12**(12): p. 60-69.

7.   Brongersma, M.L., J.W. Hartman, and H.A. Atwater, *Electromagnetic energy transfer and switching in nanoparticle chain arrays below the diffraction limit.* Physical Review B, 2000. **62**(24): p. R16356.

8.   Oates, T., H. Wormeester, and H. Arwin, *Characterization of plasmonic effects in thin films and metamaterials using spectroscopic ellipsometry.* Progress in Surface Science, 2011. **86**(11-12): p. 328-376.

9.   Bobb, D., et al., *Engineering of low-loss metal for nanoplasmonic and metamaterials applications.* Applied Physics Letters, 2009. **95**(15): p. 151102.

10.   Weiner, J. and F. Nunes, *LIGHT-MATTER INTERACTION 2/E*. 2017: Oxford University Press.

11.   Bohm, D. and D. Pines, *A collective description of electron interactions. I. Magnetic interactions.* Physical Review, 1951. **82**(5): p. 625.

12.   Bohm, D. and D. Pines, *A collective description of electron interactions: III. Coulomb interactions in a degenerate electron gas.* Physical Review, 1953. **92**(3): p. 609.

13.   Fabrizio, M. and A.O. Gogolin, *Interacting one-dimensional electron gas with open boundaries.* Physical Review B, 1995. **51**(24): p. 17827.

14.   Quinn, J.J., *Range of excited electrons in metals.* Physical Review, 1962. **126**(4): p. 1453.

15.   Liebsch, A., *Surface-plasmon dispersion and size dependence of Mie resonance: silver versus simple metals.* Physical Review B, 1993. **48**(15): p. 11317.

16.   Liu, Z., et al., *Far-field optical hyperlens magnifying sub-diffraction-limited objects.* science, 2007. **315**(5819): p. 1686-1686.

17.   Shalaev, V.M., et al., *Negative index of refraction in optical metamaterials.* Optics letters, 2005. **30**(24): p. 3356-3358.

18.   Maier, S.A., *Plasmonics: fundamentals and applications*. 2007: Springer Science & Business Media.

19.   Kneipp, K. and H. Kneipp, *Non-resonant SERS Using the Hottest Hot Spots of Plasmonic Nanoaggregates.* Frontiers of Surface-Enhanced Raman Scattering: Single Nanoparticles and Single Cells, 2014: p. 19-35.

20.   Maier, S.A., *Plasmonics: The promise of highly integrated optical devices.* IEEE Journal of selected topics in Quantum Electronics, 2006. **12**(6): p. 1671-1677.

21.   Schmidt, S., et al., *Adiabatic nanofocusing on ultrasmooth single-crystalline gold tapers creates a 10-nm-sized light source with few-cycle time resolution.* ACS nano, 2012. **6**(7): p. 6040-6048.

22.   Müller, R., V. Malyarchuk, and C. Lienau, *Three-dimensional theory on light-induced near-field dynamics in a metal film with a periodic array of nanoholes.* Physical Review B, 2003. **68**(20): p. 205415.

23.   Wei, H. and H. Eilers, *From silver nanoparticles to thin films: Evolution of microstructure and electrical conduction on glass substrates.* Journal of Physics and Chemistry of Solids, 2009. **70**(2): p. 459-465.

24.   Townsend, E. and G.W. Bryant, *Plasmonic properties of metallic nanoparticles: The effects of size quantization.* Nano letters, 2011. **12**(1): p. 429-434.

25.   West, P.R., et al., *Searching for better plasmonic materials.* Laser & Photonics Reviews, 2010. **4**(6): p. 795-808.

26.   Otto, A., *Excitation of nonradiative surface plasma waves in silver by the method of frustrated total reflection.* Zeitschrift für Physik A Hadrons and nuclei, 1968. **216**(4): p. 398-410.

27.   Kretschmann, E. and H. Raether, *Radiative decay of non radiative surface plasmons excited by light.* Zeitschrift für Naturforschung A, 1968. **23**(12): p. 2135-2136.

28. Barnes, W.L., *Surface plasmon–polariton length scales: a route to sub-wavelength optics.* Journal of optics A: pure and applied optics, 2006. **8**(4): p. S87.

29. Kliewer, K. and R. Fuchs, *Collective electronic motion in a metallic slab.* Physical Review, 1967. **153**(2): p. 498.

30. Yeh, P., *Optical waves in layered media.* Vol. 95. 1988: Wiley Online Library.

31. Reider, G.A. *Wave Propagation in Matter.* in *Photonics.* 2016. Springer.

32. Ashcroft, N. and N. Mermin, *Solid state physics (brooks cole, 1976).* Cited on, 1993. **45**.

33. Etchegoin, P.G., E. Le Ru, and M. Meyer, *An analytic model for the optical properties of gold.* The Journal of chemical physics, 2006. **125**(16): p. 164705.

34. Rakić, A.D., et al., *Optical properties of metallic films for vertical-cavity optoelectronic devices.* Applied optics, 1998. **37**(22): p. 5271-5283.

35. Li, M., S.K. Cushing, and N. Wu, *Plasmon-enhanced optical sensors: a review.* Analyst, 2015. **140**(2): p. 386-406.

36. Ritchie, R.H., *Plasma losses by fast electrons in thin films.* Physical review, 1957. **106**(5): p. 874.

37. Zayats, A.V. and I.I. Smolyaninov, *Near-field photonics: surface plasmon polaritons and localized surface plasmons.* Journal of Optics A: Pure and Applied Optics, 2003. **5**(4): p. S16.

38. Wang, L., et al., *Active display and encoding by integrated plasmonic polarizer on light-emitting-diode.* Scientific reports, 2013. **3**: p. 2603.

39. Madou, M.J., *Fundamentals of microfabrication: the science of miniaturization.* 2002: CRC press.

40. Huber, R., et al., *How many-particle interactions develop after ultrafast excitation of an electron–hole plasma.* Nature, 2001. **414**(6861): p. 286.

41.   Baldelli, S., et al., *Surface enhanced sum frequency generation of carbon monoxide adsorbed on platinum nanoparticle arrays.* The Journal of Chemical Physics, 2000. **113**(13): p. 5432-5438.

42.   Langhammer, C., et al., *Localized surface plasmon resonances in aluminum nanodisks.* Nano letters, 2008. **8**(5): p. 1461-1471.

43.   Chan, G.H., et al., *Plasmonic properties of copper nanoparticles fabricated by nanosphere lithography.* Nano Letters, 2007. **7**(7): p. 1947-1952.

44.   Teng, Y.-Y. and E.A. Stern, *Plasma radiation from metal grating surfaces.* Physical Review Letters, 1967. **19**(9): p. 511.

45.   Blinov, L.M., et al., *Photoreactive organic thin films*. 2002: Elsevier.

46.   Jiang, Y., S. Pillai, and M.A. Green, *Re-evaluation of literature values of silver optical constants.* Optics express, 2015. **23**(3): p. 2133-2144.

47.   Barnes, W.L., A. Dereux, and T.W. Ebbesen, *Surface plasmon subwavelength optics.* nature, 2003. **424**(6950): p. 824.

48.   Ebbesen, T.W., et al., *Extraordinary optical transmission through sub-wavelength hole arrays.* Nature, 1998. **391**(6668): p. 667.

49.   Alkaisi, M., et al., *Sub-diffraction-limited patterning using evanescent near-field optical lithography.* Applied physics letters, 1999. **75**(22): p. 3560-3562.

50.   Luo, X. and T. Ishihara, *Sub-100-nm photolithography based on plasmon resonance.* Japanese journal of applied physics, 2004. **43**(6S): p. 4017.

51.   Lezec, H.J., et al., *Beaming light from a subwavelength aperture.* Science, 2002. **297**(5582): p. 820-822.

52.   Nyamekye, C.K., et al., *Experimental analysis of waveguide-coupled surface-plasmon-polariton cone properties.* Analytica chimica acta, 2019. **1048**: p. 123-131.

53.   Zhang, K. and O. Rabin, *Tailoring Localized Surface Plasmon Resonances in Metallic Nanoarcs for Surface Enhanced Infrared Absorption Spectroscopy.* Bulletin of the American Physical Society, 2019.

54.   Kawata, S., *Plasmonics: future outlook.* Japanese Journal of Applied Physics, 2012. **52**(1R): p. 010001.

55.   Genet, C. and T.W. Ebbesen, *Light in tiny holes*, in *Nanoscience And Technology: A Collection of Reviews from Nature Journals*. 2010, World Scientific. p. 205-212.

56.   Gordon, R. and A.G. Brolo, *Increased cut-off wavelength for a subwavelength hole in a real metal.* Optics Express, 2005. **13**(6): p. 1933-1938.

57.   Oldenburg, S., et al., *Nanoengineering of optical resonances.* Chemical Physics Letters, 1998. **288**(2-4): p. 243-247.

58.   Kim, J.T., et al., *Graphene-based plasmonic waveguide devices for electronic-photonic integrated circuit.* Optics & Laser Technology, 2018. **106**: p. 76-86.

59.   Catrysse, P.B. and S. Fan, *Nanopatterned metallic films for use as transparent conductive electrodes in optoelectronic devices.* Nano letters, 2010. **10**(8): p. 2944-2949.

60.   Pratsinis, S.E., *Aerosol-based technologies in nanoscale manufacturing: from functional materials to devices through core chemical engineering.* AIChE journal, 2010. **56**(12): p. 3028-3035.

61.   Tanriover, I. and H.V. Demir, *Broad-band polarization-insensitive all-dielectric metalens enabled by intentional off-resonance waveguiding at mid-wave infrared.* Applied Physics Letters, 2019. **114**(4): p. 043105.

62.   Martin-Moreno, L., et al., *Theory of extraordinary optical transmission through subwavelength hole arrays.* Physical review letters, 2001. **86**(6): p. 1114.

63.   Snyder, A.W. and J.D. Love, *Optical waveguide theory.* J. Opt. Soc. Am. A, 1986. **3**: p. 378.

64.   De Abajo, F.G. and J. Sáenz, *Electromagnetic surface modes in structured perfect-conductor surfaces.* Physical review letters, 2005. **95**(23): p. 233901.

65.   Liu, H. and P. Lalanne, *Microscopic theory of the extraordinary optical transmission.* Nature, 2008. **452**(7188): p. 728.

66.   Wood, R.W., *On a remarkable case of uneven distribution of light in a diffraction grating spectrum.* Proceedings of the Physical Society of London, 1902. **18**(1): p. 269.

67.   Hessel, A. and A. Oliner, *A new theory of Wood's anomalies on optical gratings.* Applied optics, 1965. **4**(10): p. 1275-1297.

68.   Rayleigh, L., *III. Note on the remarkable case of diffraction spectra described by Prof. Wood.* The London, Edinburgh, and Dublin Philosophical Magazine and Journal of Science, 1907. **14**(79): p. 60-65.

69.   Rudolph, D. and G. Schmahl, *Spektroscopische beugungsgitter hoher teilungsgenauigkeit erzeugt mit Hilfe von Laserlicht und photoresistschichten.* Optik, 1970. **30**(5): p. 475-87.

70.   Fano, U., *The theory of anomalous diffraction gratings and of quasi-stationary waves on metallic surfaces (Sommerfeld's waves).* JOSA, 1941. **31**(3): p. 213-222.

71.   Maystre, D., *Sur la diffraction d'une onde plane par un reseau metallique de conductivite finie.* Optics Communications, 1972. **6**(1): p. 50-54.

72.   Maystre, D., *Sur la diffraction d'une onde plane electromagnetique par un reseau metallique.* Optics Communications, 1973. **8**(3): p. 216-219.

73.   Maystre, D., *Theory of Wood's anomalies*, in *Plasmonics*. 2012, Springer. p. 39-83.

74.   Rayleigh, L., *On the dynamical theory of gratings.* Proceedings of the Royal Society of London. Series A, Containing Papers of a Mathematical and Physical Character, 1907. **79**(532): p. 399-416.

75.   Gordon, R., et al., *A new generation of sensors based on extraordinary optical transmission.* Accounts of chemical research, 2008. **41**(8): p. 1049-1057.

76.   Fano, U., *Effects of configuration interaction on intensities and phase shifts.* Physical Review, 1961. **124**(6): p. 1866.

77.   Zynio, S., et al., *Bimetallic layers increase sensitivity of affinity sensors based on surface plasmon resonance.* Sensors, 2002. **2**(2): p. 62-70.

78.   Ong, B.H., et al., *Optimised film thickness for maximum evanescent field enhancement of a bimetallic film surface plasmon resonance biosensor.* Sensors and Actuators B: Chemical, 2006. **114**(2): p. 1028-1034.

79.   Garcia-Vidal, F.J., et al., *Light passing through subwavelength apertures.* Reviews of Modern Physics, 2010. **82**(1): p. 729.

80.   Sigmund, P., *On the number of atoms displaced by implanted ions or energetic recoil atoms.* Applied Physics Letters, 1969. **14**(3): p. 114-117.

81.   Myers, S., *Ion-beam-induced migration and its effect on concentration profiles.* Nuclear Instruments and Methods, 1980. **168**(1-3): p. 265-274.

82.   Knez, M., K. Nielsch, and L. Niinistö, *Synthesis and surface engineering of complex nanostructures by atomic layer deposition.* Advanced Materials, 2007. **19**(21): p. 3425-3438.

83.   Hashim, A. and Q. Hadi, *Synthesis of novel (polymer blend-ceramics) nanocomposites: structural, optical and electrical properties for humidity sensors.* Journal of Inorganic and Organometallic Polymers and Materials, 2018. **28**(4): p. 1394-1401.

84.   Simpson, P. and S. Szpala, *Proportionality of vacancy concentration to ion implantation fluence.* Journal of applied physics, 2002. **92**(10): p. 5852-5855.

85.   Markel, V.A., *Introduction to the Maxwell Garnett approximation: tutorial.* JOSA A, 2016. **33**(7): p. 1244-1256.

86.   Sipe, J. and R.W. Boyd, *Nonlinear susceptibility of composite optical materials in the Maxwell Garnett model.* Physical Review A, 1992. **46**(3): p. 1614.

87.   Noy, A., et al., *Chemical force microscopy: exploiting chemically-modified tips to quantify adhesion, friction, and functional group distributions in molecular assemblies.* Journal of the American Chemical Society, 1995. **117**(30): p. 7943-7951.

88.   Liley, M., et al., *Direct observation of self-assembled monolayers, ion complexation, and protein conformation at the gold/water interface: an ftir spectroscopic approach.* Langmuir, 1997. **13**(16): p. 4190-4192.

89.   Cheng, S.S., D.A. Scherson, and C.N. Sukenik, *In situ attenuated total reflectance Fourier transform infrared spectroscopy study of carboxylate-bearing, siloxane-anchored, self-assembled monolayers: a study of carboxylate reactivity and acid-base properties.* Langmuir, 1995. **11**(4): p. 1190-1195.

90.   Leroux, Y., et al., *Conducting polymer/gold nanoparticle hybrid materials: a step toward electroactive plasmonic devices.* Electrochemistry communications, 2007. **9**(6): p. 1258-1262.

91.   Yao, J., et al., *Functional nanostructured plasmonic materials.* Advanced Materials, 2010. **22**(10): p. 1102-1110.

92.   Mallidi, S., et al., *Molecular specific optoacoustic imaging with plasmonic nanoparticles.* Optics Express, 2007. **15**(11): p. 6583-6588.

93.   Stewart, M.E., et al., *Quantitative multispectral biosensing and 1D imaging using quasi-3D plasmonic crystals.* Proceedings of the National Academy of Sciences, 2006. **103**(46): p. 17143-17148.

94.   Vericat, C., et al., *Thiol-capped gold: from planar to irregular surfaces.* Journal of Physics: Condensed Matter, 2008. **20**(18): p. 184004.

95.   Ulman, A., *Formation and structure of self-assembled monolayers.* Chemical reviews, 1996. **96**(4): p. 1533-1554.

96.   Scott, K.A., et al., *Coarse-grained MD simulations of membrane protein-bilayer self-assembly.* Structure, 2008. **16**(4): p. 621-630.

97.   Ghorai, P.K. and S.C. Glotzer, *Molecular dynamics simulation study of self-assembled monolayers of alkanethiol surfactants on spherical gold nanoparticles.* The Journal of Physical Chemistry C, 2007. **111**(43): p. 15857-15862.

98.   Roper, D.K., *Determining surface plasmon resonance response factors for deposition onto three-dimensional surfaces.* Chemical engineering science, 2007. **62**(7): p. 1988-1996.

99.   Jung, L.S., et al., *Quantitative interpretation of the response of surface plasmon resonance sensors to adsorbed films.* Langmuir, 1998. **14**(19): p. 5636-5648.

100.   Andersson, O., et al., *Imaging SPR for detection of local electrochemical processes on patterned surfaces.* Sensors and Actuators B: Chemical, 2008. **134**(2): p. 545-550.

101.   Ziegler, J.F. and J.P. Biersack, *The stopping and range of ions in matter*, in *Treatise on heavy-ion science*. 1985, Springer. p. 93-129.

102.   Reyntjens, S. and R. Puers, *A review of focused ion beam applications in microsystem technology.* Journal of micromechanics and microengineering, 2001. **11**(4): p. 287.

103.   Ventra, M., S. Evoy, and J.R. Heflin, *Introduction to nanoscale science and technology*. 2006: Springer Science & Business Media.

104.   Giannuzzi, L.A., *Introduction to focused ion beams: instrumentation, theory, techniques and practice*. 2004: Springer Science & Business Media.

105.   Tennant, D. and A. Bleier, *Electron beam lithography of nanostructures*. Handbook of Nanofabrication (Elsevier, Amsterdam 2010) Chap, 2010. **4**: p. 121-148.

106.   Broers, A., A. Hoole, and J. Ryan, *Electron beam lithography—Resolution limits*. Microelectronic Engineering, 1996. **32**(1-4): p. 131-142.

107.   Wiederrecht, G., *Handbook of nanofabrication*. 2010: Academic Press.

108.   Newman, T., K.E. Williams, and R. Pease, *High resolution patterning system with a single bore objective lens.* Journal of Vacuum Science & Technology B: Microelectronics Processing and Phenomena, 1987. **5**(1): p. 88-91.

109.   Vieu, C., et al., *Electron beam lithography: resolution limits and applications.* Applied surface science, 2000. **164**(1-4): p. 111-117.

110.   Biswas, S., *Optimization of nanowire photodiode devices for neuronal cell survival*. 2013, Lund University.

111.   Sze, S.M., *Semiconductor devices: physics and technology*. 2008: John wiley & sons.

112.   Horák, M., et al., *Comparative study of plasmonic antennas fabricated by electron beam and focused ion beam lithography.* Scientific reports, 2018. **8**(1): p. 9640.

113.   Haisma, J., et al., *Mold-assisted nanolithography: A process for reliable pattern replication.* Journal of Vacuum Science & Technology B: Microelectronics and Nanometer Structures Processing, Measurement, and Phenomena, 1996. **14**(6): p. 4124-4128.

114.   Schift, H., *Nanoimprint lithography: An old story in modern times? A review.* Journal of Vacuum Science & Technology B: Microelectronics and Nanometer Structures Processing, Measurement, and Phenomena, 2008. **26**(2): p. 458-480.

115.   Cochrane, A., et al., *Multiphase model for nanoimprint lithography.* International Journal of Multiphase Flow, 2018. **104**: p. 9-19.

116.   Guo, T., *Fiber grating-assisted surface plasmon resonance for biochemical and electrochemical sensing.* Journal of Lightwave Technology, 2017. **35**(16): p. 3323-3333.

117.   Varghese, L.T., et al., *Resistless nanoimprinting in metal for plasmonic nanostructures.* Small, 2013. **9**(22): p. 3778-3783.

CHAPTER 3

CONTINUOUSLY TUNABLE PLASMONIC COLOUR FILTERS

3   INTRODUCTION

This chapter describes the systematic investigation into the influence of plasmonic device geometry and the results of experiments conducted using plasmonic colour filters. The first half of the chapter explains how a continuous colour palette can be produced using bimodal plasmonic devices based on periodic arrays of cross-shaped nanoapertures. It explores the relative influence of a range of geometrical parameters. It also examines the role of asymmetry in the device design and the use of linearly polarized light to obtain multi-functionality from a single plasmonic device. The second half of the chapter discusses simulation work carried out using the COMSOL Multiphysics 5.1 software to confirm our understanding of the influence of geometrical parameters on the optical characteristics of plasmonic colour filters.

3.1   Influence of geometry on optical output

Subwavelength cross-shaped apertures are the ideal candidate for demonstrating the potential polarization sensitivity of plasmonic colour filters owing to their inherent asymmetry. Cross-shaped apertures can respond differently to multiple different polarisation states and consequently can be used as the basis for plasmonic colour filters which produce a continuous colour palette as their optical output. Using high-accuracy nanofabrication techniques, it is now possible to study the influence of the aperture shape on the functional characteristics of these structures. The result is devices which have an increased dynamic range and sensitivity for a range of applications including colour filtering as well as chemical and molecular sensing.

Figure 3.1 shows a schematic of the cross-shaped aperture array used in this study and shows the axes which define the polarisation direction of the light which impinges from the glass side. TE and TM represent two orthogonal modes associated with the polarized light aligned along the x and y axes of the array, respectively. Each cross is characterised by three key dimensions: L_x and L_y, which indicate the length of the arms along the x and y directions, respectively, and w which represents the width of the arms of the crosses. The figure also shows the array periodicity in the x and y directions (Px and Py) and the Ag film thickness h respectively.
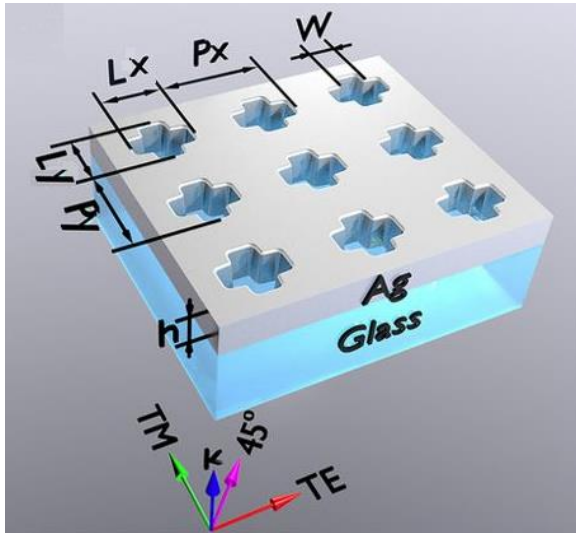
Figure 3.1 Schematic illustration of the cross-shaped aperture arrays used in the present study. The cross apertures have dimensions of L_x and L_y and w as shown. The periodicity of the pattern along the x and y axis is given by Px and Py, respectively; h is the Ag film thickness.

Figure 3.2 presents SEM images taken of a typical cross-shaped aperture array used for this study. Figure 3.2a displays the periodic array pattern after FIB milling, b shows a zoomed-in sub-region of the cross-shaped aperture array, and c is an image of a cross-section taken through two of the apertures.
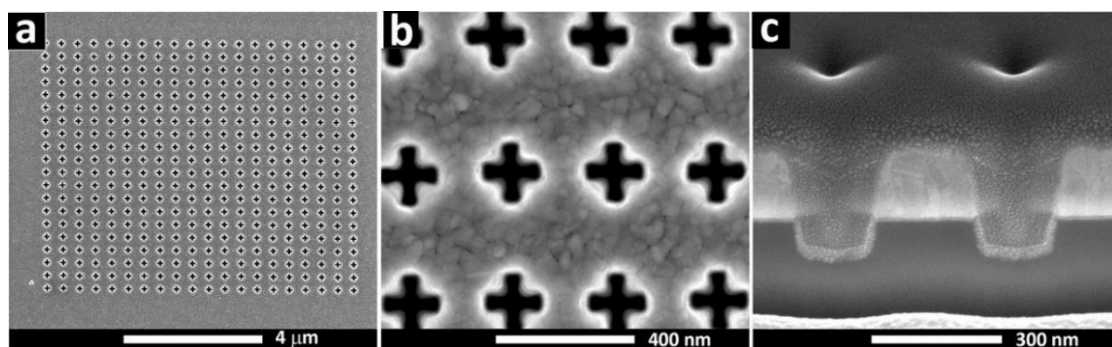
Figure 3.2 *SEM images of a representative array of cross-shaped nanoapertures. a) SEM image of one of the patterns, b) zoomed-in region of the pattern, and c) the FIB cross-section through some of the apertures, showing the underlying glass substrate, Ag film and Pt/C which was deposited during the milling process.*

The high-resolution SEM images reveal a high fidelity in the cross-shaped apertures whilst the cross-cut shows the bevelled profile of the aperture walls (~83°), which is inherent to the FIB milling process. A thin film of Pt/C was deposited on top of the patterns in order to obtain a clean-cut section after milling.

3.1.1   Effect of nanoaperture shape

In the first part of the study the length of the arms of the cross-shaped apertures was varied whilst all other parameters were kept constant. Tables 3.1 summarises parameters used to investigate the effect of the arm length on the optical output. For this experiment all patterns were fabricated in a 150 nm thick Ag films and the arm length of the cross-shaped apertures was only varied in the y direction.

Constant parameter values (nm)	Variable parameter, L_y (nm)
P_x= 300 L_x= 160 P_y= 450 $w = 40$	160
	140
	120
	80
	40

Table 3.1 *The geometrical parameters used to investigate the effect of nanoaperture shape. The film thickness as well as, P_x and L_x, were kept constant for all patterns.*

Figure 3.3 shows the transmission spectra collected under both TM and TE polarization modes for the structures defined in Table 3.1.
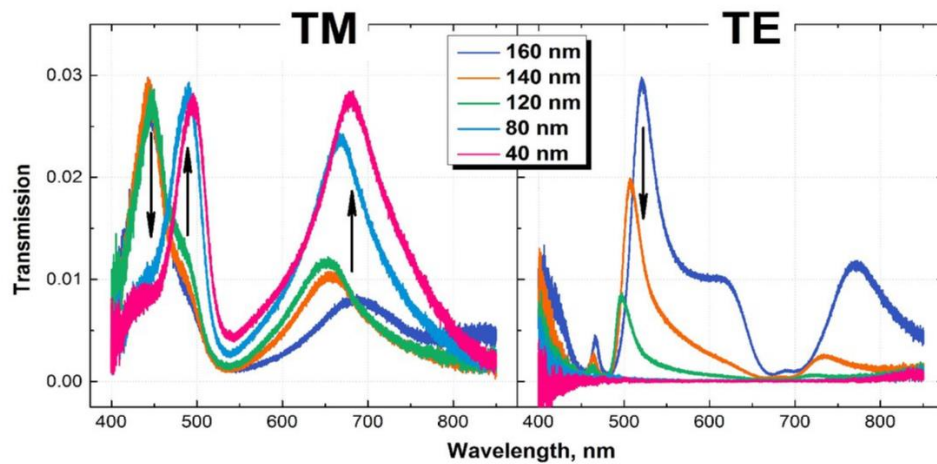
Figure 3.3 *Example transmission spectra under both TM and TE polarization modes for structures with variable arm length in the y direction.*

We observe that as L_y decreases, the resonant peak heights corresponding to the TE polarization gradually decrease. This decrease is accompanied by a reduction in the overall amount of transmitted light. The position of the peaks, however, remains largely unchanged as a result of the reduction in arm length. The situation is quite different for the TM

98

polarization, where the resonant peak at shorter wavelengths (~420 nm) drastically decreases when L_y reaches 80 nm, and the one at longer wavelengths (~670 nm) drastically increases respectively. The origin of these effects will be discussed in detail in section 3.2 and 3.3.3. Based on these results, we conclude that altering the cross-arm length leads to variation in the overall transmitted intensity but only relatively minor changes in the resonant peak position.

3.1.2   Effect of array periodicity

In the next set of experiments, ten patterns with varying periodicity P_y were fabricated using constant values for P_x (280 nm) as well as constant values for the cross-arm width and length (40nm and 160nm respectively). The geometrical parameters for the second set of experiments is summarised in Table 3.2.

Constant parameter values (nm)	Variable Parameter
	P_y (nm)
	300
$P_x= 280$	320
$L_x= 160$	340
$L_y= 160$	360
$w= 40$	380
	400
	420
	440
	480

Table 3.2 *The geometrical parameters used to investigate the effect of array periodicity. All parameters were kept constant whilst the periodicity Py was varied.*

Figure 3.4a shows the optical images that were collected for all samples illuminated with

TE, 45°, and TM linearly polarized light.
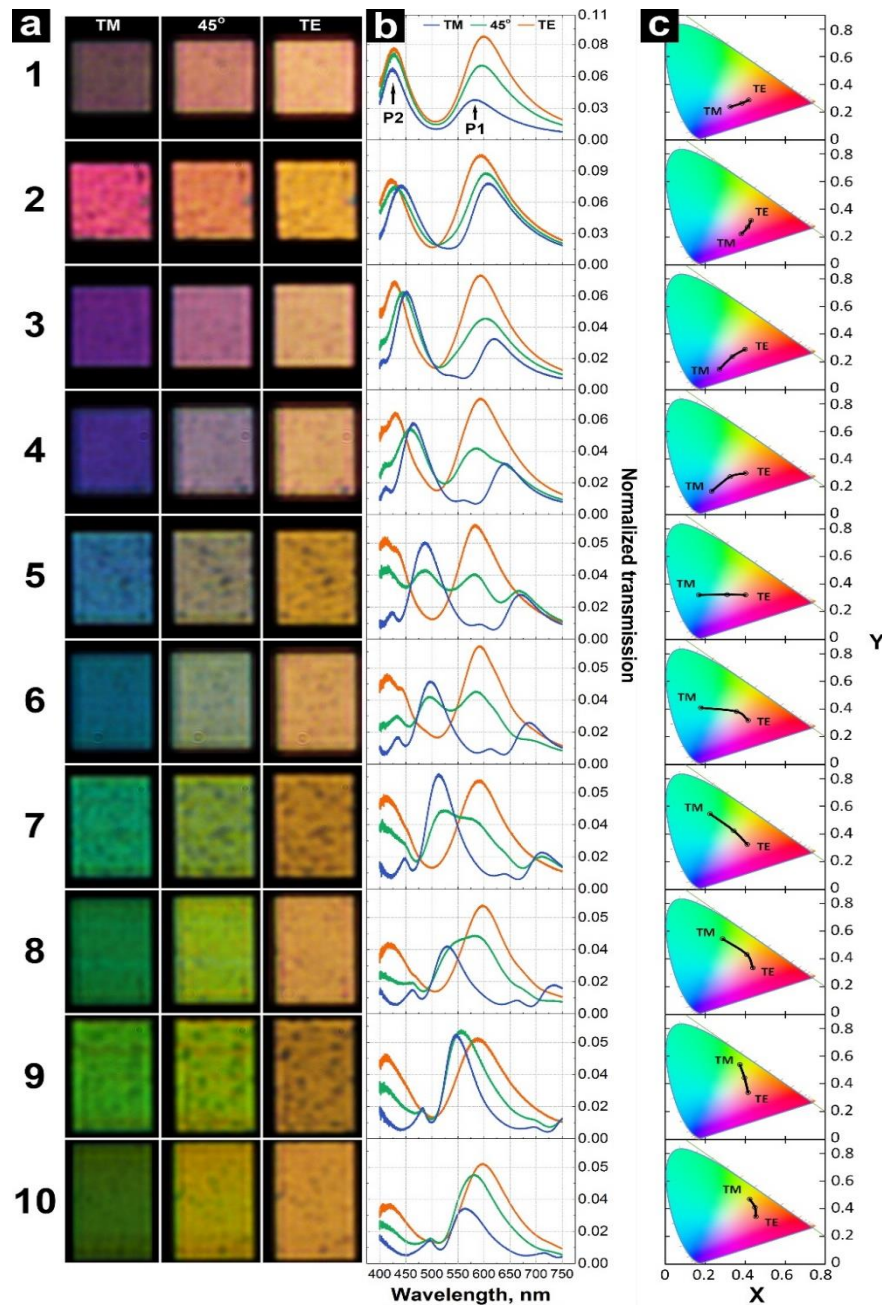
Figure 3.4 *a) Optical images of transmitted light for ten different periodicities using TM,*

45° and TE polarized light. b) Associated normalized transmission spectra showing the

position of the main peaks P1 and P2. c) Mapping of b) to points on the CIE 1931 xy

chromaticity diagram, demonstrating active polarization-dependent color tuning.

We observe that as the periodicity P_y increases a continuous range of colours is detected using TM polarized incident illumination. The situation is quite different for the TE polarisation mode where a single colour dominates the spectrum. Optical images using 45° polarized light display a mix of the colours observed for the TM and TE polarisations over the entire range of periodicities. As the polarisation direction was continuously varied between the TM and TE modes a gradual colour change was observed. The transmission spectra shown in Figure 3.5 b shows the resonant peaks associated with the TM, 45°, and TE polarisations. The features of these peaks will be described in detail in section 3.2. Overall, as the periodicity in the *y* direction increases, the resonant peak position in the transmission spectra of the TM polarized light undergoes a red shift, whilst it shows almost no changes when using TE polarized light. The transmission spectra at 45° incident polarisation meanwhile reveals a convolution of the TE and TM modes. In summary, it is possible to achieve a rainbow-like colour palette by gradually varying the distance between the cross-shaped apertures in just one direction (*y*) whilst keeping it constant in another direction (*x*). Figure 3.5a shows the SEM image taken from an array of cross-shaped apertures with gradually varying the periodicity in *y* direction. The corresponding optical images in Figure 3.5b demonstrate that in principle any colour can be achieved by choosing an appropriate periodicity. Furthermore, the colour palette can be readily adjusted by varying the incident polarization of the light. To determine the effect in terms of the perceived colours, linear colorimetric transformations were applied to each spectrum enabling the data to be displayed on a CIE 1931 *xy* chromaticity diagram (Figure 3.4c). All possible color palette combinations, resulting from the interpolation of the output at TE and TM polarisations observed for a particular pattern are plotted on the CIE 1931 *xy* chromaticity diagrams.
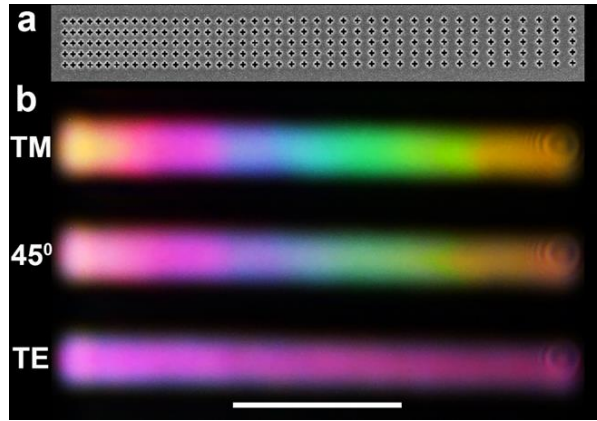
Figure 3.5 *a) SEM image of an array of cross-shaped apertures with a gradually varying periodicity in the y direction. b) Corresponding optical images of transmitted light for this structure using TM, 45°, and TE polarized light. The scale bar is 5 μm.*

Following the same fabrication principles, complex geometries can be readily achieved whilst retaining the same polarization sensitivity (Figure 3.6).
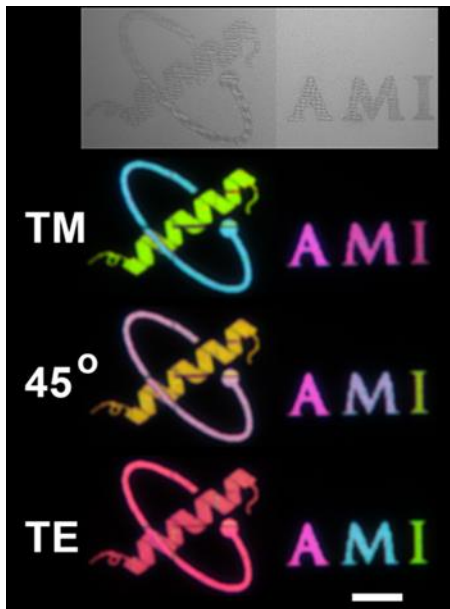
Figure 3.6 *SEM image (top) of complex structure design fabricated using apertures with varying periodicities. (bottom) Corresponding optical images of transmitted light using TM, 45° and TE polarized light. The scale bar is 15 μm.*

We next wanted to explore the smallest possible pattern that could be fabricated whilst retaining the full functionality and polarisation sensitivity of the larger devices (Figure 3.7).
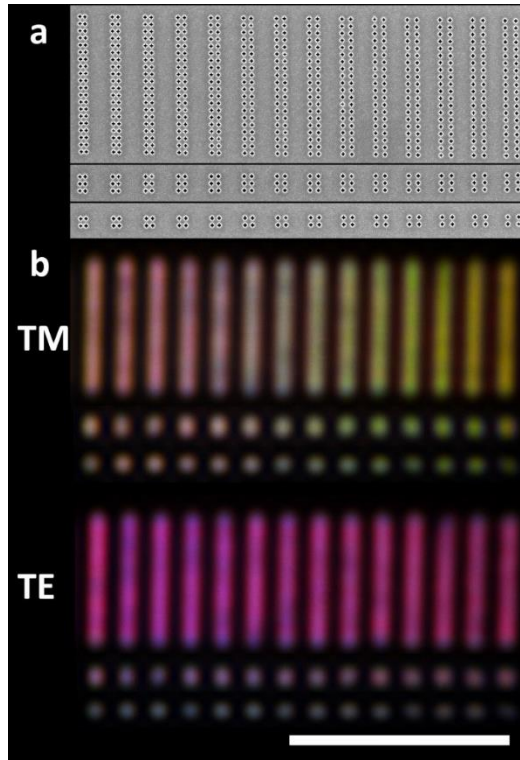
Figure 3.7 a) SEM images of 2 × 20, 2 × 3 and 2 × 2 nanoaperture arrays with gradually increasing periodicity in the x-direction. b) Corresponding optical transmission images under TM and TE polarization. The scale bar is 10 μm.

Figure 3.7 shows same trends in the colour output of the device as the periodicity is varied in one direction whilst keeping it constant in the other direction. Remarkably, even the smallest pixel fabricated from just 2×2 apertures retain this property, demonstrating the fact that the smallest achievable colour 'pixel' is in the range of 300 nm.

This experiment was followed by an investigation of the combined effect of both the aperture shape and pattern periodicity on the optical output of the plasmonic colour filters. In this case the geometrical parameters in the x direction (P_x and L_x) were kept constant for all patterns. The dimensions of the patterns in y direction were then varied as summarised in Table 3.3.

Constant parameter values (nm)	Variable Parameter (nm)	
	P_y and L_y	w
	$P_y = 260$ $L_y = 100$	50
		40
		30
$h = 150$ $P_x = 320$ $L_x = 160$	$P_y = 280$ $L_y = 120$	50
		40
		30
	$P_y = 300$ $L_y = 140$	50
		40
		30

Table 3.3 The geometrical parameters (both constant and variable) used for the plasmonic devices. The film thickness and geometrical parameters in x-directions, P_x and L_x, were kept constant for all patterns. Three different sets of geometrical values in the y-direction was considered $(L_y: 100 \ P_y: 260), (L_y: 120 \ P_y: 280)$ and $(L_y: 140 \ P_y: 300)$ with corresponding cross-arm widths of $w: 50, 40,$ and $30 \ nm$.

Figure 3.8 displays the optical images and the corresponding spectra for all patterns taken in transmission mode under three different polarizations (TE, 45° and TM). The optical images in Figure 3.8 are organised such that each row corresponds to patterns with constant P_x, P_y, L_x and L_y and variable arm width w. A direct correlation of the observed colours and transmitted spectra is observed when the incident light polarization changes from TE to TM. This is a direct result of the array asymmetry. Furthermore, by decreasing the cross-

arm width, the transmitted intensity gradually decreases (resulting in dimmer colours), with no detectable shift in the resonant peak position. On another hand, by decreasing the cross-arm length (L_y) and subsequently the periodicity (P_y) by the same amount in order to keep the distance between the cross-arm in y direction constant, we observe a colour change from pink to yellow. These changes are reflected in the transmitted spectra for all polarizations, where the resonant peaks are blue-shifted as the L_y/P_y ratio changes from 140 nm/300 nm to 100 nm/260 nm.
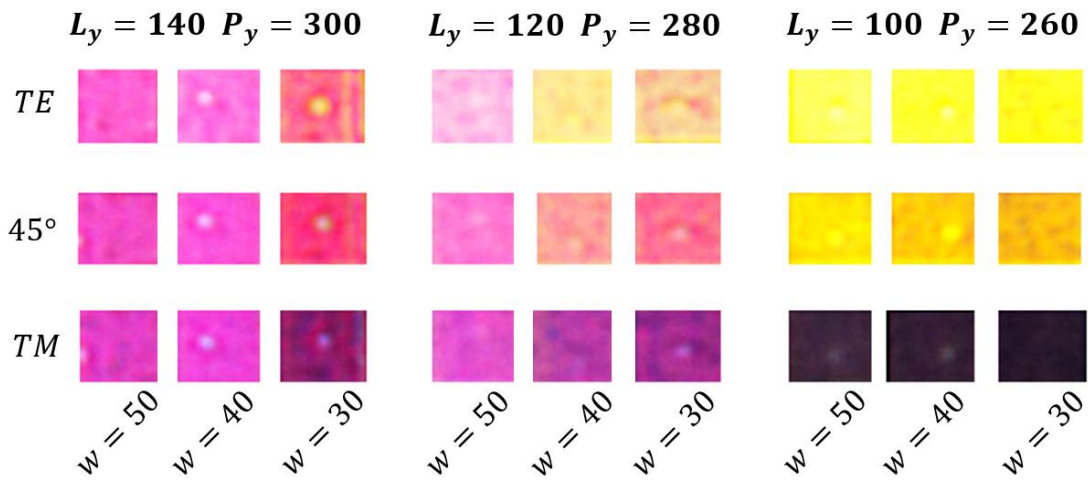
Figure 3.8 Bright-field optical images of the transmitted light observed through nine different patterns for 3 different polarization modes. The geometry of the patterns is summarised in Table 3.3.

From these set of results, it was clear that the reduction in the cross-arm width was primarily responsible for the decrease in the transmitted intensity and had negligible influence on the position of the resonant peaks. Also, it was noted that the variation in the cross-arm length and distance between the individual apertures results in a blue-shift of the resonant peak positions. However, from the experimental results it is difficult to determine which parameter is dominant in determining the output of the devices. In the next set of

experiments, we keep all the geometrical parameters constant whilst varying the film thickness.

3.1.3 Influence of the film thickness

Based on the above studies, we observed that the aperture periodicity plays a crucial role in determining the observed colour. In this section the effect of a varying film thickness was explored with experiments performed on films of 100, 150 and 200 nm Ag thickness. The overall effect of film thickness on transmitted intensity is illustrated in Figure 3.9.
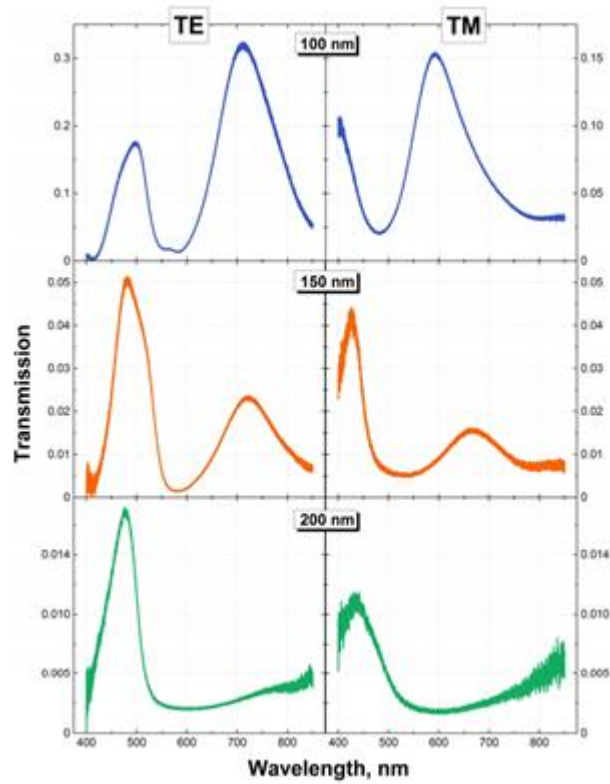
Figure 3.9 *Normalized transmission spectra using TE (left) and TM (right) incident polarisation. The $P_x = 250\ nm$, $P_y = 310\ nm$ and $w = 40\ nm$ is identical for both arms. The Ag film thickness was 100 nm, 150 nm, and 200 nm.*

These initial studies looking at the effect of a varying film thickness identified two main trends: the overall intensity decreased as the film thickness increased and the intensity of

the resonant peak appearing at longer wavelengths decreased relative to the intensity of the

resonant peak occurring at shorter wavelengths. The reasoning behind these observations

is discussed in section 3.2. Table 3.4 summarises used parameters for the film thickness

study.

Constant Parameters, nm	Variable Parameters, h, P_y (nm)		
	h		P_y
	100	150	250
$P_x = 250$			280
$L_x = 160$			310
$L_y = 160$			350
$w = 40$			390
			440
			500

Table 3.4 The geometrical parameters (both constant and variable values) used to fabricate

the plasmonic devices on two substrates with different Ag thickness. The periodicity in y

direction (P_y) was increased.

Figure 3.10 and 3.11 show the optical images and the corresponding transmitted spectra for devices fabricated on 100 nm and 150 nm Ag films, respectively. The periodicity P_x the cross-arm width was kept constant at 250 nm and 40 nm, respectively.
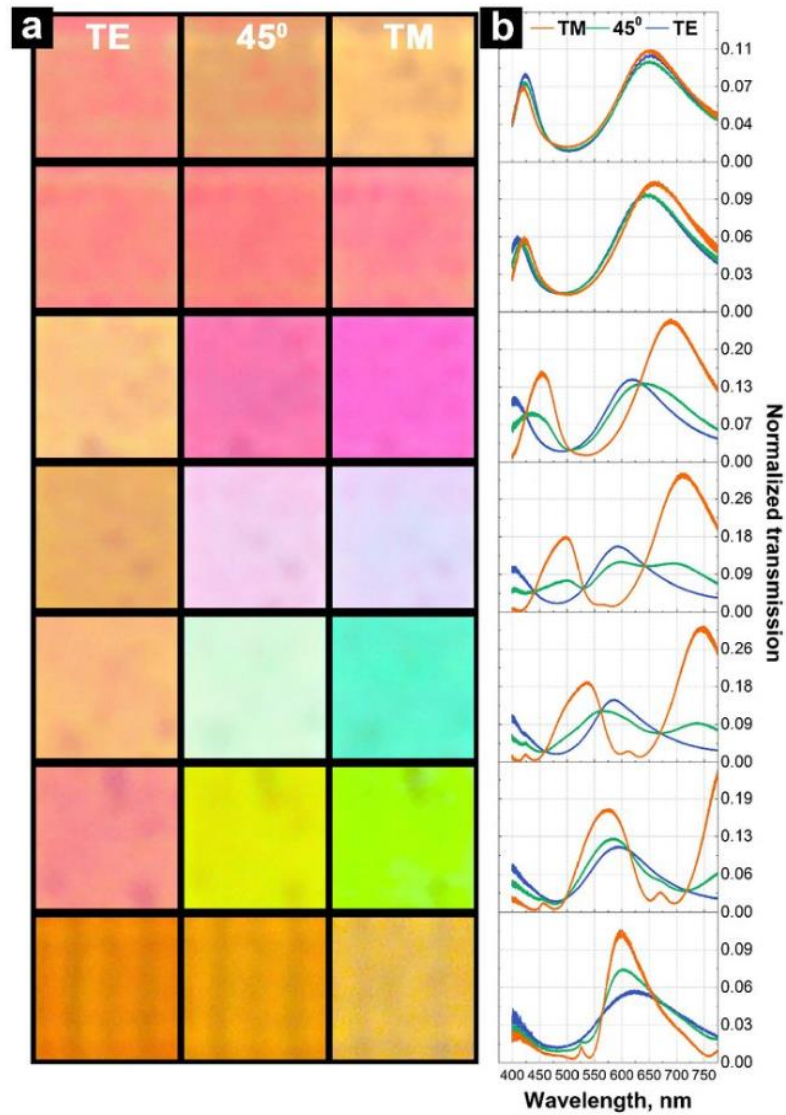
Figure 3.10 *a) The optical images in transmission mode under TE, 45^0 and TM polarized light. b) Corresponding transmission spectra. The crosses were fabricated with variable periodicity in y direction: 250, 280, 310, 350, 390, 440 and 500. The thickness of the Ag film is 100 nm.*
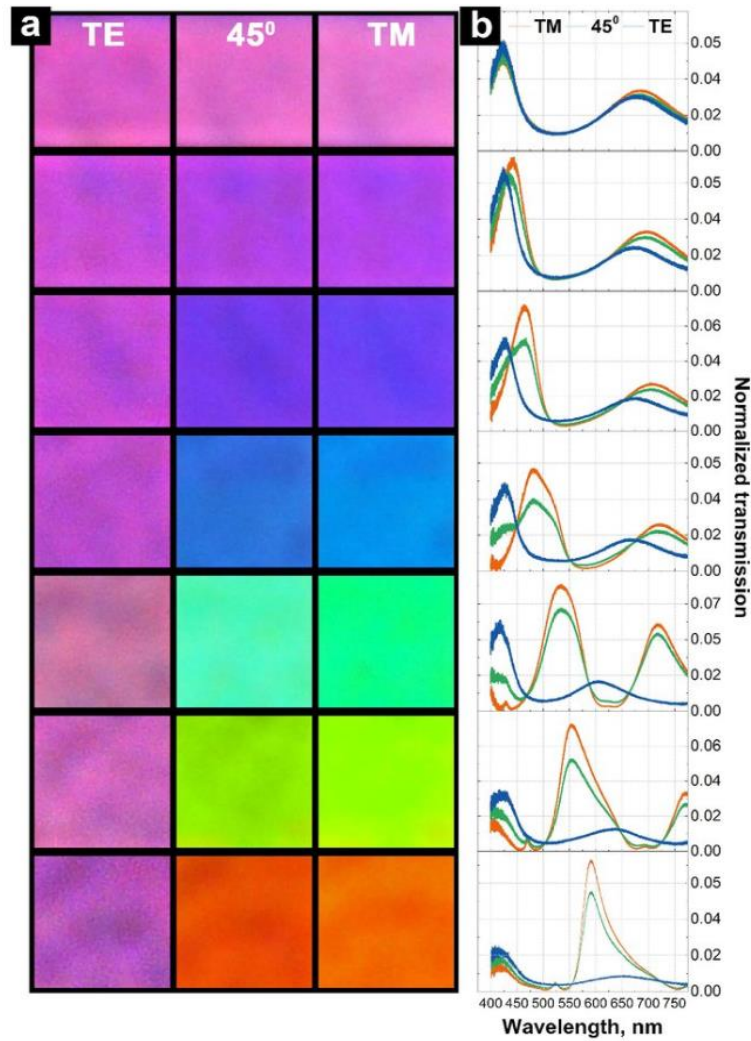
Figure 3.11 a) Optical transmission images under TE, 45^0 and TM polarized light b) Corresponding transmission spectra. Crosses were fabricated with variable periodicity in the y-direction: 250, 280, 310, 350, 390, 440 and 500 nm. The Ag film thickness is 150 nm.

For both Ag substrates, as the periodicity in *Y* direction was increased, the position of the resonance peaks underwent a redshift. However, in contrast to the transmitted colours produced by the structures on 100 nm Ag, the structures on 150 nm Ag produced more vibrant colour palette. This effect is readily observable in the transmitted spectrum, were the influence of the second peak at longer wavelength gradually diminishes, giving rise to more defined colours.

3.2 Theory of periodic array apertures in metallic films

In general, all spectra reveal two sets of dominant resonant peaks in each polarization mode. The position of these distinguishable peaks can be determined by using the dispersion relation for the EOT-based devices [1]:

$$\lambda_{SPP} \cong \frac{P}{\sqrt{i^2+j^2}} \sqrt{\frac{\varepsilon(\omega)_m \varepsilon_d}{\varepsilon(\omega)_m + \varepsilon_d}} \tag{3.1}$$

This equation is valid for a rectangular array of apertures, where P is the lattice constant (periodicity of the apertures) in x or y directions respectively, ε_d is the dielectric constant on either side of the metal film, ε_m is the real part of the dielectric constant of the metal film, and i and j are integers representing diffraction orders. This relation explains the presence of two set of resonant peaks in the transmission spectrum, associated with the Ag/glass and Ag/air interfaces. It also shows how the position of the peaks depends on the array periodicity observed in the experimental results. Besides the resonant peaks associated with these two interfaces, smaller satellite peaks observed in transmission spectra could be explained by the presence of Wood-Rayleigh anomalies (RA), which are characteristic to periodic metallic gratings, described by the relation [2, 3]:

$$\lambda_{WA} \cong \frac{P}{\sqrt{i^2+j^2}} \sqrt{\varepsilon_d} \tag{3.2}$$

Any changes in the periodicity of the same system (no changes of dielectric constant) produces spectral shifts according to the expressions:

$$\Delta\lambda_{SPP} \cong \frac{\Delta P}{\sqrt{i^2+j^2}} \sqrt{\frac{\varepsilon(\omega)_m \varepsilon_d}{\varepsilon(\omega)_m + \varepsilon_d}} \tag{3.3}$$

$$\Delta\lambda_{WA} \cong \frac{\Delta P}{\sqrt{i^2+j^2}} \sqrt{\varepsilon_d} \tag{3.4}$$

In order to compare the experimental results with the results using these relations, a system composed of a Ag 150 nm film on glass with the geometrical parameters used in the experimental section was employed. All SPP modes in the transmitted spectral range studied here along with RA modes associated with Ag/glass and Ag/air interfaces were empirically calculated for different array periodicities and compared to the experimental data (Figure 3.12).
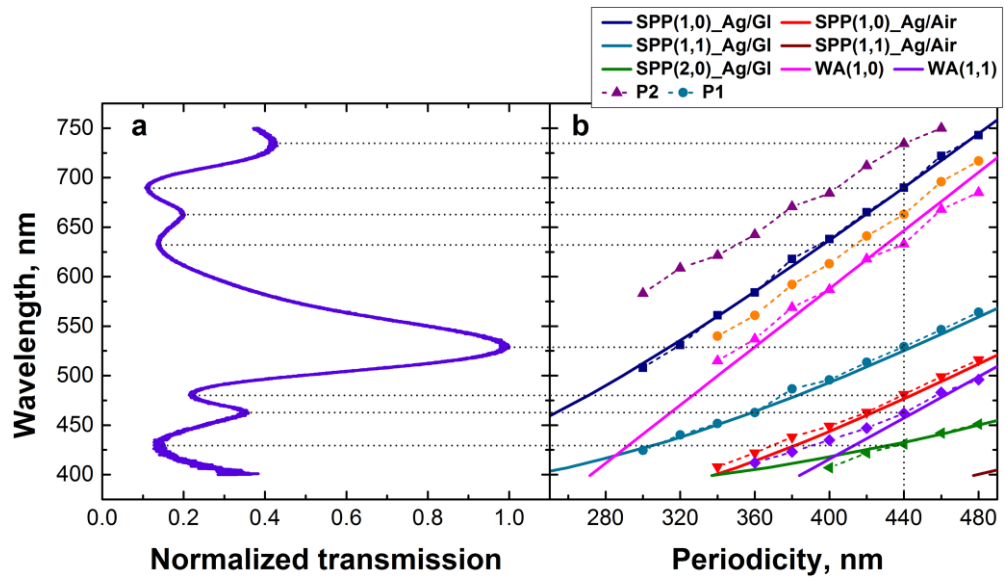
Figure 3.12 *a) Normalized transmission spectra for the 440 nm periodicity array (sample S8) showing the correlation of the peaks' origin of different modes. b) Experimental (doted lines) and calculated (full lines) SPP and RA modes.*

From Figure 3.12 we note that the expected positions of peaks in the experimental data are redshifted compared to the calculated values. This red-shift was experimentally observed at ~4% redshifted wavelengths in other works as well and was analytically calculated using the Kramers–Kronig relation [4]. The discrepancies found between the experimental observations and the analytical interpretations could be explained by the fact that the dispersion relations do not take into account the role of the aperture geometry, film thickness and scattering losses within the aperture.

According to Chen *et.al.*, the slits making up the cross-shaped apertures can be viewed as a bound charge oscillator, having a shape resonance (or cut-off frequency) of [5]:

$$\lambda_{res} = L\sqrt{2(\varepsilon_d + 1)} \qquad (3.5)$$

where L is the cross-arm length. However, Stalzer *et al.* viewed the cross-shaped aperture as a waveguide and calculated the associated TE and TM modes using the two-dimensional scalar Helmholtz equation. Based on his model, the relation of the TE_{10} mode of the cut-off frequency (which is the mode that is positioned in the spectral range studied here) is written as [6]:

$$\lambda_{res} = \frac{L^2}{0.7(L-W)}\sqrt{\varepsilon_d} \qquad (3.6)$$

where W is the arm width. According to Chen et al. and Stalzer et al. relations, the calculated cut-off frequency for the cross-shaped apertures studied here is expected to be in the range of 411 and 463 nm respectively. This localized SP mode (LSP) could be responsible for the discrepancies observed in the blue region of the spectra. However, it cannot explain alone the origin of the discrepancies in the red region of the spectrum.

Other works have noticed the role of the film thickness on transmission light through perforated metallic films. The reason of the strong dependence of optical transmission on film thickness is the existence of SPPs on both sides of the film, due to the presence of two interfaces. If the film thickness is close to or less than twice the 'skin depth' length in metal (which for Ag is $\sim$29 nm at 400 nm wavelength), these SPP modes couple together, having a direct effect on the peaks positions. For symmetric structures with a similar dielectric medium on both sides, the SPP modes on both interfaces have same resonance frequencies leading to an increased transmission intensity. An implication of this is the possibility that coupling between SPPs occurs at a single set of peaks [7].

From the transmission spectrum of the experimental data for structures explored in this study, another interesting aspect was noted. The peaks situated at longer wavelengths have a distinct Fano-type [8] asymmetric line-shape compared to the peaks situated at shorter wavelengths. The origin of this effect might be explained by the fact that the LSPs of aperture couple with the electromagnetic field of the SPPs and RAs. These LSP modes possess a narrow energy dispersion situated in the short wavelength region, described by the following relation [9]:

$$E \cong \frac{E_0}{\pi} \frac{L}{t} \cos\left(k_{SPP} t + \frac{\pi}{2}\right) \tag{3.7}$$

where $k_{SPP} = 2\pi/\lambda_{SPP}$, E_0 is the electrical field of the incident plane wave and t is the metal film thickness.

Another effect associated with the metal film thickness is the existence of aperture waveguide modes that act as 'Fabry-Perot' resonators. In this case, the maximum intensity of transmission light depends strongly on the LSP mode and aperture geometry. This effect is substantial when the film thickness is bigger than half of the SPP resonance wavelength, e.g. $> \frac{\lambda_{spp}}{2}$. We note that the coupling of SPP and LSP modes, the resonant nature of apertures, the film thickness and the losses associated with the film internal structure, and the fabrication processes could explain the discrepancies found between the experimental data and analytical interpretation.

3.3 FEM Simulations and Numerical implementation

3.3.1 Introduction

In parallel to the experimental data, COMSOL Multiphysics 5.1 software, which is based on the first principles of EM propagation, was employed to better understand the distribution of EM fields within the periodic structure. The approach used in designing the model geometry for the FEM simulations was similar to that used in experimental

fabrication: all aperture imperfections associated with the fabrication process, such as edge roundness, bevelling and over-milling were taken into account in order to find a better agreement with the experimental data. Figure 3.13 shows the model sketch used in the simulations.
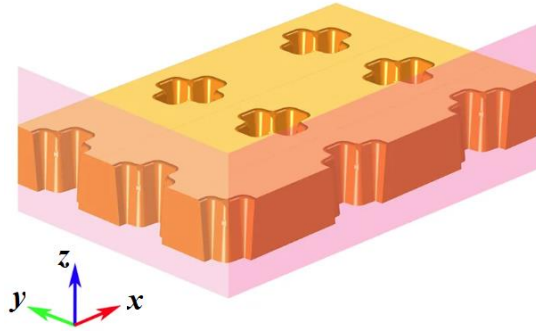
Figure 3.13 The schematics showing the cross-shaped apertures fabricated in optically opaque Ag films, the surface plane (xy plane) and cross-sectional planes (yz and zx).

3.3.2 Simulation of output as a function of periodicity

A summary of the resulted spectra along with the experimental results under TE and TM polarizations are sown in Figure 3.14. The intensity of transmitted spectra is displayed for (a) simulated and (b) experimental data as a function of periodicity for TM and TE modes and their corresponded transmission spectra. The intensity was normalized to the incident light. The value of the main peaks P_x and P_y is shown in both, the map diagram and the plot.
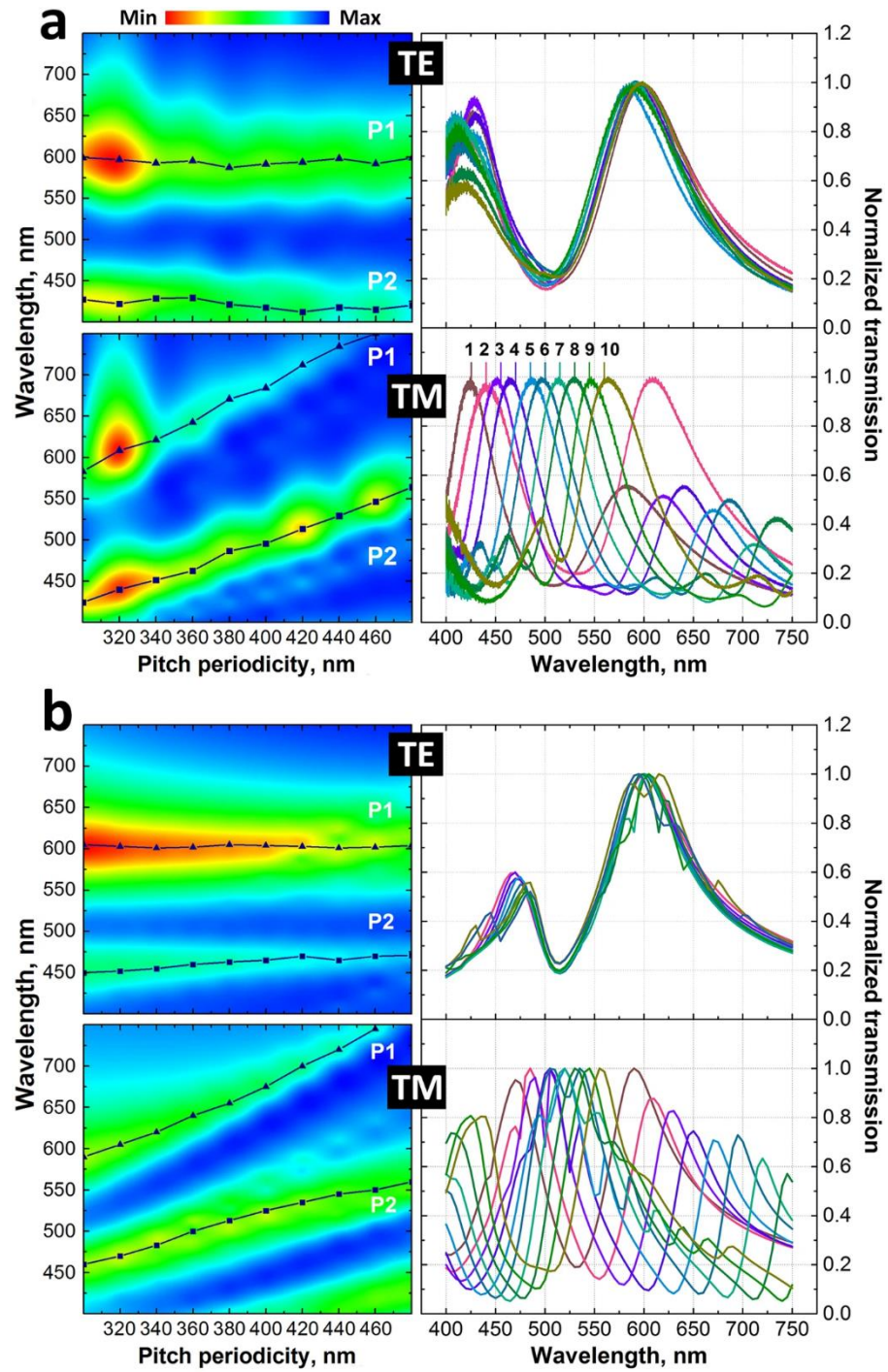
Plots 1-10 correspond to ten different periodicities in the Y direction ranging from 300 to 480 nm in 20 nm step.

Figure 3.14 *Intensity maps of the transmitted light as a function of periodicity for TM and TE polarized light and their associated normalized transmission spectra for experimental a) and calculated b) data. P1 and P2 plots indicate the position of main peaks.*

The results from the numerical calculations show the same trend of spectral red-shift, as the array periodicity in one direction is increased for TM polarization, while no shift is observed at TE polarization where the periodicity was kept constant.

3.3.3 Near-field electric field distribution

The calculated transmission spectra for the TM polarisation mode and the EM distribution through one of the samples with P_y=440 nm is displayed in Figure 3.15. The observed featured in the spectra are denoted by local maxima and minima points.
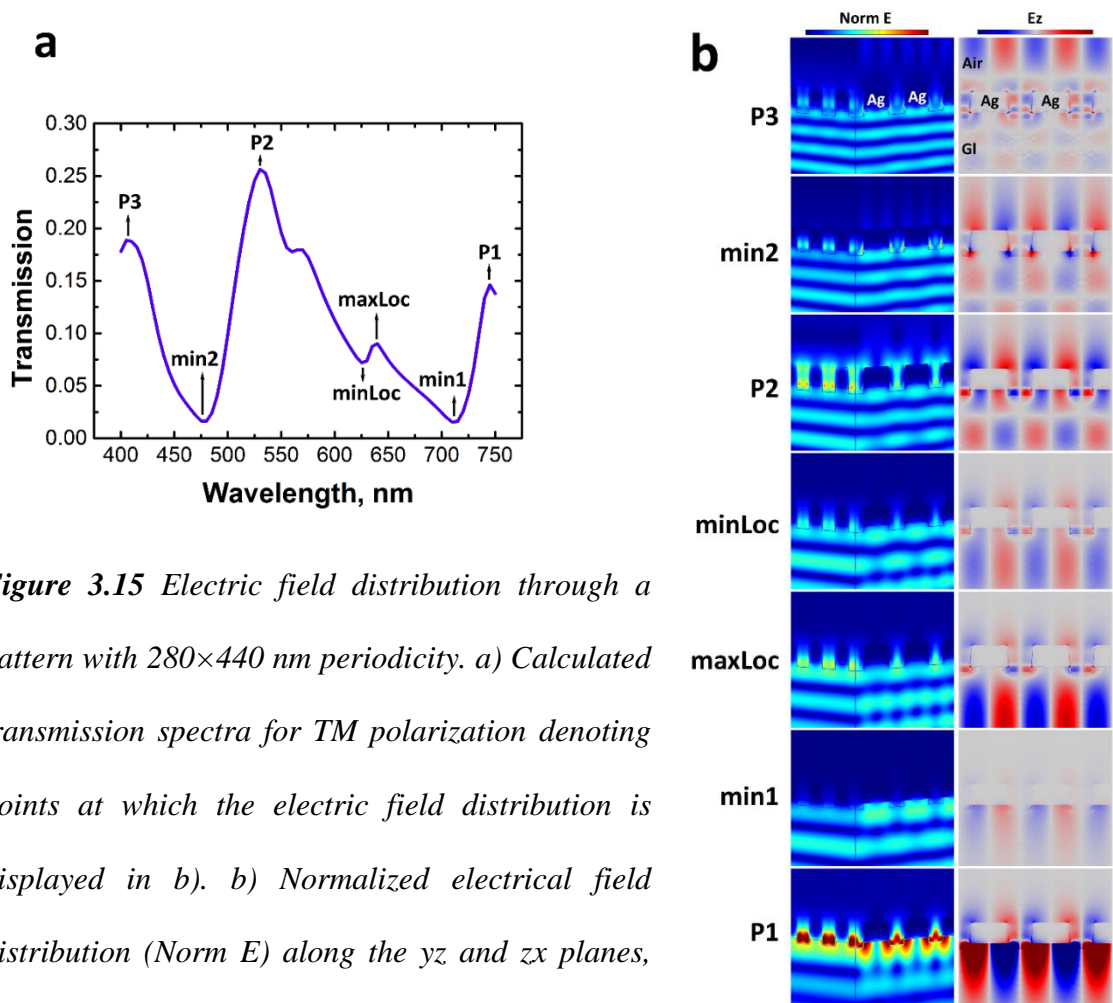
Figure 3.15 Electric field distribution through a pattern with 280×440 nm periodicity. a) Calculated transmission spectra for TM polarization denoting points at which the electric field distribution is displayed in b). b) Normalized electrical field distribution (Norm E) along the yz and zx planes, and amplitude of the field component normal to the metal surface (Ez) in zx plane.

The position of the features displayed in Figure 3.15 were chosen to correspond to the electric field distribution near the SPP, RA and LSP modes, which were experimentally observed in the transmitted spectra. From Figure 3.15b, it is noted that the electrical fields associated with peaks *P1*, *P2* and *P3* have different mechanisms of far-field propagation. The peak *P3* (~407 nm) depicts a strong localized mode within the aperture, readily noticeable in the amplitude of the field component normal to the metal surface (E_z plot), which might be attributed to the LSP. Based on the theoretical calculations, the position of this localized mode is expected to occur at ~411 nm. As all main SPP and RA modes occur at longer wavelengths, they do not expect to interfere with this LSP mode leading to a maximum in the spectra. This effect is also demonstrated by the absence of localized electrical fields at the Ag/glass or Ag/air interfaces in the 'Norm E' intensity maps for the *P3* peak. In contrast, the peak *P2* at ~525 nm shows a strong localized distribution of EM field at the Ag/air interface with visible far-field propagation demonstrating the SPP nature of the Ag/air (1,0) mode. Similarly, the peak *P1* peak, with a strong electric field distribution at the aperture rims with an enhanced propagation, could be attributed to the SPP (1,0) Ag/glass mode. The RA (1,0) Ag/glass mode at 645 nm appears as a localized maximum (*min/max*) in the spectra.

3.4 Conclusions

The use of periodic arrays of cross-shaped apertures as polarization-controlled colour filtering devices was demonstrated and the geometrical parameters responsible for the control of optical output were discussed. It was concluded that the array periodicity plays a crucial role in the setting the colour palette value, where the increased periodicity led to a red-shift of the transmitted spectrum. The colour palette could be further varied by employing asymmetrical periodic arrays of apertures. A continuous change of colour gamut could be readily achieved by gradually changing the angle of linearly polarized light with

respect to the array cell. By increasing the metal film thickness, more vibrant colour palette is observed, as a result of suppressed plasmonic modes associated with Ag/glass interface. Furthermore, it was proven that using such structures, any desirable configuration could be used for much more complex devices with the same polarization sensitivity. Also, it was shown that pixels as small as 2×2 apertures retain these properties, making possible fabrication of ultra-small nano-pixels (~300 nm).

It was demonstrated that the dispersion relations used to describe the peak position of SPP, and RA modes alone are not enough to explain the transmission output observed in the experimental details. Effects of the aperture geometry, film thickness as well as waveguide modes and the fabrication errors have to be considered in this scenario. FEM numerical simulations were carried out to better understand the nature of the individual peaks observed in the transmitted spectrum, by exploring the EM field distribution at the peak's positions.

3.5   References

1.   Ghaemi, H., et al., *Surface plasmons enhance optical transmission through subwavelength holes.* Physical review B, 1998. **58**(11): p. 6779.

2.   Chen, C.-Y., et al., *Extraordinary transmission through a silver film perforated with cross shaped hole arrays in a square lattice.* Applied Physics Letters, 2007. **91**(6): p. 063108.

3.   Lin, L. and A. Roberts, *Light transmission through nanostructured metallic films: coupling between surface waves and localized resonances.* Optics express, 2011. **19**(3): p. 2626-2633.

4.   Genet, C., M.P. van Exter, and J. Woerdman, *Fano-type interpretation of red shifts and red tails in hole array transmission spectra.* Optics Communications, 2003. **225**(4-6): p. 331-336.

5.   Choe, J.-H., et al., *Slot antenna as a bound charge oscillator.* Optics Express, 2012. **20**(6): p. 6521-6526.

6.   Stalzer, H., M. Greenman, and F. Willwerth, *Modes of crossed rectangular waveguide.* IEEE Transactions on Antennas and Propagation, 1976. **24**(2): p. 220-223.

7.   Barnes, W.L., *Surface plasmon–polariton length scales: a route to sub-wavelength optics.* Journal of optics A: pure and applied optics, 2006. **8**(4): p. S87.

8.   Fano, U., *Effects of configuration interaction on intensities and phase shifts.* Physical Review, 1961. **124**(6): p. 1866.

9.   Pacifici, D., et al., *Quantitative determination of optical transmission through subwavelength slit arrays in Ag films: Role of surface wave interference and local coupling between adjacent slits.* Physical Review B, 2008. **77**(11): p. 115411.

CHAPTER 4

DIAMOND LIKE CARBON PASSIVATION OF PLASMONIC DEVICES

4   INTRODUCTION

As discussed in Chapter 3, Ag-based plasmonic devices possess a high FoM due to their comparatively narrow resonant peaks and high sensitivity to local changes in the dielectric constant of the surrounding medium. However, it is well-known that Ag suffers from the oxidative ageing, making Ag-based plasmonic devices unsuitable for many real-world applications including chemical and molecular sensing. Figure 4.1 shows how Ag degradation impacts the optical efficiency of plasmonic colour filters. Due to the deleterious effects of oxidative aging it is thus critically important that the plasmonic Ag thin film is adequately protected from the surrounding environment.
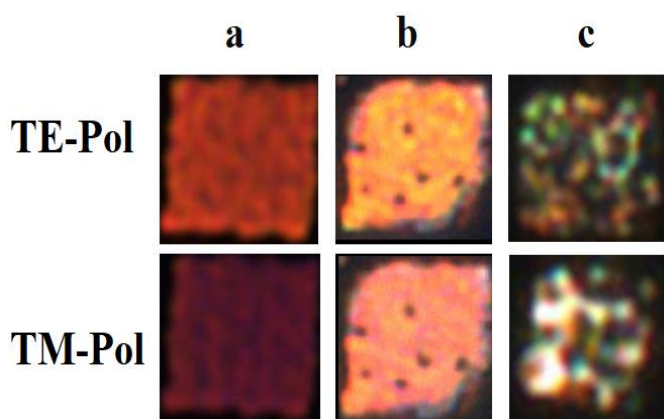
Figure 4.1 *Optical images of an unprotected Ag plasmonic device a) before, b) after 1 month and c) after 3 months submerged in water. Both TE and TM polarization modes are shown.*

Various published solutions have been proposed that aim to protect the active metallic film in plasmonic devices. The most common solution involves depositing an inert protective thin overlayer in order to create a physical barrier between the metal and the surrounding environment. Published demonstrations using thin layers of Au, SiO_2, graphene, and

PMMA have shown varying degrees of success[1-3]. Other more conventional approaches involve simply storing the films under vacuum up until the point of application, however, this does not offer a solution to the problem of using the films as chemical or environmental sensors. Some of these approaches, however, such as capping Ag films with thin layers of Au dramatically alter the plasmon resonance structure and hence have the potential to degrade the corresponding FoM.
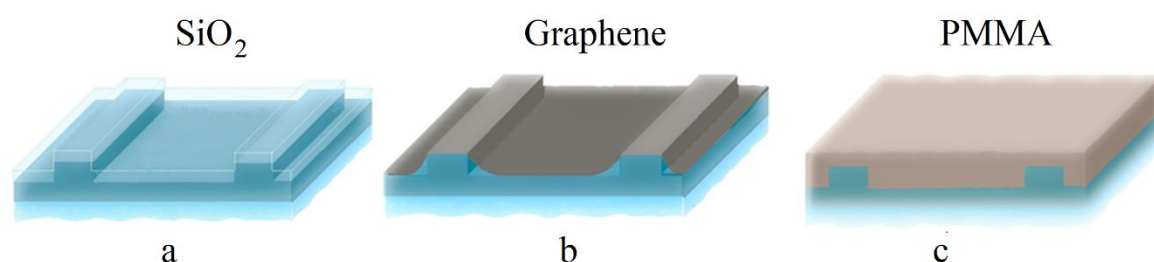
Figure 4.2 Schematic of a nanofabricated device consisting of two parallel bars being protected by a) a conformational layer of SiO₂, b) a partially-conformational layer of graphene, c) a non-conformational layer of PMMA. Adapted from references[1-3].

Meanwhile, some of the other approaches, such as placing a graphene sheet on top of the device are very challenging from the standpoint of nanofabrication.   Finally, covering plasmonic devices with a protective layer of PMMA via direct spinning is relatively straight-forward. However, it has a number of disadvantages including the ability to have highly reproducible ultra-thin PMMA layers and a lack of conformal mapping between the protective layer and the underlying structure. This in turn leads to a tendency for the PMMA to fill in any troughs, or holes in the device potentially impacting performance. Figure 4.2 summarises some of the challenges relating to the ability of the protective layer (e.g. SiO₂, graphene and PMMA) to mimic the underlying nanostructure whilst not impacting device performance.

The need to develop more effective and efficient means of protecting plasmonic devices motivated the present study in which we investigated the use of diamond-like carbon (DLC) as a capping layer. The advantages of using DLC include the fact that it conforms well to the underlying sub-structure and it can be deposited in very thin layers which do not significantly alter the plasmon resonance structure. Finally, DLC is deposited using electron beam induced deposition (EBID) meaning that the protective layer can be deposited onto the device at the same time that the structure is being characterised using SEM. The EBID method of depositing DLC uses volatile organic compounds and a rastered electron beam to locally deposit a conformational film typically only a few nanometres thick. DLC is largely composed of an amorphous layer of carbon in a sp^2/sp^3 hybridisation state[4].

Here, we used plasmonically active Ag nanostructures and subjected them to a range of environmental conditions whilst covered in layers of DLC. Through this study we aimed to determine whether DLC offers a potential solution to the problem of degradation and aging of Ag metallic thin films.

4.1   Diamond-like carbon (DLC)

Diamond-like carbon (DLC) is an amorphous form of carbon which has previously been applied in a range of different thin-film coating applications. The hydrogenated form of DLC is metastable and contains sp^2 and sp^3 bonded carbon (less than 40% is sp^3 hybridized carbon). DLC is an inert, impervious hydrocarbon film with physical and mechanical properties suitable for use in a wide range of research, industrial, and biomedical applications. DLC coatings are characterized by properties similar to diamond such as high

electrical resistance and chemical inertness, high corrosion resistance, low coefficients of friction, and high optical transparency. Figure 4.3 illustrates how DLC, consisting of sp^3, sp^2, and even sp^1 bonded carbon, has a range of properties spanning those of diamond, polymer, and graphite. In spite of the complex topography of DLC films, they can still be readily deposited in conformal and very smooth layers. Metals covered by DLC have been found to exhibit reduced wear and friction coefficients [5, 6].
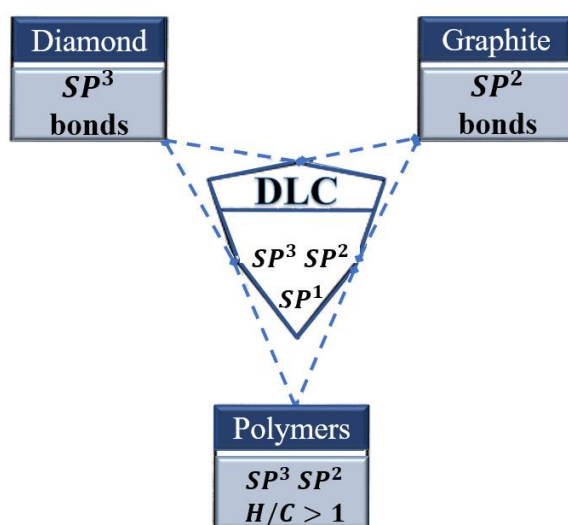
Figure 4.3 *Properties of DLC which include some features of diamond, polymers and graphite. Adapted with permission from reference [6].*

In addition to EBID, DLC can be deposited by physical vapor deposition (PVD), plasma source ion implantation (PSII), or plasma assisted chemical vapor deposition (PECVD) methods. The refractive index, density and hardness of DLC films can be controlled by the bias and temperature of the substrate when using these techniques. However, these approaches to creating DLC coatings result in film thicknesses of the order of microns and are therefore not appropriate to the current application in plasmonics which requires extremely thin, nanometer thick films. Hence, here we choose EBID as the most appropriate and straightforward method for producing DLC layers and which can be accomplished using hydrocarbon gases in an SEM [7].

During SEM imaging, electron back-scattering occurs as the electron beam interacts with an electrically conductive substrate. The back-scattered electrons interact with any intrinsic contamination which is naturally present in the instrument chamber usually in the form of hydrocarbon gases. The resulting interaction leads to the formation of a DLC coating on the substrate. Previous studies have shown that highly conformal and smooth layers of DLC are produced as a result of EBID within the SEM.

4.2   Controlling DLC film thickness via EBID dose

In the present study we examine the protective influence of nanometer thick layers of DLC with respect to aging, deposited on nanostructured Ag thin films in a FIB-SEM, immediately following FIB milling of the films [4, 8, 9]. The thickness of the DLC layer can be controlled by varying the deposition dose and was calibrated in a previously published AFM study[4, 9, 10]; the results are displayed in Figure 4.4.
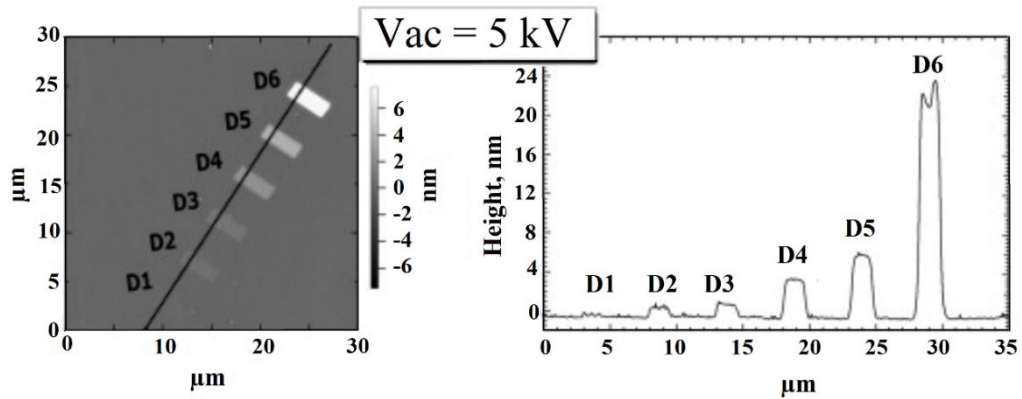
Figure 4.4 *Left: AFM image of pillars of DLC, each with a different height deposited using EBID. Right: corresponding height profile used to estimate the DLC protective film thickness in the present study as a function of the deposition dose. DLC films were deposited using six different e-beam doses (D1=10^3, D2=5×10^3, D3=10^4, D4=5×10^4, D5=10^5 and D6=5×10^5 μC/cm^2) under constant (e.g. 5 kV) acceleration voltage. Adapted from Ref [4].*

The deposition dose under different SEM scanning conditions can be calculated using:

$$D = \frac{Q}{A}$$ (4.1)

where Q is the electric charge equal to $I \times t$ (here I is the beam current used during the scanning and t is the total dwell-time) and A is the exposed area. Table 4.1 summarises the calculated dose and the extrapolated DLC thickness. These values were used to determine the DLC film thickness in the present study.

	A	B	C	D	E	F
Exposure time, μs	0.1	0.5	1.0	10.0	30.0	100.0
Dose $\mu \frac{C}{cm^2}$	0.3	1.4	3.1	23.5	41.3	264.7
Thickness, nm	0.5	0.7	0.8	1.0	1.1	1.2

Table 4.1 *DLC thickness for a range of different exposure times and dose rates.*

4.3   Influence of DLC on performance of plasmonic devices

Prior to investigating whether DLC can be used as a protective layer for Ag-based plasmonic nanostructures, we first wanted to determine whether there was any significant impact on the plasmon resonance structure of these devices. To do this, we covered half of a plasmonic colour filter in a comparatively thick (1.1 nm) layer of DLC at a dose rate of 41.3 μC/cm^2 (column C – Table 4.1). Figure 4.5 shows the brightfield optical microscopy images and corresponding transmission spectra for one of these devices. The periodicity of the cross-shaped nanoapertures was different in the two orthogonal directions resulting in polarisation sensitivity in terms of the optical output. The results for TE, 45^0 and TM incident polarisation states are shown.

A direct comparison of the optical output for the DLC covered and uncovered portions of the freshly prepared devices did not reveal any noticeable differences. From these tests we conclude that incorporating nanometre thick protective layers of DLC do not have any measurable effect on the optical output of these plasmonic nanostructures.
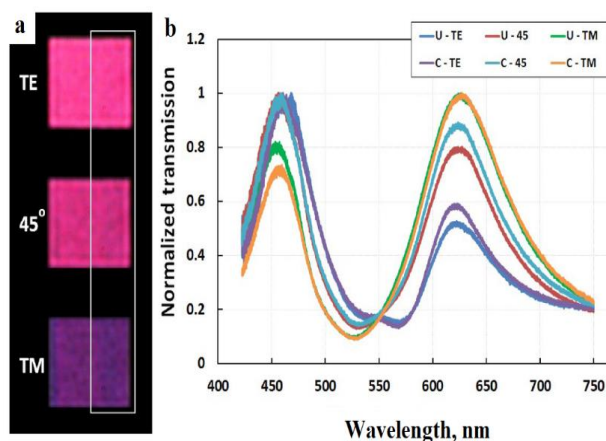
Figure 4.5 *a) Optical brightfield microscopy images and b) corresponding transmission spectra for a polarisation sensitive plasmonic colour filter partially covered with DLC (indicated by the white box). Data were collected using TE, 45° and TM polarised light.*

4.4   Use of DLC to protect against oxidative aging

Previous studies have shown that scanning during SEM imaging induces the deposition of layers of DLC[4]. These layers not only act to protect the underlying substrate, they can also act as an etching mask which can be used in harsh chemical environments including in HF-based electrolytes [11, 12]. To test the protective properties of DLC in the context of Ag plasmonic devices, we fabricated a plasmonic colour filter and covered a small portion of the device in layers of DLC at a dose rate of 264.7 $\mu C/cm^2$ (column D – Table 4.1). Figure 4.6 shows an SEM image of the plasmonic device fabricated in a 150 nm thick Ag film using FIB lithography.
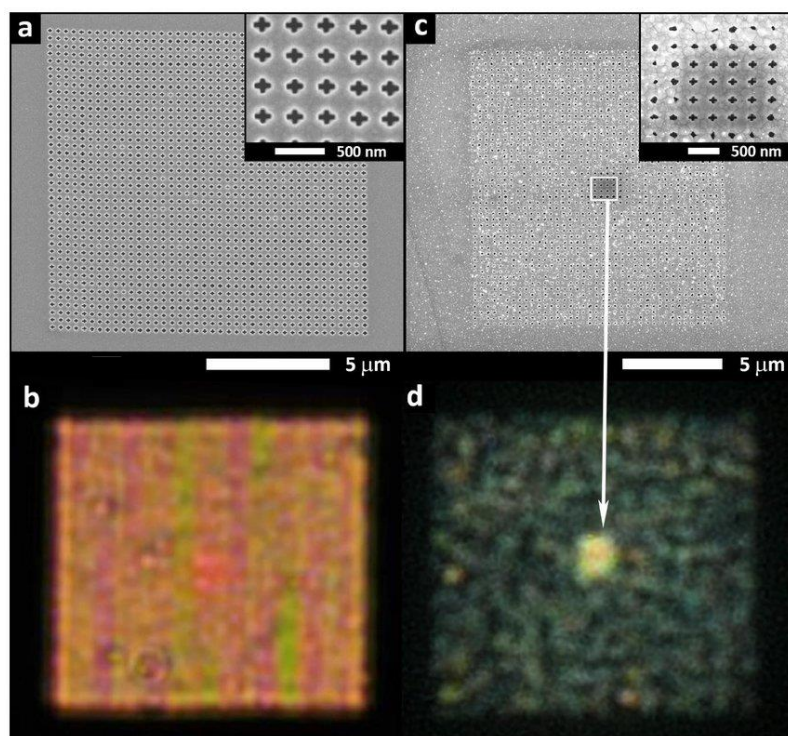
Figure 4.6 *a) SEM image of a plasmonic device immediately after the fabrication using FIB lithography. Note that a small central square in the device was covered by layers of DLC. b) Corresponding bright-field image of the film immediately after fabrication. c) SEM image of the same device after five months left on the benchtop, under ambient conditions, in air. d) Bright-field image of the device in c) showing signs of severe degradation of the optical performance of the unprotected areas.*

The insets in Figures. 4.6a and 4.6c show a higher resolution image of the cross-shaped aperture structures which make up the plasmonic device. Figure 4.6b displays the associated bright-field image straight after fabrication. The SEM image in Figure 4.6c reveals severe topological degradation of the apertures milled into the Ag film after being exposed for five months to air under standard RTP conditions. However, a small square area in the centre of the film which was protected by DLC remains almost unchanged (see inset, Figure 4.6c). The corresponding optical bright-field image of the device (Figure

4.6d), confirmed that 1.2 nm thick layer of DLC deposited at a dose rate of 264.7 µC/cm^2 in the centre of the device retained its plasmonic colour filtering properties whereas the rest of the device was degraded.

4.4.1 Influence of DLC thickness versus resistance to oxidative aging

Having established that DLC had the potential to protect Ag plasmonic devices from oxidative aging, the impact of DLC thickness (controlled via the EBID dose) on the passivation performance of these devices was investigated. For this study two identical periodic arrays of nano-apertures (P_x :320, P_y :280 nm and L_x :160, L_y :140 nm) were fabricated in Ag using the FIB lithography and subjected to two different EBID doses: 0.3 $\mu C/cm^2$ (sample A) and 1.4 $\mu C/cm^2$ (sample B). This resulted in an estimated DLC protective layer thickness of 0.5 and 0.7 nm for samples A and B respectively (see Table 4.1). Figure 4.7 shows SEM images of the device immediately after the fabrication (a) consisting of 40×40 and (b) consisting 3×3 nano-apertures.
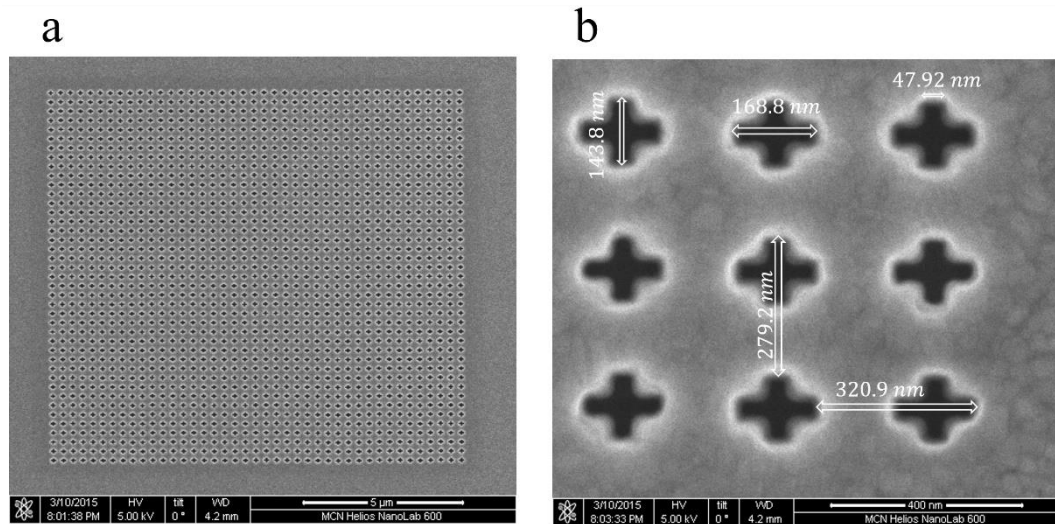
Figure 4.7 *a) SEM image of 40×40 array. b) Unit cell with higher magnification highlighting the dimensions of the structures.*

Following measurement of the transmission spectra for these samples immediately following fabrication, both samples were exposed for six months to air under standard RTP conditions. After this, the transmission spectra were again collected from both patterns. Figure 4.8 compares the transmission spectra before and after the ageing process.
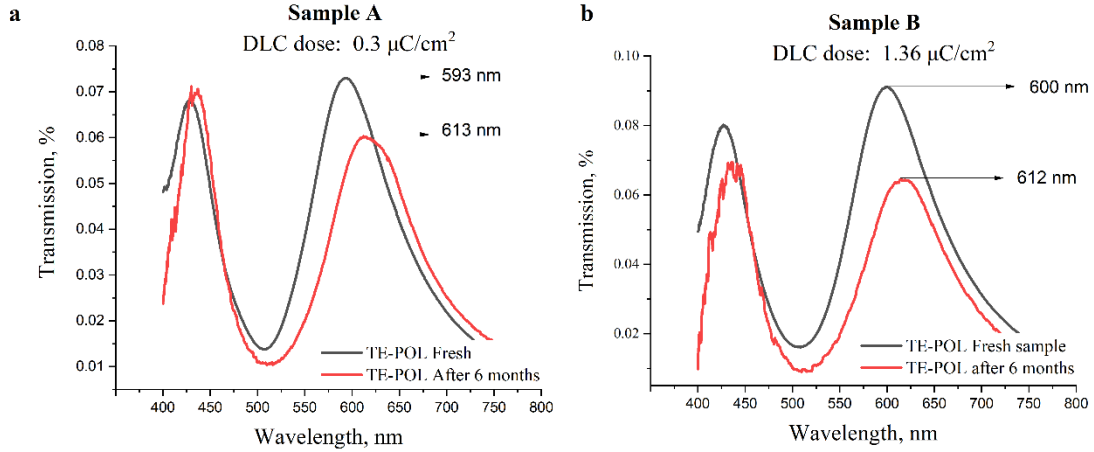
Figure 4.8 *Comparison between the spectra of a freshly prepared plasmonic colour filter and one that has been exposed to air for six months. a) Sample A: the main resonance peak experienced a* 20 *nm redshift following oxidative aging. b)* *Sample B*: *the main resonant peak experienced a* 12 *nm redshift following oxidative aging.*

From the transmission spectra, it is clear that both patterns retained their plasmonic performance following six months of exposure to air albeit with some detectable differences in the position of the principal resonance peak. We hypothesise that this shift in peak position for sample A (20 nm) could be due to a minor degradation of the cross-shaped apertures. We also observe that the shift in peak position is less for sample B (12 nm) which was exposed to a higher DLC deposition dose and consequently was covered by a thicker protective layer (0.7 nm for sample B versus 0.5 nm for sample A – see Table 4.1).

4.4.2 DLC resistance to performance degradation in water

Following the tests of DLC resistance to oxidative aging we next carried out a series of tests on DLC protected Ag-based plasmonic devices submerged in water. These tests were to demonstrate the applicability of DLC protected Ag devices to applications involving chemical sensing. For these studies a 0.8 nm thick DLC protective layer at a dose rate of 3.1 $\mu C/cm^2$ was used (see Table 4.1). Two identical patterns (here labelled 'A' and 'B') with P_x = 350 and P_y =300 nm pitch and L_x =160 and L_y =140 nm arm length were fabricated in the same Ag thin film. A Schematic illustration of the cross-shaped aperture arrays used in the present study is shown in Figure 4.9.
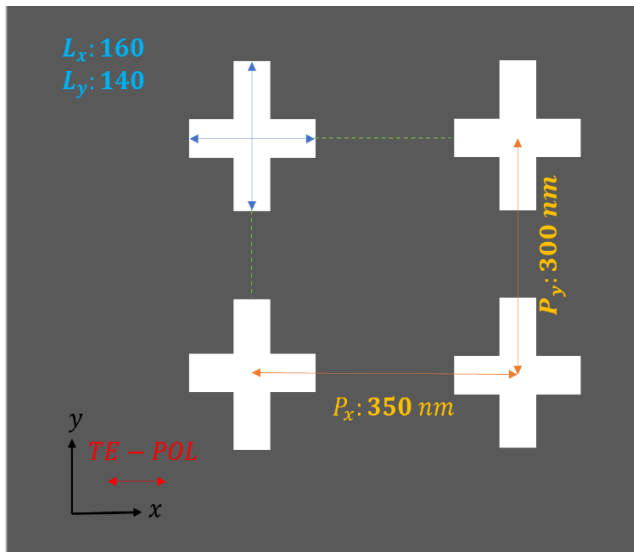
Figure 4.9 Schematic of the cross-shaped aperture array. The apertures have dimensions of L_x=160 and L_y=140 nm. The array periodicity is given by P_x=350 and P_y=300 nm. The green dash lines indicate the distances between the edge of the crosses.

For this test only pattern B was covered by the DLC protective film whilst pattern A was left exposed. The two patterns were submerged in water under standard RTP conditions. To minimise the effects of oxidative aging the tests were performed on the devices immediately following device fabrication. The devices were left under water but removed briefly at 24, 48, and 168 hours in order to record optical brightfield images. Following

removal from water and prior to optical characterisation a nitrogen gas stream was used to dry the sample. Figure 4.10 presents a summary of the results for the TE, 45°, and TM, incident polarisation modes.
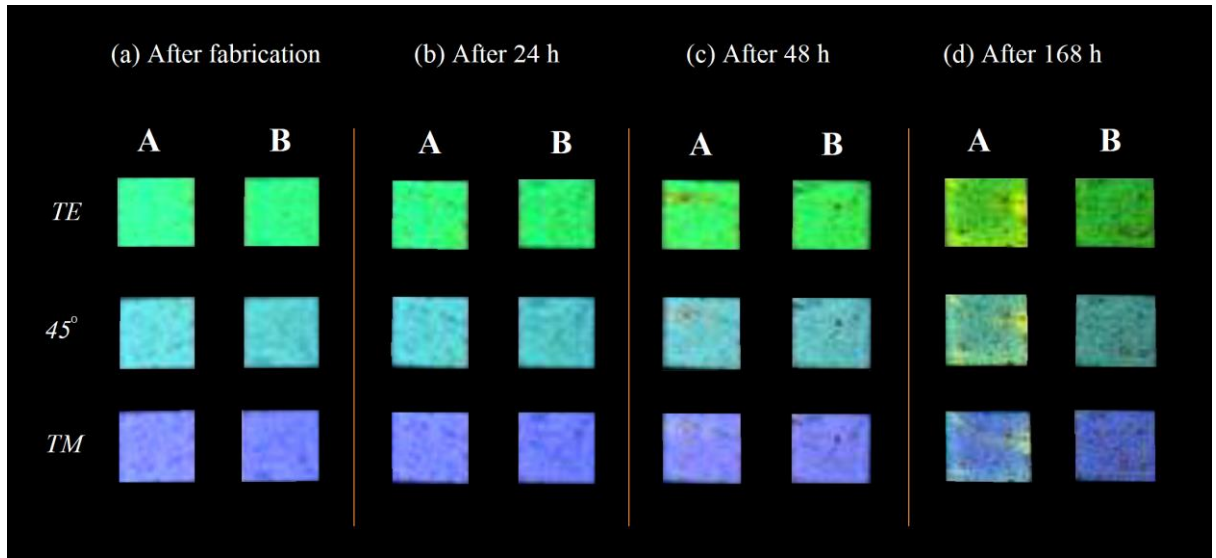
Figure 4.10 *Optical brightfield images of an uncovered (A) and a DLC covered plasmonic colour filter(B). a) freshly preparred patterns. b-d) immersed in water for a period of 24, 48 and 168 hours, respectively. The images were taken at TE, 45° and TM polarization modes after drying the samples.*

We observe that after 168 hours submerged in water both the DLC covered and uncovered samples exhibit signs of aging. However, the DLC covered device (B) exhibits substantially less degradation. The water damaged areas on the uncovered plasmonic devices are shown in Figure 4.11 (indicated by the white arrows) for uncovered sample. We note that the polarisation sensitivity of the damaged areas is no longer present.
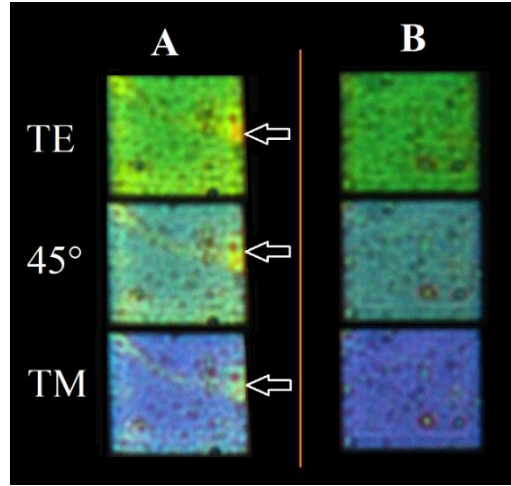
Figure 4.11 *The uncovered sample versus covered one after 168 h in water shown for three different incident polarisation modes (TE, 45°, TM).*

Figure 4.12 displays the associated transmission spectra under TE, 45° and TM polarization modes normalized to the incident light. The position of the observed peaks and maximum redshift at the end of the experiment are illustrated in Table 4.2.
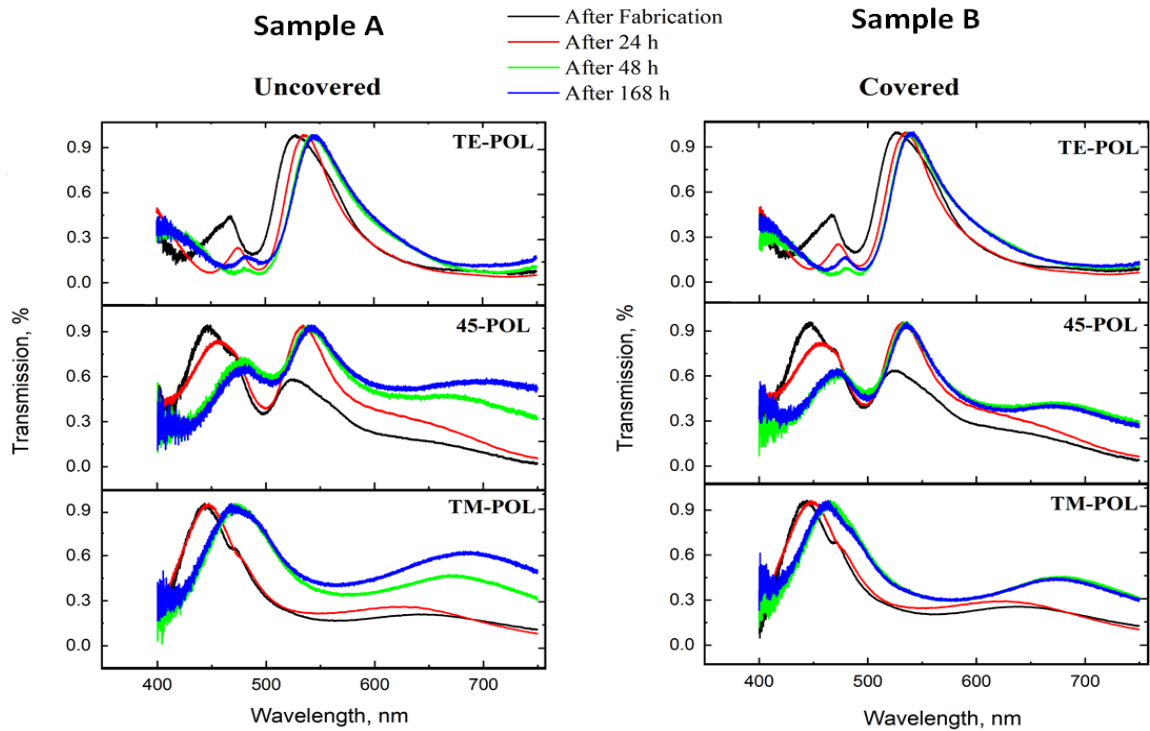
Figure 4.12 *Comparison of spectra collected from an uncovered and DLC covered plasmonic colour filter for TE, 45° and TM incident polarizations.*

Sample POL		A TE	B TE	A 45°	B 45°	A 45°	B 45°	A TM	B TM
				Right peak	Right peak	Left peak	Left peak		
Peak position	**fresh**	528	529	528	527	447	446	443	445
	24 h	535	534	534	532	456	452	450	450
	48 h	543	536	539	533	460	456	468	463
	168 h	544	541	542	536	464	458	471	466
Final redshift		15	12	14	9	17	12	28	21

Table 4.2 *Comparison of observed peaks at the end of all experiments stage collected for uncovered and covered sample. The final redshift after 168 h calculated for TE, 45° and TM polarization modes.*

After 24 h of being left in water we observe a redshift in the measured transmission spectra for both the uncovered and DLC covered plasmonic devices. However, in the case of the DLC covered device the redshift (as measured from the principle plasmonic resonance peak) was ~5 nm versus ~7 nm for the uncovered device. A possible explanation for the observed redshift even with the DLC protective overlayer is that the dose used and resulting DLC film thickness (column C, Table 4.1) was not sufficient to form a complete protective layer against liquids. However, after 24 hours the uncovered sample had larger shift compare to covered one (~8 nm versus ~2 nm in TE polarization mode). Interestingly, the amount of redshift for TM polarization mode at this stage is much bigger than TM mode (~18 nm). Furthermore, the amount of redshift under 45° polarization mode was smaller for the peaks near the TE mode's peaks (right peak). The amount of redshift for uncovered

device increases much more than the covered one at the end of 48 and 168hours. The final observed redshift for both samples exhibits larger redshift for TM polarization mode (see Figure 4.12 and Table 4.2). The spectra for both devices revealed more redshift for TM polarization. This effect could be attributed to a smaller Ag surface area which did not lead to a continuous Ag film in y-direction. The distance between adjacent cross-shaped apertures in y-directon is less than in x-direction (see Figure 4.9), therfore, the overall continuous Ag surface area in y-direction was less compared to the surface area in x-direction. Finally, the uncovered sample which, at 168 h submerged in water, reveals sections of the plasmonic device that have degraded to the point of no longer exhibiting any polarisation sensitivity.

4.4.3 DLC resistance to performance degradation in harsh environments

Having demonstrated the benefits of DLC protection in water we next wanted to study the performance of DLC protected Ag plasmonic devices in more aggressive chemical environments. The goal was to further demonstrate the utility of DLC covered plasmonic devices for a wider range of sensing applications. For the first part of this test we exposed a Ag plasmonic device to an iodine-containing gas – known to be a very aggressive Ag etchant. A portion of the device was covered with a 1.2 nm thick layer of DLC deposited at a dose of 264.7 $\mu C/cm^2$ (see Table 4.1).

Figure 4.13a shows example optical brightfield images collected from this device at standard RTP before (1) and after (2) exposure to iodine-containing gas at three different incident polarisations (TE, 45˚, and TM). There is a striking difference in the optical output of the regions covered by DLC (indicated by the white rectangles in Figure 4.13b) and the uncovered regions.
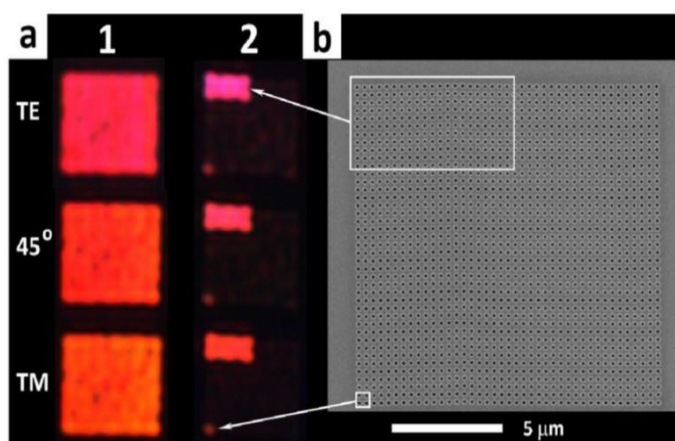
Figure 4.13 a) Optical images of the sample before (a₁) and after (a₂) exposure to iodine-containing gas taken under three different polarizations. b) SEM image showing areas protected by the DLC film.

We observe that the DLC protective film was able to prevent any damage to the Ag film caused by interaction with the iodine gas and that the protected regions continued to exhibit full colour transmission for all incident polarisations.

Following the tests in iodine gas, the effectiveness of DLC in protecting Ag plasmonic devices in harsh liquid chemical environments was studied. For this test half of the Ag plasmonic device was coated in a 1.1 nm thick layer of DLC deposited at a dose of $41.3\ \mu C/cm^2$ (see Table 4.1). The device was then immersed in poly diallyldimethylammonium chloride for 1 hour and 3 hours respectively. Figure 4.14 shows example optical brightfield images of this device, comparing the output of the uncovered and DLC covered halves of the sample.
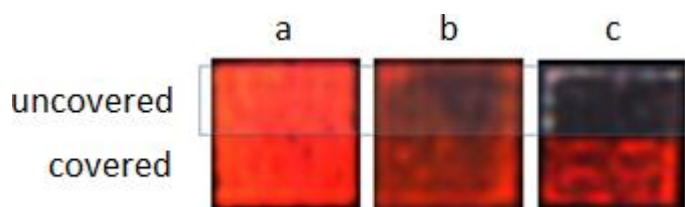
Figure 4.14 Optical brightfield images collected under TE-polarisation mode from a Ag plasmonic device half covered in DLC. a) immediately after fabrication and after immersion in poly diallyldimethylammonium chloride for b) 1 hour and c) 3 hours.

Although both the uncovered and DLC covered halves of the plasmonic device undergo some degradation when immersed in poly diallyldimethylammonium chloride, it is clear that the uncovered portion undergoes substantially more damage than the covered portion.

4.5   Conclusions

Electron-beam induced deposition techniques using volatile organic compounds can be used to deposit nanometer thin amorphous diamond-like carbon films. Incorporation of DLC on surface of a plasmonic device lead to an ultra-thin and conformational protection layer. The use of DLC as a passivating layer for Ag based plasmonic devices against degradation was demonstrated and the influence of DLC thickness to oxidative aging was discussed. It was concluded that the DLC has the benefits of negligible impact on the device optical performance.

The current work revealed that the protection efficiency is a function of used e-beam doses, and higher doses show better protection performance against oxidation under ambient conditions owing to increase of deposited carbon amount and increase of DLC height. DLC films as thin as ~ 1.1 nm (deposited at a dose of 41.3 and 264.7 $\mu C/cm^2$) were proven to demonstrate this ability even in harsh chemical environments, making this method most suited for high-sensitivity chemical and molecular sensing applications. Furthermore, the effect of the smallest applied dose (10^3 $\mu C/cm^2$) was investigated. The amount of 0.5 nm thick DLC could not protect the device well, this effect could be attributed to the lowest dose rate which did not lead to a continuous DLC film.

4.6   References

1.   Li, Y., *Monolayer protection for eletrochemical migration control in silver nanocomposite.* Applied physics letters, 2006. **89**.

2.   Pratsinis, S.E., *Aerosol-based technologies in nanoscale manufacturing: from functional materials to devices through core chemical engineering.* AIChE journal, 2010. **56**(12): p. 3028-3035.

3.   Floris, F., et al., *Optical sensitivity gain in silica-coated plasmonic nanostructures.* The journal of physical chemistry letters, 2014. **5**(17): p. 2935-2940.

4.   Balaur, E. and A.G. Peele, *Tunnelling through diamond-like carbon nanofilms deposited by electron-beam-induced deposition.* Thin solid films, 2009. **517**(24): p. 6520-6526.

5.   Thomson, L.A., et al., *Biocompatibility of diamond-like carbon coating.* Biomaterials, 1991. **12**(1): p. 37-40.

6.   Grill, A., *Diamond-like carbon: state of the art.* Diamond and related materials, 1999. **8**(2-5): p. 428-434.

7.   Grill, A., *Diamond-like carbon coatings as biocompatible materials—an overview.* Diamond and related materials, 2003. **12**(2): p. 166-170.

8.   Adhikary, S., et al., *Bonding defects and optical band gaps of DLC films deposited by microwave surface-wave plasma CVD.* Diamond and related materials, 2005. **14**(11-12): p. 1832-1834.

9.   Djenizian, T., E. Balaur, and P. Schmuki, *Direct immobilization of DNA on diamond-like carbon nanodots.* Nanotechnology, 2006. **17**(8): p. 2004.

10.   Tsai, H.c. and D.B. Bogy, *Characterization of diamondlike carbon films and their application as overcoats on thin-film media for magnetic recording.* Journal of

Vacuum Science & Technology A: Vacuum, Surfaces, and Films, 1987. **5**(6): p. 3287-3312.

11.   Balaur, E., et al., *Electron beam-induced modification of organic monolayers on Si (1 1 1) surfaces used for selective electrodeposition.* Electrochemistry communications, 2004. **6**(2): p. 153-157.

12.   Zhang, Y., et al., *Nanopatterning of Si (1 1 1) surfaces by atomic force microscope scratching of an organic monolayer.* Electrochemistry communications, 2003. **5**(4): p. 337-340.

CHAPTER 5

BIMODAL PLASMONIC SENSORS FOR ION IMPLANTATION

5   INTRODUCTION

Plasmonic metamaterials have been researched extensively for a wide range of applications including chemical and molecular sensing. Using the phenomenon of Extraordinary Optical Transmission (EOT) these devices are able to sense extremely small changes in the local dielectric constant within the near-surface region. Whilst these materials have received significant attention as sensors for the liquid and gas phase, their use in the detection of the optoelectronic properties of solid-state samples has been less-well studied. This chapter includes an exploration of the application of bimodal plasmonic to detecting changes in the local optoelectronic properties of ion implanted thin films. This is described in the incorporated paper submitted to Advanced Functional Materials: "Bimodal plasmonic colour filters enable direct optical imaging of ion implantation in thin films".

5.1   Local refractive index sensing using biomodal plasmonic devices

The increased versatility and dynamic range of bimodal plasmonic devices offers greater levels of sensitivity for converting small changes in the samples' dielectric constant into shifts in the resonant peak positions which make up the measured transmitted spectrum of the device. These shifts in resonant peak position can be quantitatively modelled via empirical equations based on the device parameters and incident spectrum [1].

Changes in the TiO_2 band-gap (E_g = 3.0 to 3.2 eV) affect the rate of light absorption and alter its photosensitivity [2]. Previous investigations have shown that reducing the bandgap can lead to enhanced light absorption, specifically in the visible region [3]. Doping TiO_2 with metal and non-metal ions plays a crucial role in determining the optoelectronic

properties of TiO$_2$ which has important implications for their application in a wide range of different devices. In particular, gallium ion implantation of TiO$_2$ has been found to be highly effective in tailoring its band gap [4]. Previous experimental work has shown that the carrier concentration in TiO$_2$ increases as a function of the gallium ion implantation dose which in turn has a strong effect on the refractive index of implanted TiO$_2$. A higher concentration of impurities has been found to make the configuration of the band-gap more stable leading to improvements in the light absorption performance inducing a redshift (smaller band-gap) [3]. The optical response of a non-homogenous, complex medium can be characterised in terms of the complex dielectric constant, $\varepsilon(\omega)$. In principle, $\varepsilon(\omega)$ describes how strongly an external electric field polarizes the charge carriers within a given material which would influence the coupling between surface plasmons and the electronic structure of the material.

It is important to consider both the real and imaginary parts of the complex dielectric function together because, according to the Kramers-Kronig relation, they exhibit a degree of interdependency [5, 6] . The real part of the equation describes how strongly an external electric field can polarize the material whilst the imaginary part describes the ohmic losses due to electron-electron interactions and inter-band electronic transitions [7-10]. The link between the dielectric constant and the complex refractive index derives from Maxwell's equations

$$\varepsilon(\omega) = n'(\omega)^2 = \big(n(\omega) + ik(\omega)\big)^2 \tag{5.1}$$

where $n'(\omega)$ is the frequency dependant complex refractive index which characterises the optical properties of the material [11, 12]. The coupling of light with the electronic structure of metamaterials is described by the equations governing the Surface Plasmon (SP) modes; this includes both long-range Surface Plasmon Polaritons (SPPs) and Localised Surface

Plasmons (LSPs). Other plasmon related phenomena such as Wood-Rayleigh Anomalies (RA) can be used to experimentally determine the values of the real component of the refractive index [13-20].

5.2　Ion implantation mechanisms in thin films

In order to corelate the optoelectronic properties of the implanted TiO_2 regions with the plasmon resonance spectra, it is important to understand the mechanisms that induce changes in the local dielectric constant during the implantation process. The electronic stopping mechanism for ions entering the target material results in vacancy-interstitials. The total distance travelled by an ion prior to stopping is called the ion range (or ion implantation depth) and for the current study, the total displacement and range of ion in the target lattice (TiO_2) was calculated by using the stopping and range of ions in matter (SRIM) Monte Carlo simulation software [21, 22]

5.2.1　Transport of ions in matter

The SRIM program calculates the interaction of ions in solids based on the Monte Carlo simulation method. The programme simulates the trajectories of energetic ions in matter and evaluates their energy loss and final stopping ranges within the solid. Here SRIM was used to evaluate the effects of gallium ion implantation on the TiO_2 lattice such as excitation or displacement by the ions. It was also used to determine the energy losses for the ion due to either electronic or nuclear interactions with the target atoms. An extension of SRIM is known as the Transport of Ions in Matter (TRIM) method which is used to calculate ion penetration depths over a wide range of incident energies. Using TRIM the ion trajectories can be plotted in both 2D and 3D and the resulting information used to estimate the volume and density of the ion implantation. Figure 5.1 presents an example result outputted using TRIM for 16 keV gallium ions incident upon TiO_2.
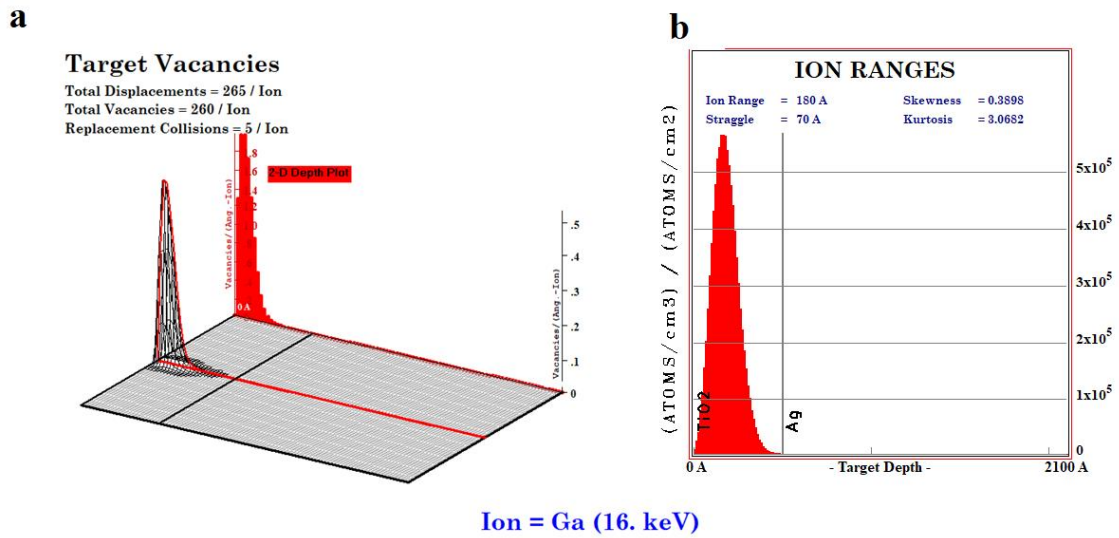
Figure 5.1 The concentration of impurities (ions and vacancies) within the target calculated using the TRIM software. a) A 3-D view of ion displacements within the target and a 2-D plot of the depth of penetration of the ions. b) The ion ranges and corresponding statistical moments. This peak can be used to obtain the distribution of defect densities within the target.

5.3 Paper

Table 5.1 Candidate and co-author contributions

Manuscript title	"**Bimodal plasmonic colour filters enable direct optical imaging of ion implantation in thin films**"
Journal	Advanced Functional Materials
Publication status	Under review
Authors	**C. Sadatnajafi**, E. Balaur, and B. Abbey
Nature and extent of candidates contribution	Sixty percent including data collection, data processing and analysis, image reconstructions, interpretation of results, and drafting of the paper and manuscript revisions.
Nature and extent of co-authors contribution	Forty percent including data analysis, drafting of paper manuscript and revisions and critical review.

WILEY-VCH

Title: Bimodal plasmonic colour filters enable direct optical imaging of ion implantation in thin films

C. Sadatnajafi[1,2], E. Balaur,[1,2]* and B. Abbey[1,2]*

Dr E. Balaur, Prof. Brian Abbey

Australian Research Council Centre of Excellence for Advanced Molecular Imaging, Department of Chemistry and Physics, La Trobe Institute for Molecular Science (LIMS), La Trobe University, Victoria 3086, Australia
E-mail: e.balaur@latrobe.edu.au, b.abbey@latrobe.edu.au

Ms C. Sadatnajafi,
Australian Research Council Centre of Excellence for Advanced Molecular Imaging, Department of Chemistry and Physics, La Trobe Institute for Molecular Science (LIMS), La Trobe University, Victoria 3086, Australia

Optical metamaterials offer precise control over the properties and interactions of light at the nanoscale, attracting interest in many new fields of research including chemical and molecular sensing, magnetic antennas, and photovoltaic elements. By utilizing the phenomenon of Extraordinary Optical Transmission (EOT) plasmonic devices enable the detection of minute changes in the local, near-surface, dielectric properties of materials, opening up a wide range of different applications [1-9]. Characterization of the optoelectronic properties of ultra-thin films is of paramount importance for a wide range of electronic applications including integrated circuit production [10-14]. However, it is often extremely difficult to achieve using conventional imaging techniques. Here we demonstrate that plasmonic colour filters can be used for the direct optical imaging and characterization of ion implantation in thin films. We use a model system consisting of variable doses of gallium ions implanted within titanium oxide thin films. We observe that the ion implantation dose leads to a variation in the measured plasmon resonance spectra which can be further enhanced through the use of bimodal nanopixel arrays. Using Monte Carlo simulations and the Maxwell-Garnett relation, we quantitatively interpret the observed plasmon resonance spectra in terms of the gallium ion implantation dose.

1

WILEY-VCH

1. Introduction

Direct detection of local changes in the dielectric properties of nanometre-thin films is important for a wide range of electronic applications [7,15-17]. Ion implantation is routinely used in integrated circuit production and new approaches to characterising ion implantation doses are continuously being researched and have attracted significant interest[18]. Techniques such as impedence spectroscopy[19] and ellipsometry[20] have been previously employed to try and probe the optoelectronic properties of thin films as a function of implantation fluence. However, plasmonic colour filters offer a simple and direct alternative means for non-destructively characterising these types of samples optically. These types of optical sensor are particularly useful in the case of very thin films where techniques such as Secondary Ion Mass Spectrometry (SIMS) or Time-of-Flight (ToF)-SIMS are currently used to study dopant profiles[21].

Here we describe and demonstrate the direct visualisation of ion implantation in a thin film (titanium oxide, TiO_2) based on analysis of the brightfield optical images and plasmon resonance spectrum generated by bimodal plasmonic colour filters. By measuring the optical output for these devices at two different polarisation states, the relative sensitivity of the plasmon resonance transmission spectra to ion implantation can be assessed and optimised. In this approach the behaviour of the local Refractive Index (RI) of the TiO_2 film, placed within the evanescent field of a plasmonic device, is used to investigate the effect of doping using gallium ions (Ga^+). Examination of the critical parameters involved in this process allow us to determine values of the optical constant and extinction coefficient for the ion-implanted TiO_2. An important consequence of Ga doping of TiO_2 is that gallium ion substitution has been shown to significantly improve the stability of the TiO_2 lattice and to have a strong influence on its optoelectronic properties [22-25].

Previously bimodal plasmonic nanopixel arrays combined with polarisation control have shown great promise as both colour filters and chemical sensors [6,7,26,27]. The increased

2

versatility and dynamic range of bimodal plasmonic devices offers even greater levels of sensitivity then single mode devices for converting small changes in the samples' dielectric constant into significant modifications of the measured transmitted spectrum of the device. Shifts in resonant peak position, peak height, and peak width can be modelled based on the device parameters and incident spectrum in order to quantiatively characterise the sample [6].

Variations in the TiO_2 band-gap (E_g = 3.0 to 3.2 eV) affect the optoelectronic properties of the material including altering its photosensitivity [28]. Previous investigations have shown that reducing the bandgap can lead to enhanced optical absorption, specifically in the visible region [29]. It is now understood that doping TiO_2 with either metal or non-metal ions plays a crucial role in modifying the optical properties of TiO_2. Until recently, Ga ion implantation was used to achieve a narrower TiO_2 band-gap [30]. It has been experimentally shown that the carrier concentration in TiO_2 increases as a function of the implantation dose, this in turn has a strong effect on the refractive index of implanted TiO_2. A higher concentration of impurities can make the configuration of the band-gap more stable and can improve the light absorption performance inducing a redshift (decreased band-gap) [29]. However, beyond a critical level of doping, further increases in the density of ion impurities do not have a significant impact on the band-gap and consequently the optical absorption does not change[30,31]. In principle, the permittivity (dielectric function) of hybrid materials is a complex function because of the polarizability of the dielectric/metal matrix. The electric permittivity describes how strongly an external electric field polarizes the charge carriers within a given material. The optical response of a non-homogenous, complex medium, can be characterised in terms of the electric permittivity, $\varepsilon(\omega)$, of the medium described by

$$\varepsilon(\omega) = \varepsilon_\infty - \varepsilon'(\omega) + i\varepsilon''(\omega). \tag{1}$$

3

For each material ε_∞ is the contribution owing to the bound electrons and is approximated as a constant value, whilst $\varepsilon'(\omega)$ and $\varepsilon''(\omega)$ represent the real and imaginary part of the dielectric function, respectively. The complex function of electric permittivity is a frequency dependent function. It is crucial to consider both the real and imaginary parts of this function together because, according to the Kramers-Kronig relation, they exhibit an interdependency [32,33]. The real part of the equation describes how strongly an external electric field can polarize the material whilst the imaginary part describes the ohmic losses due to electron-electron interactions and inter-band electronic transitions [34-37]. The link between the electric permittivity and refractive index can be derived from Maxwell's equations as

$$\varepsilon(\omega) = n'(\omega)^2 = \big(n(\omega) + ik(\omega)\big)^2 \tag{2}$$

where $n'(\omega)$ is the frequency dependant complex refractive index which characterises the optical properties of the material with $n(\omega)$ and $k(\omega)$ the real and imaginary components respectively [38,39]. The coupling of light with the electronic structure of metamaterials is described by the equations governing the Surface Plasmon (SP) modes; this includes both long-range Surface Plasmon Polaritons (SPPs) and Localised Surface Plasmons (LSPs). Other plasmon related phenomena include Wood-Rayleigh Anomalies (RA) which can be used to determine the values of the real component of the refractive index[40-47].

4

2. Materials and Method
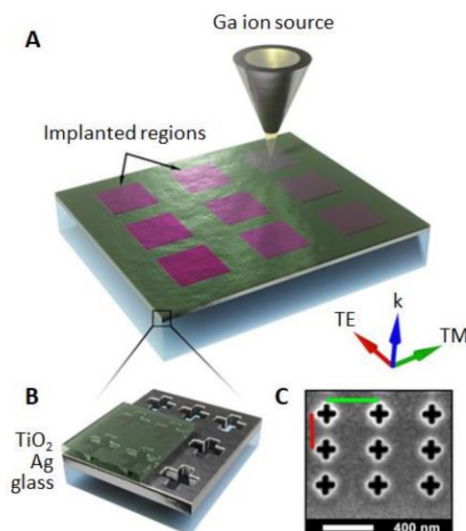
Figure 1. A) Schematic of the plasmonic device/TiO_2 being implanted with Ga^+ ions. The Ga ion source was raster scanned over nine separate square (2.5 × 2.5 μm) regions with a varying implantation dose. The beam diameter, r, was 10 nm. B) The device structure consisted of an Ag film containing a periodic array of cross-shaped apertures covered by a TiO_2 thin film. C) SEM image of the plasmonic device. P_x (green line) and P_y (red line) are the array periodicities in the X and Y directions equal to 400 and 300 nm respectively.

To experimentally determine if bimodal plasmonic arrays could be used to detect Ga ion implantation, nine areas of varying Ga ion implantation dose were created using a Focused Ion Beam (FIB) system (see **Figure 1**A). For each implantation area, the beam was raster-scanned in a square pattern in order to achieve a homogeneous distribution of ions within the implanted zone. All implanted areas were later evaluated using a spectrometer and an optical bright-field microscope. The device architecture prior to ion implantation is shown in **Figure 1**B; a high-resolution SEM image of the pattern is shown in **Figure 1**C. A summary of the experimental ion implantation parameters based on the known Ga ion fluences and ion beam diameter is given in Table 1.

5

WILEY-VCH

Table 1. Ion fluence and number of ions contained within the cross-section of the ion beam. Note that the beam diameter = 10 nm, equivalent to an ion implantation area of 78.5 nm^2.

Implantation area	Ion fluence × 10^{13} [ions/cm^2]	Number of ions contained in beam [ions/beam area]
D0	0	0
D1	2	16
D2	4	32
D3	6	48
D4	12	96
D5	26	208
D6	50	400
D7	100	800
D8	200	1600
D9	400	3200

3. Results and discussion

In order to investigate the use of plasmonics for direct imaging of ion implantation, optical images were collected using both a bare glass substrate and the bimodal plasmonic device as a substrate for the TiO$_2$ thin-film. **Figure 2** shows the optical images and corresponding data analysis, collected in bright-field mode, using using the plasmonic device. In **Figure 2**A The ion implanted regions are labelled 1 to 9 with `1` indicating the lowest dose and `9` the highest. Two different incident polarisation modes were used. In **Figure 2**A the results for the transverse electric (TE) and in **Figure 2**B the results for the transverse magnetic (TM) are shown .

6

148
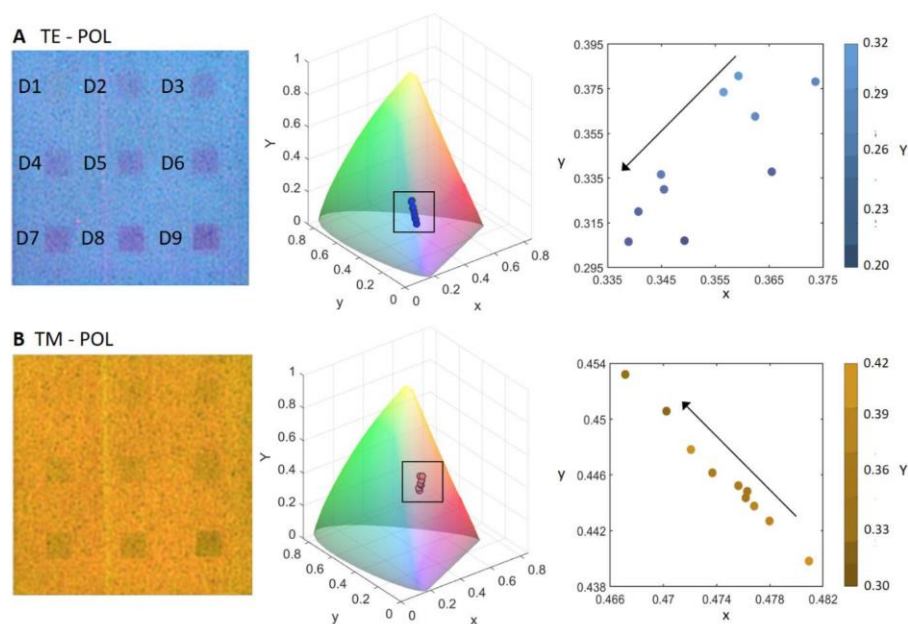
Figure 2. Bright-field optical images of the Ga-ion implanted TiO$_2$ thin film on the plasmonic device (left), corresponding colour output plotted in the CIE 1976 xyY colour space on a 3D chromaticity diagram, with x and y specifying the chromaticity and Y the luminescence (middle). An enlarged plot showing the x-y chromaticity values is also presented (right). Results are shown for both A) transverse electric (TE) and B) transverse magnetic (TM) incident polarisations. The black arrows indicate the direction of increasing Ga ion implantation.

Figure 2 shows that the chromoticity output of the ion implanted regions for both the TE and

TM incident polarisation only displays a relatively small variation as a function of implantation

dose.The peak output for the devices is within the blue region of the spectrum for the TE mode

and within the orange region of the spectrum for the TM mode. The variation in terms of the

brightness is much greater than the chromaticity and can be observed directly `by eye` with

around a 40% variation in the measured signal for both TM and TE modes. This was confirmed

through measurement of the normalised line-profiles measured across the ion implanted areas

which are shown in **Figure 3**. A dramatic increase (~ 450%) in the absorption due to ion

implantation is observed when using the plasmonic device compared to the sample implantation

dose measured on glass alone due to the change in the height and position of the resonant peaks

7

when using plasmonics. The result is that by using the plasmonic device even areas at the lower

end of the scale in terms of the number of implanted ions are clearly distinguishable 'by eye'

whereas the signal is virutally undetectable on glass.
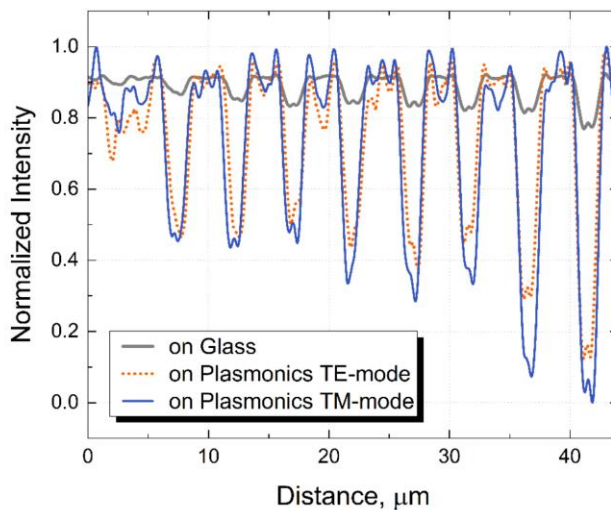
Figure 3. Line profiles taken through the middle of each of the 9 ion implanted squares. Moving from left to right on the plot the ion implantation dose decreases corresponding to squares 1 → 9. The images on the plasmonic device clearly show significant variation in the measured intensity as a function of the implantation dose consistent with the results in **Figure 2**.

In contrast to the glass/TiO$_2$ sample where transmission is mainly characterized by classical

absorption, transmission through the plasmonic/TiO$_2$ sample is determined via coupling of the

incident light to the SPs and LSPs. This is because the TiO$_2$ thin film (50 nm) is thinner than

the 'skin depth' for this material (around 69 nm for a 600 nm incident wavelength). Therefore,

changes in the dielectric constant of the TiO$_2$ thin film due to the presence of Ga ions are

detectable as changes in the plasmonic resonant peak structure. These changes can be further

enhanced and quantified by varying the polarisation of the illuminating field. **Figure 3** shows

the measured transmission spectra as a function of the incident wavelength from all 9 implanted

8

areas (D1-D9) as well as the uninplanted TiO_2 thin film at both TE and TM incident polarizations (D0).

As the implantation dose increases, the transmission through the implanted areas significantly decreases (**Figure 2** and **Figure 3**), with a corresponding small change in the output colour detected (**Figure 2**). The results of the analysis of the optical brightfield images are confirmed when looking at transmission spectra measured using a spectrometer (**Figure 4**). Very little variation in the position of the primary plasmon resonance peaks is observed as a function of increasing implantation dose which is consistent with the lack of strong colour contrast as a function of Ga ion density. As expected though, due to the coupling of the surface plasmons (SPs) and localised surface plasmons (LSP) to ion implanted TiO_2 there is a significant difference in the peak height. We observe that the difference between the implanted and unimplanted areas is greater when the sample is illuminated using the TM polarization, which is associated with the larger periodicity (400 nm) for the device compared to TE polarization. Typically, any changes in the real part of the refractive index of a material probed by a plasmonic device lead to a shift of the resonant peak position (i.e. a red shift is expected if the refractive index increases). In the case of the TiO_2 thin film, since the resonant peak position remains approximately constant, it is the changes in the height of the resonance peak, described by the imaginary part of the refractive index, which provides the greatest optical contrast.

9
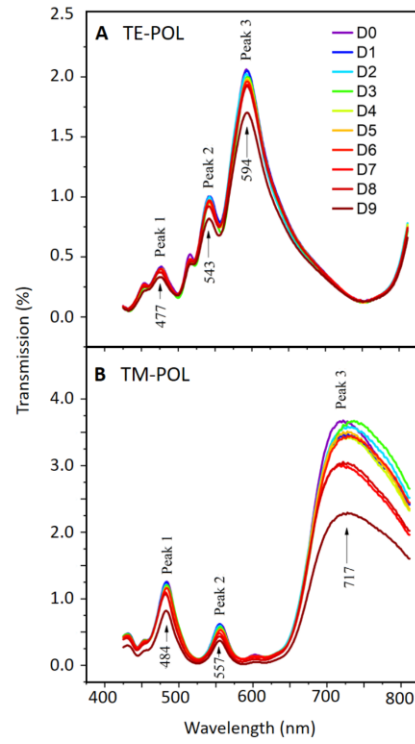
Figure 4. The transmitted intensity spectra measured as a function of wavelength for the plasmonic/TiO$_2$ sample taken from the unimplanted TiO$_2$ film (D0) and all nine Ga ion implanted areas (D1-D9) at both A) TE and B) TM incident polarizations.

The origin of the three plasmon resonance peaks: peak 1, peak 2, and peak 3 (P$_1$, P$_2$, and P$_3$) is associated with the different Bloch modes for the dielectric/metal SPPs, cavity LSPs, and RAs of the grating; each of which has a different mechanism of electric field propagation. The generalised dispersion relation describing the resonant peaks associated with the different Bloch modes in periodic rectangular arrays in metal films are given in the first approximation as [48]

$$\lambda_{SPP} \cong \frac{P}{\sqrt{i^2 + j^2}} \sqrt{\frac{\varepsilon_d \varepsilon_m}{\varepsilon_d + \varepsilon_m}} \qquad (3)$$

and

10

152

$$\lambda_{RA} \cong \frac{P}{\sqrt{i^2+j^2}} \sqrt{\varepsilon_d} \tag{4}$$

where P represents the array pitch, ε_m and ε_d are the dielectric constants of the metal film (in this case TiO_2) and dielectric layer, respectively, and i and j are integers representing the diffraction orders. These dispersion relations approximate the resonance wavelength position in the transmission spectrum of the devices which can be altered by modifying the pitch of the rectangular array of nanoapertures. The dispersion relation is also strongly dependent on the dielectric constants, ε_m and ε_d. Due to the presence of interface asymmetries (glass/plasmonic and plasmonic/TiO_2), resonant peaks arising from both interfaces are observed in the measured spectra. The resonant localized surface plasmon mode of the apertures are also present in the spectra. Stalzer et al. [49] modelled an array of cross-shaped nanoapertures as a waveguide and calculated the TE and TM modes for different arm length-to-width ratios using the two-dimensional scalar Helmholtz equation. Based on their model, the cut-off frequency for the main TE mode (which is situated within the spectral range studied here) is expressed as:

$$\lambda_{res} = \frac{L^2}{0.7(L-W)} \sqrt{\varepsilon_d} \tag{5}$$

where L and W are the arm length and width respectively. Using this relation, the cut-off frequency for the nanoaperture array used in this study is expected to occur at around 463 nm. It is worth noting that the peak P_1 occurs close to this cut-off at around 477 nm. Therefore, we conclude that this peak likely corresponds to one of the LSP modes of the nanoaperture array. All main SPP and RA modes occur at longer wavelengths and therefore do not to interfere with this LSP mode. The P_3 peak corresponds to the SPP (1,0) Ag/TiO_2 mode and is located at ~594 nm and ~717 nm for the TE and TM polarizations respectively. For the TE polarization mode,

this peak is well defined, whereas it broadens significantly for the TM polarization due to the overlap with the SPP (1,0) Ag/glass mode. The peak P_2 occurs at 543 nm for the TE polarization and corresponds to the RA (1,0) mode, whereas the peak at 557 nm for the TM polarization is a result of the overlap of two SPP modes (1,1) Ag/TiO$_2$ and (1,1) Ag/glass. There are also some smaller satellite peaks associated with higher orders of SPPs and RAs visible within the measured spectrum. From the dispersion equations the main SPP modes have the most significant impact on the transmission spectrum of the plasmonic devices. **Figure 5** shows the variation in transmission intensity for P_1, P_2, and P_3 as a function of Ga ion implantation dose.
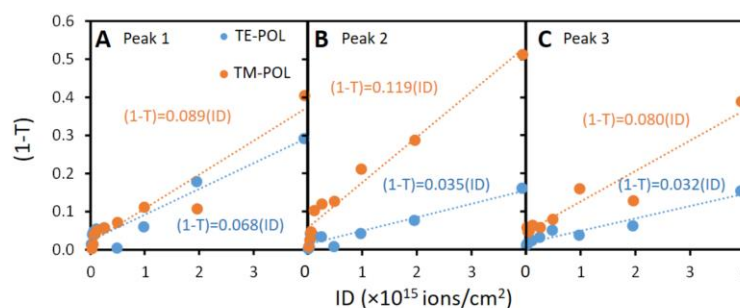
Figure 5. Relative change in the absorption (1-T) compared to D0, where T is the normalised transmission, of **(A)** Peak 1 (P_1), **(B)** Peak 2 (P_2) and **(C)** Peak 3 (P_3) as a function of ion deposition fluence (ID) at both TE and TM incident polarisations.

Consistent with both the luminescence (**Figure 2**) and normalized transmission intensity (**Figure 3**), the plasmon resonance transmission peaks (**Figure 5**) clearly decrease in height (corresponding to an increase in optical absorption) as a function of Ga ion implantation. This is due to the dependence of the plasmon resonance modes on the local dielectric function of the ion implanted TiO$_2$ (see Equations 3 to 5). As expected, the biggest change occurs at the TM polarisation (associated with the 400 nm array periodicity) for P_3 (SPP (1,0) Ag/TiO$_2$ mode). Based on the spectral data the sensitivity of the plasmonic devices to Ga ion implantation in TiO$_2$ is: $0.141 \pm 0.041 \times 10^{15}$ ions/cm^2, i.e. based on the standard deviation of the TM-POL data from **Figure 5**B the spectral output could be used to detect differences in the ion deposition

12

fluence of down to 4.1×10^{13} ions/cm^2. This is comparable, for example, to the levels of Ga ion implantation characterised in bulk diamond using ellipsometry[20].

In order to interpret the optical and spectral data in terms of the dielectric properties of the implanted TiO$_2$ regions, it is important to understand the mechanisms that induce changes in the local dielectric constant during the ion implantation process. Ion implantation is usually defined by two main parameters: dose (amount of implanted dopant per unit area) and implantation energy (responsible for the final depth of the dopant in the substrate). There are two primary stopping mechanisms when the ions enter the target material; the first one is the interaction of the implanted ions with the target ions (nuclear stopping), which results in a deflection of the incident ions and dislodging of the target ions. The second one is the interaction of the incident ions with the target's free and bound electrons (electronic stopping). Nuclear stopping causes physical damage and produces defects within the host lattice; electronic stopping results in vacancy-interstitials being formed. The number of displacements per target atom per unit time is described by the Kinchin-Pease relation [50,51]:

$$P(x) = \frac{0.8}{2nE_d} \left(\frac{dE}{dx}\right)_n \Phi \tag{6}$$

where Φ is the incident ion flux, n is the number density of the implanted ions, E_d is effective threshold displacement energy and $\left(\frac{dE}{dx}\right)_n$ is ion energy per unit depth. It is important to note that replacement reduces the number of vacancies that remain after the collisions by the recoil atoms. The total distance travelled by an ion before stopping is called the ion range (or ion implantation depth) and is determined by:

$$R = \int_0^R dx = \frac{1}{N} \int_0^{E_0} \frac{dE}{S_n(E) + S_e(E)} \tag{7}$$

13

Where E_0 is the initial energy of the ion (determined by the acceleration voltage), and S_n and S_e are the nuclear and electronic stopping power respectively. In the current study, the total displacement and range of the ions in the target lattice (TiO$_2$) is calculated by using the stopping and range of ions in matter (SRIM) Monte-Carlo simulation software [50,51].

The values in Table 1 were used as input parameters for the SRIM simulations along with the ion energy in *keV*. Several factors play a role in determining the effect of implanted ions on target atoms. Both the incident ion and target ion mass play an essential role in the energy transfer process. Ga ions have almost 90% of the TiO$_2$ ion mass and therefore every time a Ga ion hits the TiO$_2$ surface, it will transfer a portion of its energy to the target atoms. This means that after each collision the Ga ion has a high probability of creating a vacancy in the lattice. However, there is also a chance for the target atoms to recoil and to cause a much larger number of vacancies to form than those created by the ion collisions. **Figure 6** shows the collision plots produced from the SRIM Monte Carlo simulations of Ga ion implantation in TiO$_2$.
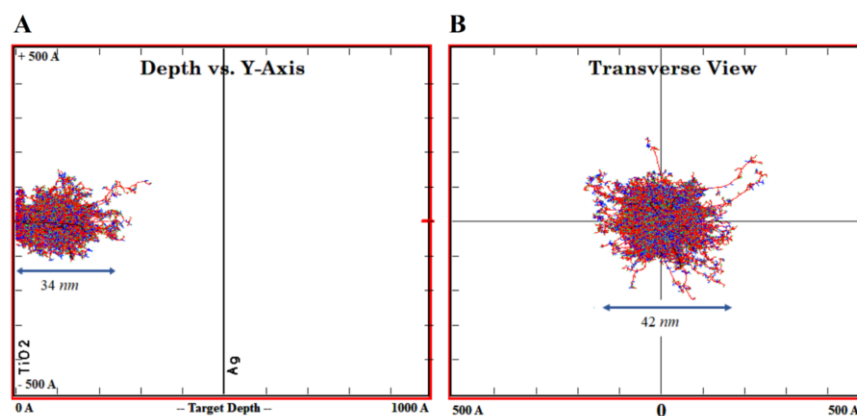
Figure 6. Still frames taken from animated collision plots generated using SRIM Monte Carlo simulations of Ga ion implantation in TiO$_2$. The longitudinal (A) and lateral (B) projection of the ion distributions (black cascades) and recoiling atoms (blue and red cascades) and vacancies (light blue and green dots) are shown.

14

156

The implantation depth of 16 keV Ga ions into TiO$_2$ is approximately 34 nm (**Figure 6**A), which is within the detectable range of the evanescent field of the plasmons and less than the overall film thickness. **Figure 6**B shows the transverse implantation spread has an approximate diameter of 42 nm. If we assume that the implantation volume can be approximated as a sphere this equates to a `cluster volume` of 3×10^{-17} cm^3. In the current experiment, each Ga ion transferred 14.7 keV (initial energy = 16 keV) to the target atoms: 9.2 keV to the Ti atoms and 5.5 keV to the O atoms. Since the energy transferred from the Ga ions to the Ti and O atoms is substantially less than their corresponding displacement energy (25 and 28 keV for Ti and O respectively) the Ga ions have a much higher probability of creating intersititials. Any energy transferred to the lattice is then likely to be converted to phonons. In the current study, the monovalent Ga-doped TiO$_2$ film was doped using a relatively low concentration of Ga ions and thereby the induced lattice charges were compensated for by Ti and Ga interstitials (Ga$^+$ or Ti^{4+}).

Table 2 shows the relative contribution of impurity ions within the implanted cluster at the end of each implantation process. A super-cell lattice is considered ($xGa[TiO_2]$) and it is assumed that x relates to the number of interstitials (Ga$^+$ and holes/vacancies). As a valid approximation, based on the energy loss, it is also assumed that during the implantation process only the incorporation of Ga$^+$ (the ion substitution in Ti^{4+}) took place with no formation of a new compound.

15

157

Table 2. TiO$_2$ contribution and impurity within the cluster based on SRIM calculations.

Implantation area	Number of impurity atoms × 10^2 [atoms/cluster] [a]	Contribution from impurity atoms within a cluster [%]
D0	0	0
D1	2	0.007
D2	4	0.013
D3	6	0.020
D4	10	0.033
D5	26	0.100
D6	50	0.167
D7	100	0.333
D8	200	0.667
D9	400	1.333

[a]This was determined as the product of the implanted defect density and the cluster volume which was assumed to be 3×10^{-17} cm^3 (see description in main text).

In our model we treat the Ga ions as spherical metal particles (with radius a) that are inclusions distributed within a homogeneous dielectric host (with radius h). While $0 \leq a \leq h/2$, ε_i and ε_h are taken to be the permittivity of the inclusion particle (Ga ion) and host medium (TiO$_2$) respectively. Typically, Lorentz molecular theory is not derived from the macroscopic form of Maxwell's equations, and therefore cannot directly be directly applied to the calculation of macroscopic quantities such as the permittivity of a composite. However, the closely related Maxwell-Garnett mixing formula considers both the electric and magnetic dipole moments as well as the volume fractions associated with individual contituents and therefore can be applied to the analysis of composites [52].

The specific volume per one Ga ion is: $v_{Ga} = \frac{V}{N}$, where V and the corresponding volume fraction of Ga ions is: $f = \frac{4\pi}{3}(a^3/v_{Ga})$. Therefore, the effective permittivity, $\varepsilon_{eff_{Ga}}$, of such composite is given by the Maxwell Garnet mixing formula [53]:

$$\varepsilon_{eff_{Ga}} = \varepsilon_h \frac{1+2f\frac{\varepsilon_i-\varepsilon_h}{\varepsilon_i+2\varepsilon_h}}{1-f\frac{\varepsilon_i-\varepsilon_h}{\varepsilon_i+2\varepsilon_h}} = \varepsilon_h \frac{\varepsilon_h+\frac{1+2f}{3}(\varepsilon_i-\varepsilon_h)}{\varepsilon_h+\frac{1-f}{3}(\varepsilon_i-\varepsilon_h)} \tag{8}$$

16

WILEY-VCH

here ε_{eff_G} is the effective permittivity of Ga ion in TiO$_2$, (note, $\varepsilon_{eff_{Ga}}$ is not the usual permittivity of a Ga ion in a vacuum [54]). The specific volume per particle is v, and the volume fraction of inclusions is f, also:

$$\varepsilon_h = \varepsilon'_{TiO_2} + \varepsilon''_{TiO_2} = (5.84 + 7.63 \times 10^{-8}\, i) \tag{9}$$

$$\varepsilon_i = \varepsilon'_{Ga} + \varepsilon''_{Ga} = (-12.53 + 34.10\, i) \tag{10}$$

Table 3 gives the volume fraction, the effective permittivity and the real and imaginary part of the implanted areas at λ = 578 nm (this value was chosen as it lies in between P$_2$ for TM-POL and P$_3$ for TE-POL) taking into the account the values of the relative composition presented in Table 2.

Table 3. Monte-carlo simulations of implanted TiO$_2$ based on the fraction of interstitials in each pattern. The volume fraction of inclusions corresponded to the SRIM simulated value.

Implantation area	Volume fraction of Ga ions × 10⁻³ (f)	Effective permittivity		Refractive index	
		$\varepsilon'_{eff_{Ga}}$	$\varepsilon''_{eff_{Ga}}$	$n_{eff_{Ga}}$	$k_{eff_{Ga}}$
D0	0	5.841	7.634 × 10⁻⁸	2.417	1.579 ×10⁻⁸
D1	0.121	5.844	0.001	2.417	0.00023
D2	0.241	5.846	0.002	2.418	0.00045
D3	0.362	5.848	0.003	2.418	0.00067
D4	0.724	5.854	0.007	2.420	0.00135
D5	1.568	5.869	0.014	2.423	0.00292
D6	3.016	5.895	0.027	2.428	0.00562
D7	6.032	5.949	0.055	2.439	0.01127
D8	12.064	6.058	0.111	2.461	0.02261
D9	24.127	6.278	0.228	2.506	0.04552

The optical constants summerised in Table 3 are shown as a function of both the relative change in the plasmon resonance peak absorption (P$_3$, TM-POL) and ion deposition fluence is shown

17

in **Figure 7**. Note that the linear fit in **Figure 5**B for TM-POL was used to convert from ID to

(1-T)
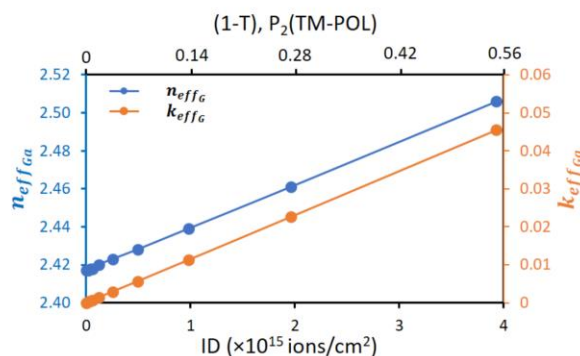
Figure 7. Optical constants $n_{eff_{Ga}}$ (blue line) and $k_{eff_{Ga}}$ (orange line) of the implanted TiO$_2$ plotted as a function of *either* (1-T) for P$_2$ at TM-POL (top *x*-axis) or as a function of the ion deposition fluence (bottom *x*-axis).

As the Ga ion deposition fluence increases, the real part of the refractive index ($n_{eff_{Ga}}$) changes from 5.841 for pure TiO$_2$ (D0) to 6.278 for TiO$_2$ Ga-doped with the highest dose (D9). Whereas the imaginary part of the refractive index ($k_{eff_{Ga}}$) changes from 7.634×10^{-8} for pure TiO$_2$ to 0.228 for TiO$_2$ Ga-doped with the highest dose. The real part of the effective permittivity is responsible for the lateral shift in the plasmon resonance peaks (~ 3 nm between D0 and D9 for P$_3$ at TM-POL). It is also primarily responsible for the small observed change in chromaticity as a function of implantation fluence (**Figure 2**). The change in the imaginary part of the refractive index, however, is responsible for absorption. Compared to the pristine TiO$_2$ the relative change in $k_{eff_{Ga}}$ is larger than that of $n_{eff_{Ga}}$. This is reflected in both the narrow range of chromaticity values observed on the optical brightfield images as well as the relatively small plasmon resonance peak shifts compared to the overall change in peak height and optical transmission.

18

WILEY-VCH

The relatively large change in plasmon resonance peak height as a function of implantation dose gives a simple and direct means of characterising the ion implantation density which could be applied to a wide range of different material systems. The analysis and equipment required to measure the optical output of bimodal plasmonic colour filters is comparatively straightforward and can be carried out using a standard brightfield microscope. By building up a reference database for different implanted ions, rapid, accurate measurement of ion implantation fluence could be carried out close to the sample preparation site providing rapid feedback to the user.

4. Conclusion

Direct optical detection of implanted TiO_2 thin films was demonstrated for the first time by using biomodal colour filters consisting of arrays of cross-shaped apertures in thin Ag films. The plasmon-mediated colour contrast and luminosity observed in the direct imaging of these structures was correlated to the Ga ion implantation dose. Furthermore, it was demonstrated that the plasmon resonance transmission could be varied by using aperiodic arrays of apertures and a polarized light source, where the highest contrast was achieved by using bigger array pitch (TM-POL).

By employing Monte-Carlo simulations and using the Maxwell Garnett mixing formula, we were able to determine the optical constants of the Ga ion implanted TiO_2 thin films and correlate this to the implantation fluence and plasmon resonance spectra. Our simulations showed that the implantation results in Ga ions mainly residing as interstitials within the TiO_2 matrix. This produces a small change in the real part of the refractive index for the composite material but leads to a substantial change in the imaginary part of the refractive index. The result is that coupling to the SPPs and LSPs within our plasmonic colour filter results in a significant and easily detectable change in the optical transmission as a function of Ga ion

19

WILEY-VCH

implantation fluence. This change in optical absorption is otherwise virtually undetecable using standard optical microscopy.

In conclusion, using direct optical imaging of the implanted material employing plasmonic nanostructures opens up new possibilities in the field of electronics where implantation is a routine technological process. Furthermore, it is possible to tune the plasmonic properties of individual biomodal plasmonic devices for the detection of a wide range of different implanted ions based on their dielectric properties.

References

[1]   Donda, K. D. & Hegde, R. S. Optimal design of beam-deflectors using extended unit-cell metagratings. *Progress In Electromagnetics Research* **77**, 83-92 (2019).

[2]   Xiong, K., Tordera, D., Jonsson, M. P. & Dahlin, A. B. Active control of plasmonic colors: emerging display technologies. *Reports on Progress in Physics* **82**, 024501 (2019).

[3]   Vashistha, V., Vaidya, G., Hegde, R. S., Serebryannikov, A. E., Bonod, N. & Krawczyk, M. All-dielectric metasurfaces based on cross-shaped resonators for color pixels with extended gamut. *ACS photonics* **4**, 1076-1082 (2017).

[4]   Balaur, E., Sadatnajafi, C., Kou, S. S., Lin, J. & Abbey, B. Continuously tunable, polarization controlled, colour palette produced from nanoscale plasmonic pixels. *Scientific reports* **6**, 28062 (2016).

20

WILEY-VCH

[5]   Balaur, E., Sadatnajafi, C., Langley, D. & Abbey, B. in *SPIE BioPhotonics Australasia.* 100132F (International Society for Optics and Photonics).

[6]   Langley, D. P., Balaur, E., Hwang, Y., Sadatnajafi, C. & Abbey, B. Optical chemical barcoding based on polarization controlled plasmonic nanopixels. *Advanced Functional Materials* **28**, 1704842 (2018).

[7]   Langley, D., Balaur, E., Sadatnajafi, C. & Abbey, B. in *SPIE BioPhotonics Australasia.* 1001338 (International Society for Optics and Photonics).

[8]   Choudhury, S. A. & Chowdhury, M. H. in *1st International Conference on Advanced Information and Communication Technology.*

[9]   Dasgupta, A., Singh, D., Tripathi, R. P. & Kumar, G. P. Directional Fluorescence Emission Mediated by Chemically-Prepared Plasmonic Nanowire Junctions. *The Journal of Physical Chemistry C* **120**, 17692-17698 (2016).

[10]   Barnes, W. L. Surface plasmon–polariton length scales: a route to sub-wavelength optics. *Journal of optics A: pure and applied optics* **8**, S87 (2006).

[11]   Zhang, K. & Rabin, O. Tailoring Localized Surface Plasmon Resonances in Metallic Nanoarcs for Surface Enhanced Infrared Absorption Spectroscopy. *Bulletin of the American Physical Society* (2019).

[12]   Hernandez-Lopez, J., Bauer, R., Chang, W.-S., Glasser, G., Grebel-Koehler, D., Klapper, M., Kreiter, M., Leclaire, J., Majoral, J.-P. & Mittler, S. Functional polymers as nanoscopic building blocks. *Materials Science and Engineering: C* **23**, 267-274 (2003).

[13]   Ni, G., Wang, L., Goldflam, M., Wagner, M., Fei, Z., McLeod, A., Liu, M., Keilmann, F., Özyilmaz, B. & Neto, A. C. Ultrafast optical switching of infrared plasmon polaritons in high-mobility graphene. *Nature Photonics* **10**, 244 (2016).

[14]   Wang, K., Schonbrun, E., Steinvurzel, P. & Crozier, K. B. Trapping and rotating nanoparticles using a plasmonic nano-tweezer with an integrated heat sink. *Nature communications* **2**, 469 (2011).

21

WILEY-VCH

[15]   Yoshioka, S. & Kinoshita, S. Direct determination of the refractive index of natural multilayer systems. *Physical Review E* **83**, 051917 (2011).

[16]   Tian, H., Luo, W., Pu, X., He, X., Qiu, P., Ding, A., Yang, S. & Mo, D. Determination of the optical properties of sol-gel-derived BaxSr1-xTiO3 thin film by spectroscopic ellipsometry. *Journal of Physics: Condensed Matter* **13**, 4065 (2001).

[17]   Rodrigues, M. S., Costa, D., Domingues, R., Apreutesei, M., Pedrosa, P., Martin, N., Correlo, V., Reis, R., Alves, E. & Barradas, N. Optimization of nanocomposite Au/TiO2 thin films towards LSPR optical-sensing. *Applied Surface Science* **438**, 74-83 (2018).

[18]   Larson, L. A., Williams, J. M. & Current, M. I. in *Reviews of Accelerator Science and Technology*   11-40.

[19]   Vollmer, D. P., Garber, J. D., Madani, K. R., Glass, G. A. & Walters, F. H. Electrochemical Impedance Spectroscopy of 3 MeV Nickel Implanted into Steel. *Analytical Letters* **30**, 359-366, doi:10.1080/00032719708002808 (1997).

[20]   Draganski, M. A., Finkman, E., Gibson, B. C., Fairchild, B. A., Ganesan, K., Nabatova-Gabain, N., Tomljenovic-Hanic, S., Greentree, A. D. & Prawer, S. Tailoring the optical constants of diamond by ion implantation. *Opt. Mater. Express* **2**, 644-649, doi:10.1364/OME.2.000644 (2012).

[21]   Polignano, M. L., Codegoni, D., Galbiati, A., Grasso, S., Mica, I., Basa, P., Pongracz, A., Kiss, Z. & Nadudvari, G. *Characterization Techniques for Ion-Implanted Layers in Silicon.* (2018).

[22]   Zhang, M., Lin, G., Dong, C. & Wen, L. Amorphous TiO2 films with high refractive index deposited by pulsed bias arc ion plating. *Surface and Coatings Technology* **201**, 7252-7258 (2007).

[23]   Nakayama, N. & Hayashi, T. Preparation and characterization of TiO2 and polymer nanocomposite films with high refractive index. *Journal of applied polymer science* **105**, 3662-3672 (2007).

WILEY-VCH

[24]   Jalil, S. A., Ahmed, Q. S., Akram, M., Abbas, N., Khalid, A., Khalil, A., Khalid, M. L., Mehar, M. M., Riaz, K. & Mehmood, M. Q. Fabrication of high refractive index TiO2 films using electron beam evaporator for all dielectric metasurfaces. *Materials Research Express* **5**, 016410 (2018).

[25]   Lester, S. D., Miller, J. N. & Roitman, D. B.   (Google Patents, 1998).

[26]   Yokogawa, S., Burgos, S. P. & Atwater, H. A. Plasmonic color filters for CMOS image sensor applications. *Nano letters* **12**, 4349-4354 (2012).

[27]   Li, Z., Clark, A. W. & Cooper, J. M. Dual color plasmonic pixels create a polarization controlled nano color palette. *ACS nano* **10**, 492-498 (2016).

[28]   Wang, D.-Y., Lin, H.-C. & Yen, C.-C. Influence of metal plasma ion implantation on photo-sensitivity of anatase TiO2 thin films. *Thin Solid Films* **515**, 1047-1052 (2006).

[29]   Fang, Y.-z., Kong, X.-j., Wang, D.-t., Cui, S.-x. & Liu, J.-h. Role of dopant Ga in tuning the band gap of rutile TiO2 from first principles. *Chinese Journal of Physics* **56**, 1370-1377 (2018).

[30]   Amraoui, R., Doghmane, M., Chettibi, S. & Laefer, D. The electronic structure and optical properties of rutile TiO2 co-doped with nickel and cerium. *Chinese journal of physics* **55**, 2393-2399 (2017).

[31]   Sell, D., Casey Jr, H. & Wecht, K. Concentration dependence of the refractive index for n‑ and p‑type GaAs between 1.2 and 1.8 eV. *Journal of Applied Physics* **45**, 2650-2657 (1974).

[32]   Kneipp, K. & Kneipp, H. Non‑resonant SERS Using the Hottest Hot Spots of Plasmonic Nanoaggregates. *Frontiers of Surface‑Enhanced Raman Scattering: Single Nanoparticles and Single Cells*, 19-35 (2014).

[33]   Liu, Z., Lee, H., Xiong, Y., Sun, C. & Zhang, X. Far-field optical hyperlens magnifying sub-diffraction-limited objects. *science* **315**, 1686-1686 (2007).

23

165

WILEY-VCH

[34]   West, P. R., Ishii, S., Naik, G. V., Emani, N. K., Shalaev, V. M. & Boltasseva, A. Searching for better plasmonic materials. *Laser & Photonics Reviews* **4**, 795-808 (2010).

[35]   Maier, S. A. Plasmonics: The promise of highly integrated optical devices. *IEEE Journal of selected topics in Quantum Electronics* **12**, 1671-1677 (2006).

[36]   Shalaev, V. M., Cai, W., Chettiar, U. K., Yuan, H.-K., Sarychev, A. K., Drachev, V. P. & Kildishev, A. V. Negative index of refraction in optical metamaterials. *Optics letters* **30**, 3356-3358 (2005).

[37]   Schmidt, S., Piglosiewicz, B. r., Sadiq, D., Shirdel, J., Lee, J. S., Vasa, P., Park, N., Kim, D.-S. & Lienau, C. Adiabatic nanofocusing on ultrasmooth single-crystalline gold tapers creates a 10-nm-sized light source with few-cycle time resolution. *ACS nano* **6**, 6040-6048 (2012).

[38]   Kliewer, K. & Fuchs, R. Collective electronic motion in a metallic slab. *Physical Review* **153**, 498 (1967).

[39]   Teng, Y.-Y. & Stern, E. A. Plasma radiation from metal grating surfaces. *Physical Review Letters* **19**, 511 (1967).

[40]   Lin, L., Goh, X. M., McGuinness, L. P. & Roberts, A. Plasmonic lenses formed by two-dimensional nanometric cross-shaped aperture arrays for Fresnel-region focusing. *Nano letters* **10**, 1936-1940 (2010).

[41]   Bouillard, J.-S., Einsle, J., Dickson, W., Rodrigo, S., Carretero-Palacios, S., Martin-Moreno, L., Garcia-Vidal, F. & Zayats, A. Optical transmission of periodic annular apertures in metal film on high-refractive index substrate: the role of the nanopillar shape. *Applied Physics Letters* **96**, 201101 (2010).

[42]   Chen, X., Huang, L., Mühlenbernd, H., Li, G., Bai, B., Tan, Q., Jin, G., Qiu, C.-W., Zhang, S. & Zentgraf, T. Dual-polarity plasmonic metalens for visible light. *Nature communications* **3**, 1198 (2012).

24

WILEY-VCH

[43]   Jiang, Y., Pillai, S. & Green, M. A. Re-evaluation of literature values of silver optical constants. *Optics express* **23**, 2133-2144 (2015).

[44]   Blinov, L. M., Kawai, T., Kozlovsky, M. V., Kawata, Y., Ichimura, K., Seki, T., Tripathy, S., Li, L., Oliveira Jr, O. & Irie, M. *Photoreactive organic thin films*. (Elsevier, 2002).

[45]   Kawata, S. Plasmonics: future outlook. *Japanese Journal of Applied Physics* **52**, 010001 (2012).

[46]   Genet, C. & Ebbesen, T. W. in *Nanoscience And Technology: A Collection of Reviews from Nature Journals*   205-212 (World Scientific, 2010).

[47]   Martin-Moreno, L., Garcia-Vidal, F., Lezec, H., Pellerin, K., Thio, T., Pendry, J. & Ebbesen, T. Theory of extraordinary optical transmission through subwavelength hole arrays. *Physical review letters* **86**, 1114 (2001).

[48]   Ghaemi, H., Thio, T., Grupp, D. e. a., Ebbesen, T. W. & Lezec, H. Surface plasmons enhance optical transmission through subwavelength holes. *Physical review B* **58**, 6779 (1998).

[49]   Stalzer, H., Greenman, M. & Willwerth, F. Modes of crossed rectangular waveguide. *IEEE Transactions on Antennas and Propagation* **24**, 220-223 (1976).

[50]   Sigmund, P. On the number of atoms displaced by implanted ions or energetic recoil atoms. *Applied Physics Letters* **14**, 114-117 (1969).

[51]   Myers, S. Ion-beam-induced migration and its effect on concentration profiles. *Nuclear Instruments and Methods* **168**, 265-274 (1980).

[52]   Koledintseva, M. Y., DuBroff, R. E. & Schwartz, R. W. Maxwell Garnett Model for Dielectric Mixtures Containing Conducting Particles at Optical Frequencies. (MISSOURI UNIV-ROLLA, 2006).

[53]   Markel, V. A. Introduction to the Maxwell Garnett approximation: tutorial. *JOSA A* **33**, 1244-1256 (2016).

WILEY-VCH

[54]   Hambleton, K., Hilsum, C. & Holeman, B. Determination of the effective ionic charge of gallium arsenide from direct measurements of the dielectric constant. *Proceedings of the Physical Society* **77**, 1147 (1961).

5.4 Summary

This chapter has shown how plasmonic colour filters can be used to experimentally determine the ion implantation dose and to characterise the optoelectronic properties of doped solid thin films. Maximum sensitivity was achieved by exploiting the bimodal characteristics of the device in combination with control over the incident polarisation. SRIM simulations were then used to help interpret the plasmon resonance spectra.

The use of plasmonic colour filters to detect changes in the local dielectric constant of implanted solid thin films provides a simple and direct means of characterising the local optoelectronic properties of these samples. This approach is expected to find a wide range of applications, particularly for ultra-thin layers where currently conventional optical imaging techniques struggle to measure the relevant material properties.

5.5 References

1.   Langley, D.P., et al., *Optical chemical barcoding based on polarization controlled plasmonic nanopixels.* Advanced Functional Materials, 2018. **28**(4): p. 1704842.

2.   Wang, D.-Y., H.-C. Lin, and C.-C. Yen, *Influence of metal plasma ion implantation on photo-sensitivity of anatase TiO2 thin films.* Thin Solid Films, 2006. **515**(3): p. 1047-1052.

3.   Fang, Y.-z., et al., *Role of dopant Ga in tuning the band gap of rutile TiO2 from first principles.* Chinese Journal of Physics, 2018. **56**(4): p. 1370-1377.

4.   Amraoui, R., et al., *The electronic structure and optical properties of rutile TiO2 co-doped with nickel and cerium.* Chinese journal of physics, 2017. **55**(6): p. 2393-2399.

5.   Kneipp, K. and H. Kneipp, *Non-resonant SERS Using the Hottest Hot Spots of Plasmonic Nanoaggregates.* Frontiers of Surface-Enhanced Raman Scattering: Single Nanoparticles and Single Cells, 2014: p. 19-35.

6.   Liu, Z., et al., *Far-field optical hyperlens magnifying sub-diffraction-limited objects.* science, 2007. **315**(5819): p. 1686-1686.

7.   West, P.R., et al., *Searching for better plasmonic materials.* Laser & Photonics Reviews, 2010. **4**(6): p. 795-808.

8.   Maier, S.A., *Plasmonics: The promise of highly integrated optical devices.* IEEE Journal of selected topics in Quantum Electronics, 2006. **12**(6): p. 1671-1677.

9.   Shalaev, V.M., et al., *Negative index of refraction in optical metamaterials.* Optics letters, 2005. **30**(24): p. 3356-3358.

10.   Schmidt, S., et al., *Adiabatic nanofocusing on ultrasmooth single-crystalline gold tapers creates a 10-nm-sized light source with few-cycle time resolution.* ACS nano, 2012. **6**(7): p. 6040-6048.

11.   Kliewer, K. and R. Fuchs, *Collective electronic motion in a metallic slab.* Physical Review, 1967. **153**(2): p. 498.

12.   Teng, Y.-Y. and E.A. Stern, *Plasma radiation from metal grating surfaces.* Physical Review Letters, 1967. **19**(9): p. 511.

13.   Lin, L., et al., *Plasmonic lenses formed by two-dimensional nanometric cross-shaped aperture arrays for Fresnel-region focusing.* Nano letters, 2010. **10**(5): p. 1936-1940.

14.   Bouillard, J.-S., et al., *Optical transmission of periodic annular apertures in metal film on high-refractive index substrate: the role of the nanopillar shape.* Applied Physics Letters, 2010. **96**(20): p. 201101.

15.   Chen, X., et al., *Dual-polarity plasmonic metalens for visible light.* Nature communications, 2012. **3**: p. 1198.

16.   Jiang, Y., S. Pillai, and M.A. Green, *Re-evaluation of literature values of silver optical constants.* Optics express, 2015. **23**(3): p. 2133-2144.

17.   Blinov, L.M., et al., *Photoreactive organic thin films*. 2002: Elsevier.

18.   Kawata, S., *Plasmonics: future outlook.* Japanese Journal of Applied Physics, 2012. **52**(1R): p. 010001.

19.   Genet, C. and T.W. Ebbesen, *Light in tiny holes*, in *Nanoscience And Technology: A Collection of Reviews from Nature Journals*. 2010, World Scientific. p. 205-212.

20.   Martin-Moreno, L., et al., *Theory of extraordinary optical transmission through subwavelength hole arrays.* Physical review letters, 2001. **86**(6): p. 1114.

21.   Myers, S., *Ion-beam-induced migration and its effect on concentration profiles.* Nuclear Instruments and Methods, 1980. **168**(1-3): p. 265-274.

22.   Sigmund, P., *On the number of atoms displaced by implanted ions or energetic recoil atoms.* Applied Physics Letters, 1969. **14**(3): p. 114-117.

CHAPTER 6

CHEMICAL AND MOLECULAR SENSING VIA POLARIZATION CONTROLLED PLASMONIC DEVICES

6   INTRODUCTION

Periodic subwavelength metallic apertures have the ability to passively detect variations in the dielectric properties of the local sample environment through modification of the plasmon resonances associated with these structures. For plasmonic colour filters this change manifests as an alteration of the measured transmission spectra collected using an incident white light source. The resulting peak structure can effectively provide a 'fingerprint' indicative of the dielectric properties of the medium within the near-surface region of these devices. For example, the shift in measured transmission peak positions can be used to quantify variations in the local refractive index via the dispersion relation. Some of the advantages of using plasmonic colour filters in the context of chemical or molecular sensing include the ability for these devices to be miniaturised permitting the use of very small sample volumes. In addition these plasmonic devices can be manufactured to deliver extremely high sensitivity and rapid response times making them ideally suited to sensing dynamic changes in the local chemistry or for real-time molecular detection [1-3].

In this chapter we explore the use of silver-based plasmonic colour filters for both chemical and molecular sensing. Firstly, by exploring the optical output of these devices as a function of the incident polarisation for a range of different analytes of known refractive index (RI), we are able to both maximise and quantify their sensitivity. We are able to show that through a simple colour change we can detect small changes in RI simply 'by eye'. We then extend this work to the real-time monitoring of the formation of self-

assembled monolayers (SAMs) based on detection of the optical output using a spectrometer. This latter application is much more challenging and highlights the potential for these devices to be able to dynamically monitor variations in the local environment down to the level of single molecules.

6.1 Chemical sensing based on plasmonic nanopixel arrays

In previous chapters it was demonstrated that through the introduction of asymmetries into the device structure/design it is possible to exploit variations in the incident polarisation to selectively modify the device output. In particular, periodic arrays of cross-shaped apertures were used to achieve a fine control over the resulting plasmon resonance modes that are excited within the devices and hence the measured transmission spectrum. Here, this property of aperiodic plasmonic colour filters is explored in the context of enhanced chemical sensing.

6.1.1 Chemical sensing using asymmetric periodic plasmonic arrays

A number of previous studies have investigated the sensitivity of EOT-based devices to changes in the local dielectric constant, via monitoring of the plasmon resonance peaks, which in turn give rise to the characteristic transmission intensity associated with these structures [4, 5]. Typically, these investigations have utilised periodic structures which were insensitive to changes in the polarisation vector of the incident light. Here, we examine how the introduction of aperiodicity, and hence polarisation sensitivity, enhances the ability of plasmonic colour filters to detect changes in the near-field refractive index. One interesting property of aperiodic plasmonic colour filters is that the degree of polarisation sensitivity is wavelength dependant. Whilst at most wavelengths some kind of change, which often involves a wholesale modification of the optical output, is detected.

There are particular special wavelengths where the measured transmission intensity is entirely insensitive to the incident polarisation vector. We classify these points in the transmission spectrum as 'isosbestic points'. Figure 6.1a shows a typical transmission spectrum recorded using a linearly polarised light incident upon an aperiodic array of cross-shaped apertures in a silver film. There are two distinct periodicities associated with this nanoaperture array, 300 and 450 nm, in the *X* and *Y* directions respectively.
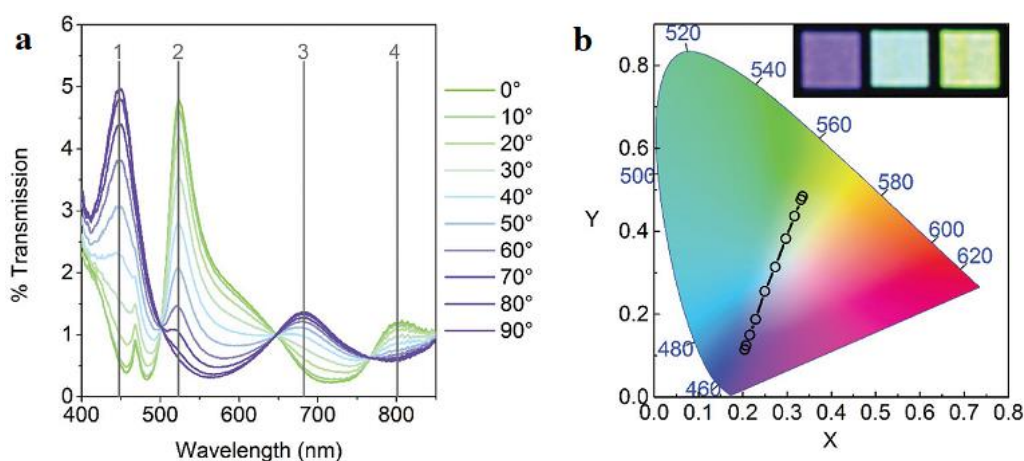
Figure 6.1 a) Transmission spectra recorded at 10° increments of the incident polarization angle. The four main peaks associated with the primary SPP modes are indicated by the vertical lines. b) CIE 1931 chromaticity diagram illustrating the observed output colour of the device for the ten polarization angles used in (a). In the top right corner are example optical images corresponding to the 0°, 45°, and 90° polarisation angles [6].

Whilst varying the incident polarisation between 0° and 90° four main transmission peaks were observed, these can be assigned to the (1,0) and (1,1) Ag/glass and Ag/air SPP modes respectively. The presence and location of the isosbestic points is also readily observed in the spectra. Figure 6.1b illustrates the CIE 1931 colour map for the optical output corresponding to each of the ten polarisation angles respectively, with the inset showing example optical images taken at 0°, 45° and 90°. It is clear that the choice of incident

polarisation vector has a profound effect on the optical output of these devices. As discussed in Chapter 3, a linear transition in the colour palette is observed as a function of the polarisation angle [7].

To be able to test the sensitivity of these devices to changes in the local RI due to the introduction of different analytes, the devices were incorporated into a microfluidic device as shown in Figure 6.2. Using this microfluidic setup, real-time monitoring of RI changes due to analyte change could be performed via either measurement of the transmission spectra using a spectrometer or as a direct colour change 'by eye'. A list of the analytes and their associated RIs used in this study are summarised in Table 6.1. The results obtained for the corresponding transmission spectrum for each of the different analytes tested are summarised in section 6.1.2.
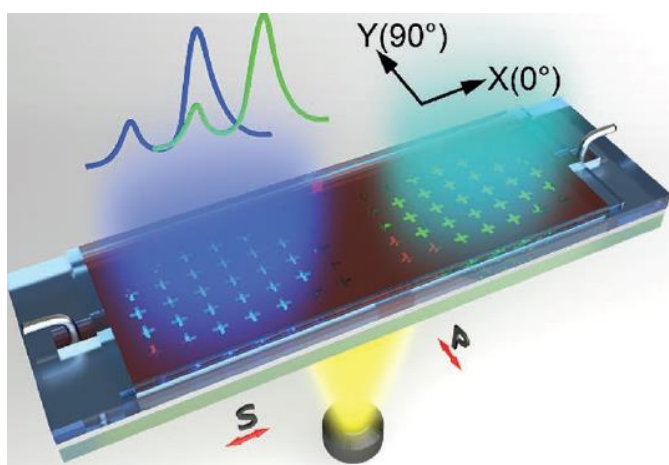
Figure 6.2 Schematic of microfluidic device used for chemical sensing measurement based on polarisation sensitive plasmonic colour filters. Details of the fabrication are provided in ref[6].

Analyte	Air	Water	0.1 M DMSO	0.1 M Sucrose	1M DMSO	1M Sucrose	DMSO
RI	1.0003	1.3332	1.3341	1.3379	1.3421	1.3607	1.4707

Table 6.1 *List of analytes and their associated refractive indices used in this study.*

6.1.2 Results from chemical sensing measurements

Figure 6.3 shows the transmission spectra for each of the 7 different chemicals measured for two different incident polarization angles (0° and 90°). As the RI of the analyte increases a redshift in the optical output is observed with the largest shift occurring for DMSO (RI=1.4707). The spectra reveal that even when the RI varies by less than 0.1% a measurable change in the optical output occurs. However, the spectral variation is more pronounced when the incident polarisation is set at 0°, defined here as being when the polarisation vector is aligned with the 450 nm pitch. A summary of the results showing the shift in wavelength of the main resonance peak and (for 90° polarisation) the secondary resonance peak as a function of the change in RI, corresponding to the data shown in Figure 6.3 is presented in Figure 6.4. The RI sensitivity of the optical output at both 0° and 90° incident polarisation defined as, Δλ/ΔRI, is also shown.
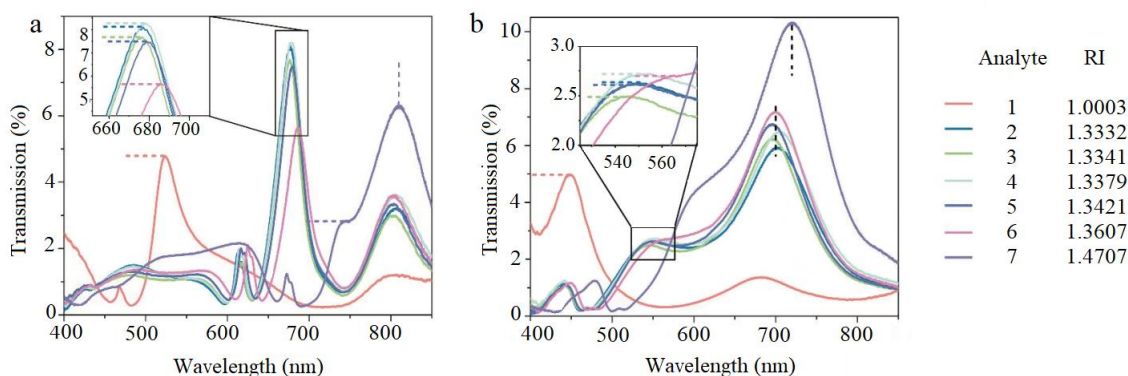
Figure 6.3 *Transmission spectra measured in air and seven analytes (see Table 6.1). The main resonance peaks are, associated with the Ag/Analyte and Ag/Glass interface SPP modes (indicated by the horizontal and vertical dashed lines) at a) 0° and b) 90° polarization.*
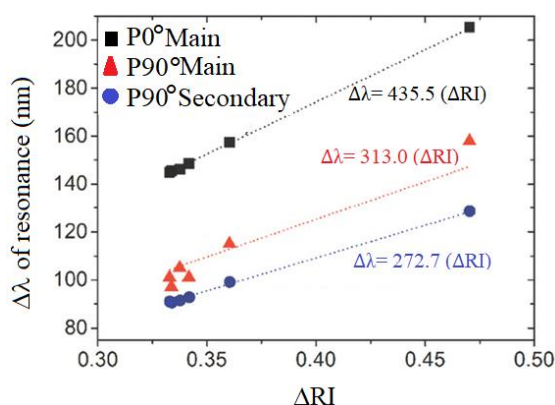
Figure 6.4 *Relative wavelength shifts of the Ag/A peaks as a function of RI for 0° and 90° polarizations. The dotted lines represent linear fits to the data (the equations are displayed on the graph).*

As suggested by a qualitative assessment of the relative spectral variation, the sensitivity is considerably higher for the $0°$ polarization angle (435.5 nm/RIU) compared to the $90°$ polarization angle (313 nm/RIU). This difference can be understood by considering the dispersion relation:

$$\Delta\lambda_{SPP} \cong \frac{P}{\sqrt{i^2+j^2}}\left(\sqrt{\frac{\varepsilon_d^1\varepsilon_m}{\varepsilon_d^1+\varepsilon_m}} - \sqrt{\frac{\varepsilon_d^2\varepsilon_m}{\varepsilon_d^2+\varepsilon_m}}\right) \qquad (6.1)$$

177

From Eq. 6.1 it can be seen that the effect of increasing the periodic spacing between apertures induces a larger shift in the wavelength of the plasmon resonance peak for a given change in RI. In addition, based on findings in the literature, the sensitivity of the devices is expected to be larger for the main SPP resonance modes compared to the secondary modes. Here the difference is 313 nm/RIU for the primary versus 272.7 nm/RIU for the secondary mode.

6.1.3 Chemical Sensing Based on Optical Colour Variation

In section 6.1.2 a spectrometer was used to detect minute changes in the RI of analytes via measurement of the position of the primary plasmon resonance peak. Here, we explore how the change in transmission spectrum with wavelength translates to an optical colour change that can be detected 'by eye'. Figure 6.5 presents the optical output corresponding to each of the spectra collected at both 0° and 90° incident polarisation shown in Figure 6.3 for the seven analytes. In addition, the results for 45°, corresponding to a linear combination of the output from the 0° and 90° polarisations is also shown.

Of particular note is the fact that a distinct colour change can be observed 'by eye' in the device output for changes in RI > 0.05. As indicated by the relative shift in wavelength position for the main resonance peak (Figure 6.4) the colour change is most pronounced for the 0° polarization angle. The colour palette in the optical output is observed to change from bright green through pink, indigo and chartreuse as the RI increases. As implied by the dispersion relation, the relative shift in the main plasmon resonance peak position is a function of the array pitch size – which is also reflected in the magnitude of the colour change for the 0° compared to 90° incident polarisation angle. Even though the sensitivity is reduced, one advantage of using an illumination with a 90° incident polarisation, is that the device will have a larger dynamic range in terms of

detectable RI. Further, in cases where the colour change with RI is quite subtle, the use of optical filters can render the changes more obvious to the naked eye. This is also illustrated in Figure 6.5 where the blue channel (which showed the highest sensitivity to changes in RI) is shown.
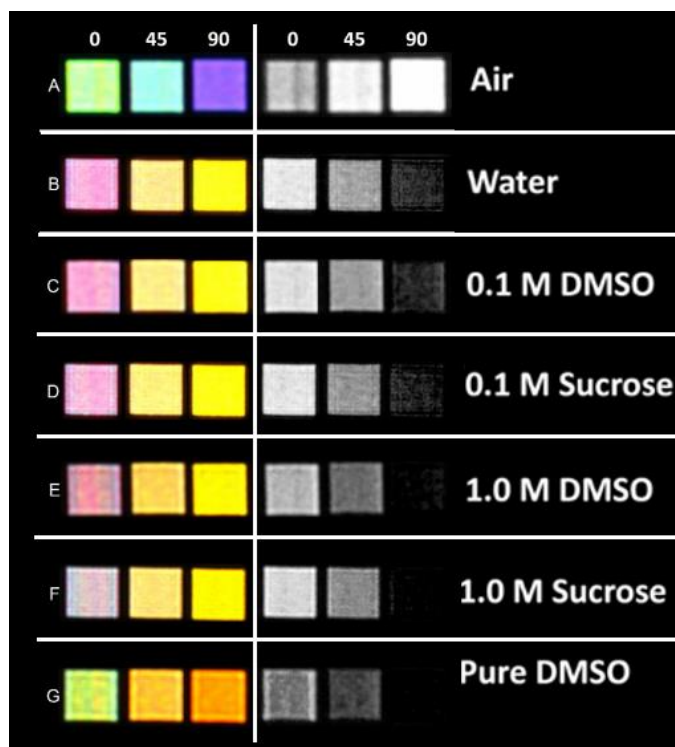
Figure 6.5 *Left: Full spectrum colour palette recorded for all seven analytes at 0°, 45° and 90° incident polarization angles. Right: corresponding greyscale images showing the blue colour channel only. All images have been captured under identical conditions with only the polarisation angle and analyte being varied.*

6.1.4 Use of isosbestic points to characterise local refractive index

Following the use of the measured transmission spectrum (section 6.1.2) and optical output detected 'by eye' (section 6.1.3) to characterise changes in the local RI, we next explore the potential to use the isosbestic points in the spectrum for chemical 'barcoding'. As discussed previously, the transmission spectra consist of a set of primary and secondary SPP modes associated with two interfaces (Ag/A and Ag/glass), as well as Wood anomalies. The modes associated with the Ag/A interface tend to be the most sensitive to changes in the local RI of the analyte. Whereas, the Ag/glass modes typically remain unchanged. As the RI of the analyte increases, the modes associated with the Ag/A interface

tend to overlap with the Ag/glass ones, making the tracking of the position of these modes difficult and in many cases impossible [1, 8]. This effect is clearly observed in Figure 6.3b, where the position of the main SPP modes are not readily detectable. The same issue also impacted the ability to use the output colour alone as a way of detecting changes in the analyte RI. To increase sensitivity to RI changes and eliminate the need to track the resonance peak positions, we developed a new approach to analysing the optical output of these devices based on tracking the isosbestic points in the transmission spectrum. Based on a qualitative assessment of the spectral data collected for the seven different analytes tested, the changes in both the position and intensity of the isosbestic points appear extremely sensitive to any variation in the local RI.

The transmission, $T(\theta)$, at a given point on the output spectrum and for an arbitrary polarisation angle can be described as a linear combination of the transmitted light contributions taken at 0° and 90° incident polarisation,

$$T(\theta) = T(0)\cos^2\theta + T(90)sin^2\theta \tag{6.2}$$

where θ is the incident polarization angle. The corresponding intensity of the electric field, $E(\theta)$, associated with the transmitted light must obey the following relationship

$$|E(\theta)|^2 = |E(0°)|^2 \cos^2\theta + |E(90°)|^2 \sin^2\theta \tag{6.3}$$

At particular values of the isosbestic point wavelengths both $T(\theta)$ and $|E(\theta)|^2$ will exhibit a special property that they are independent of the incident polarisation. To illustrate these features in the experimental data, Figure 6.6 presents the transmission spectra taken in air as well in all six analytes recorded at 10° increments of the polarization angle. The position of the isosbestic points are marked by vertical lines in each plot.
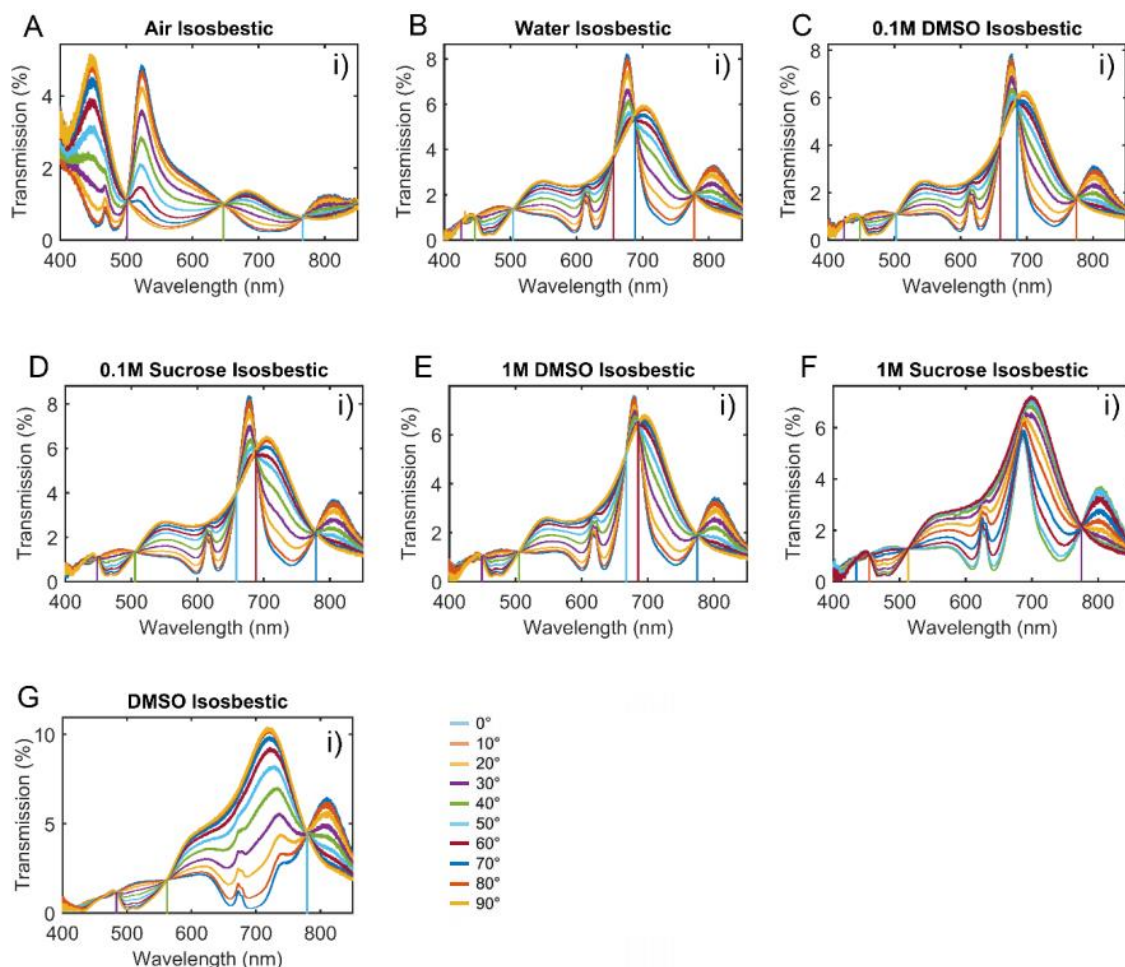
Figure 6.6 *Spectra for a) air, b) water, c) 0.1 M DMSO, d) 0.1 M sucrose, e) 1 M DMSO, f) 1 M sucrose, and g) DMSO collected at 10° increments of the incident polarisation. The isosbestic points are indicated by the vertical lines.*

Figure 6.6 shows that there is a clear variation in the isosbestic point position, number and intensity depending on the specific RI of the analyte investigated. By extracting the quantitative values for the isosbestic points for different analytes therefore, we have a means of uniquely 'barcoding' them which appears to be more accurate than either monitoring the peak resonance shift or looking at the colour output by eye. The three variables that were used to identify specific chemicals were the position, intensity, and

overall number of isosbestic points recorded in the spectrum. A summary of the isosbestic

point data for air and the six different analytes studied is presented in Figure 6.7.
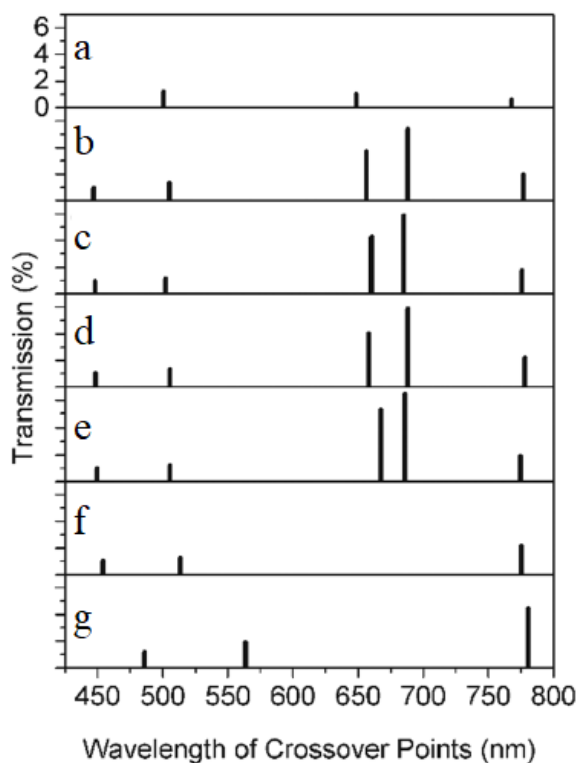
Figure 6.7 Isosbestic barcodes for a) Air, b) Water, c) 0.1M DMSO, d) 0.1M Sucrose, e) 1M DMSO, f) 1M Sucrose and g) DMSO. Note that the vertical axis scale for b-g is identical to a.

We note that although the wavelength of some of the isosbestic points are close (though still comfortably within our ability to resolve them), the overall combination of the intensity, wavelength position, and number of points provide a robust characteristic fingerprint for each analyte. In summary, comparing the three different approaches: resonant peak position, colour output, and isosbestic points, we find based on this data that the isosbestic points provide the most sensitive means of detecting changes in the local RI.

6.2 Molecular detection using bimodal plasmonic arrays

In section 6.1 the application of aperiodic plasmonic colour filters was explored in the context of chemical sensing. Here, we extend these ideas to investigate the formation of

self-assembled monolayers (SAMs) from solution, again using biomodal arrays of nanoapertures fabricated in silver films.

6.2.1 Plasmonic devices for molecular sensing

The structure and fabrication of the plasmonic devices used for the detection of SAM formation was similar to those used for chemical sensing. However, there was an additional issue when using these devices for molecular sensing due to the degradation of silver in the ethanolic solutions used to deliver SAMs to the surface of the plasmonic device [9]. Specifically, selective oxidation of ethanol by the silver films leads to the formation of silver aggregates and recrystalization [10, 11]. Since the surface of the device needed to both protect the active silver film and provide a facile surface for the molecules to attach to. Gold was selected as a suitable capping layer both to prevent the ethanol solution reaching the silver and to provide a surface that the organic molecules could attach to. Whilst gold is both chemically inert and can be easily deposited, it's performance within the optical regime for plasmonic sensing devices is less superior to silver. Hence, a thin 7 nm layer of gold was chosen to enable the formation of a continuous capping layer free from pores or defects, whilst only having minimal impact on the performance of the silver plasmonic devices. We note that 7nm is much less than the typical skin depth of these devices in ethanol which is $\sim$ 100 nm at λ=550 nm [12, 13], allowing for a substantial sensing volume to be maintained above the device surface. In order to test the stability of the plasmonic devices in ethanol, with and without a 7nm gold protective layer, freshly prepared devices were immersed in ethanol and their transmission spectra periodically measured (Figure 6.8).
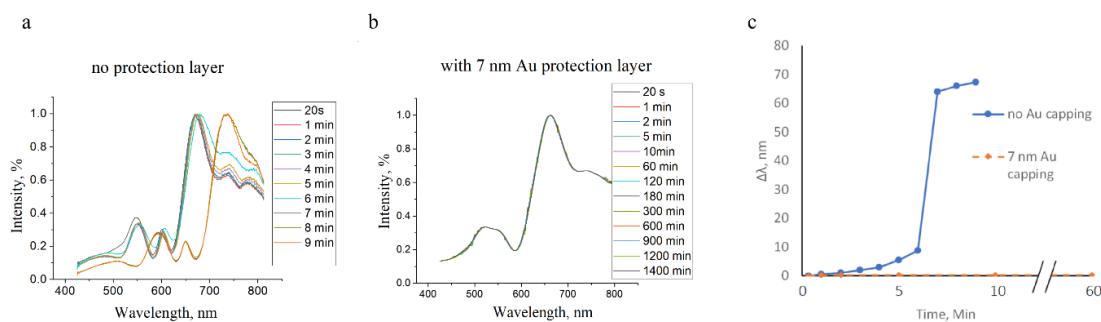
Figure 6.8 *Transmission spectra of: a) a bare device with no protective capping layer and*

b) a device covered with a 7 nm Au film immersed in ethanol solution. c) The corresponding

shift in the main plasmon resonance peak. Note that at 7 mins there is a large jump in the

main transmission peak position for the unprotected device and hence the measurements

were halted for the bare plasmonic after 10 mins. For the device protected by 7nm Au

(orange markers) the shift in plasmon resonance peak position was found to be < 0.5 nm

after 60 min. Note that the devices were also left in ethanol overnight for a total of 24 hrs

and then re-measured and, even then, no peak shifts greater than 0.5 nm were observed.

For the unprotected plasmonic device, a significant redshift of >60 nm occurs after 7 mins

exposure to ethanol, this confirms the expected degradation of Ag which happens very

rapidly due to oxidation of the surface. Given that the formation of a single SAM layer will

only induce a relatively small shift in the resonance peak position, it is clear that the bare

plasmonic is unsuitable for conducting these experiments. By contrast, just 7nm of gold,

deposited on top of the devices was found to lead to a dramatic improvement in the

resistance of the plasmonic device to degradation in ethanol. Even after leaving the devices

in ethanol for 24 hours there was less than a 0.5 nm shift recorded for the primary resonance

peak which is at the limit of detection for the spectrometer.

Although a 7 nm gold capping layer was found to provide sufficient protection in the preliminary ethanol trials, this was increased to 10 nm for the final plasmonic devices used for the SAM measurements to provide a small margin for error in case of any variations or inconsistences in the fabrication. Figure 6.9 compares the results for the same plasmonic device before and after capping with 10 nm of gold. As expected, the gold layer only has a minimal influence on the main plasmon resonance peak resulting in a shift of 4nm. This shift occurs partially due to the fact that Au itself exhibits plasmonic modes in the visible range [14].
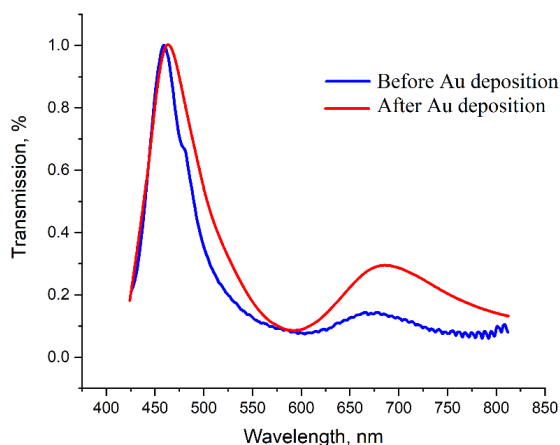
Figure 6.9 Normalised transmission spectra of a plasmonic device before and after capping with 10 nm of gold.

6.2.2 Physical characteristics of SAMs

Having established a reliable means for fabricating plasmonic devices for molecular sensing, a set of model SAMs against which to benchmark these devices needed to be established. A summary of the optoelectronic properties of the three SAMs studied that were studied is presented in Table 6.2.

SAM name	1-Hexa-decanethiol (HDT)	1-Octa-decanethiol (ODT)	16-Mercaptohexadecanoic acid (16-MHDA)
Molecular formula	$C_{16}H_{33}SH$	$C_{18}H_{37}SH$	$C_{16}H_{32}O_2S$
# of carbon atoms	C16	C18)	C16
Refractive index (n)	1.462	1.483	1.765
Permittivity (ε_{SAM})	2.14	2.20	3.16
Chain Length (nm)	2.0	2.8	1.9
Skin depth (nm) @ λ=550 nm.	117	114	76

Table 6.2 *The refractive index, permittivity, chain length and skin depth associated with the SAMs used in this study. Values take from refs[15, 16], [17], and [18].*

The particular SAMs that were chosen for this study, 1-Hexa-decanethiol (HDT) and 1-Octa-decanethiol (ODT), contain different numbers of carbon atoms in the molecular chain, and yet have a very similar RI. By contrast HDT and 16-Mercaptohexadecanoic acid (16-MHDA) have the same number of carbon atoms but very different RI properties. Note that as discussed in chapter 2, the 'skin depth', δz, is defined as the distance over which the component of the electric field associated with the SPP wave decays to 1/e of its initial value. A value for the skin depth can be determined by considering the dielectric constant for the metal and SAM, ε_m and ε_{SAM} respectively assuming a quasi-infinite layer thickness:

$$\delta z = \frac{1}{k_0} \left| \frac{\varepsilon_m + \varepsilon_{SAM}}{\varepsilon_{SAM}^2} \right|^{\frac{1}{2}}. \tag{6.4}$$

Figure 6.10 presents the calculated skin depth across the whole visible spectra for a dielectric layer which is just air as well as for the three SAMs used in this study.
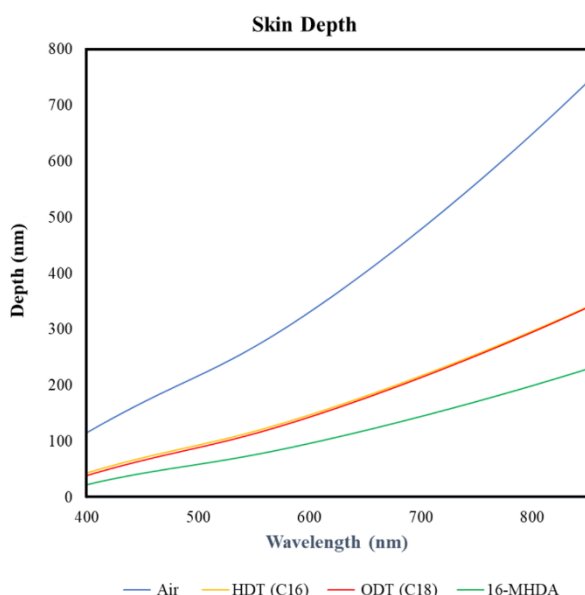
Figure 6.10 Skin depth calculated for air, HDT, ODT and 16-MHDA using Eq. 6.4.

Figure 6.10 shows that in terms of the skin depth, HDT and ODT, have a very similar trend in spite of their differences in terms of chain lengths. Whereas, the skin depth for 16-MHDA is quite different from HDT and ODT by virtue of its distinct RI properties despite having the same chain length. In the following section, theoretical predictions of the expected sensitivity in terms of detecting these SAMs are presented.

6.2.3 Theoretical calculation of the device sensitivity for SAM detection

Historically, detection of SAM formation via conventional SPR approaches has proven to be quite challenging. As the differences in the skin depth demonstrate, the decay of the electromagnetic wave associated with the SPPs can be highly dependant on the local RI. Figure 6.11 presents a schematic of the E_z component of the electric field arising from the

propagation of SPPs in three different media: air, a quasi-infinitely thick SAM, and (after formation) a SAM which is just one molecule thick.
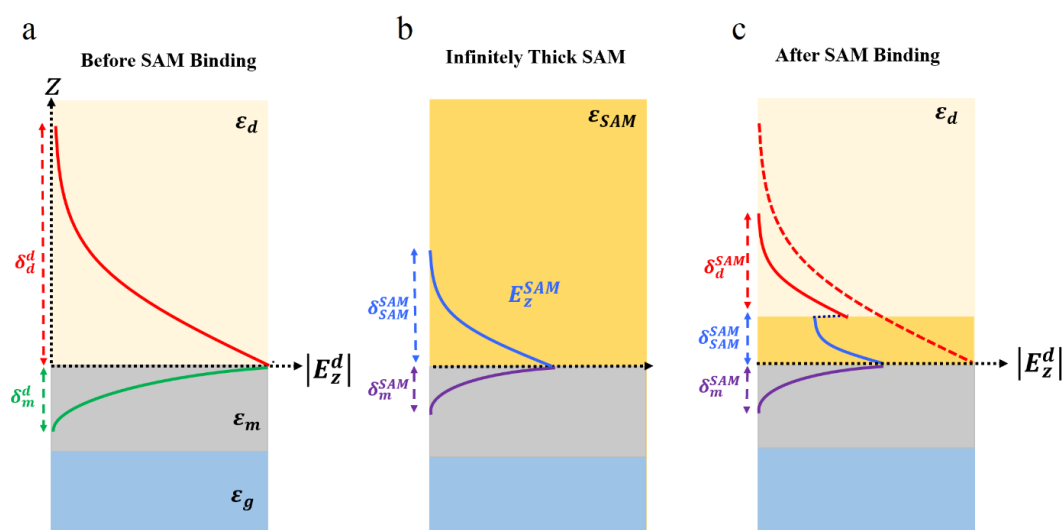
Figure 6.11 *Schematic of the decay of the E_z component associated with the SPP EM field for a) Free-space propagation, b) in a quasi-infinitely thick SAM and c) in a single SAM just one molecule thick. The dotted arrows the extent of the field in metal ($\boldsymbol{\delta_m^d}$ and $\boldsymbol{\delta_m^{SAM}}$), air($\boldsymbol{\delta_d^d}$ and $\boldsymbol{\delta_d^{SAM}}$), and in the SAM ($\boldsymbol{\delta_{SAM}^{dSAM}}$).*

The maximum skin depth for the plasmonic devices investigated here is ~ 295 nm at $\lambda=600$ when the SPP electromagnetic field is propagating in air (Figure 6.11a) [19]. However, as the permittivity increases the corresponding skin depth gradually decreases. In case of a single SAM layer, the exponential decay curve initially matches that of the quasi-infinitely thick SAM (Figure 6.11b). However, once the electric field extends beyond the single molecule layer, the rate of exponential decay instead matches that consistent with air (Figure 6.11c). This results in a discrete step-change in the decay rate at the upper SAM-air boundary.

For the majority of practical sensing applications, the wavelength (or angle) shift is recorded as a function of the change in the refractive index of the medium being investigated. As described in Chapter 2, the relationship between these parameters is known as the sensitivity factor and is given by:

$$S = \frac{\Delta\lambda}{\Delta RI} \tag{6.5}$$

This parameter gives an indication about the expected wavelength (or angle) shift as a function of the change in RI. Using Eq. 6.5 the expected sensitivity for three different device periodicities used for these measurements (350 nm, 400 nm, and 450 nm) was calculated and is summarised in Figure 6.12.
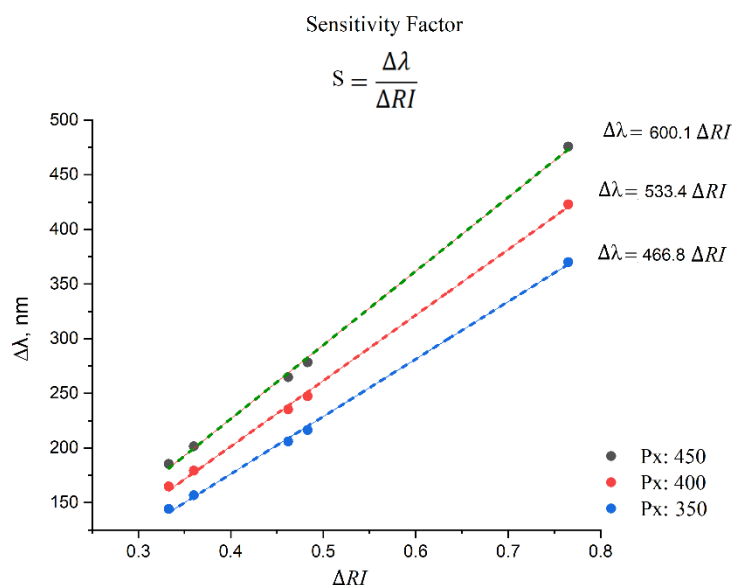
Figure 6.12 *The calculated sensitivity factor for the plasmonic devices used for SAM detection corresponding to three different pattern periodicities: 350, 400 and 450 nm.*

In the case of a finite SAM film with a thickness in the range of the skin depth, the SPR response, *R*, is given by:

189

$$R = S \left((n_{SAM} - n_d)[1 - \exp\left(\frac{-2t_{SAM}^{th}}{\delta z}\right)] \right) \tag{6.6}$$

Where n_{SAM} and n_d are the RI of the SAM and the dielectric medium immediately adjacent to the SAM respectively; t_{SAM} is the SAM thickness and δz is the skin depth in a quasi-infinite SAM. In the case of a highly-ordered monolayer, t_{SAM} is very similar to the thiol molecule length, therefore, the Eq, 6.6 can be used to estimate the theoretical expected resonant shift for a given SAM. Likewise, from the experimental evaluation of the resonant spectral shift, t_{SAM} can be calculated using the following derived relation based on Eq. 6.6:

$$t_{SAM}^{exp} = \left(\left(\frac{\delta_z}{2}\right)\left\{\frac{R_{exp}}{S[(n_{SAM}-n_d)]}\right\}\right) \tag{6.7}$$

By comparing the experimental to the theoretically predicted SAM film thickness it is thus possible to estimate the total SAM coverage using:

$$C = \frac{t_{SAM}^{exp}}{t_{SAM}^{th}} \times 100\% \tag{6.8}$$

Equations 6.6-6.8 were used to generate theoretical predictions against which to benchmark our experimental SAM data; the results are summarised in section 6.2.4.

6.2.4 SAM refractive index and coverage

Polarization-sensitive devices with cross-shaped patterns and periodicities P_x:450 and P_y:400 nm, protected with a 10 nm gold capping film were employed to study the formation of three SAMs discussed in section 6.2.2. A transmission spectrum was first collected in air prior to immersion in $1mM$ SAM (MHDA, HDT or ODT) ethanolic solutions for 24 hours. This amount of time in the SAM should be more than sufficient to form a complete layer. After immersion in the SAM, the sample was cleaned using pure ethanol followed by a wash in deionised water and finally was dried using N_2 gas. A comparison of the

measured transmission spectra before and after SAM deposition is shown in Figure 6.13

for both TE and TM incident polarisation modes.
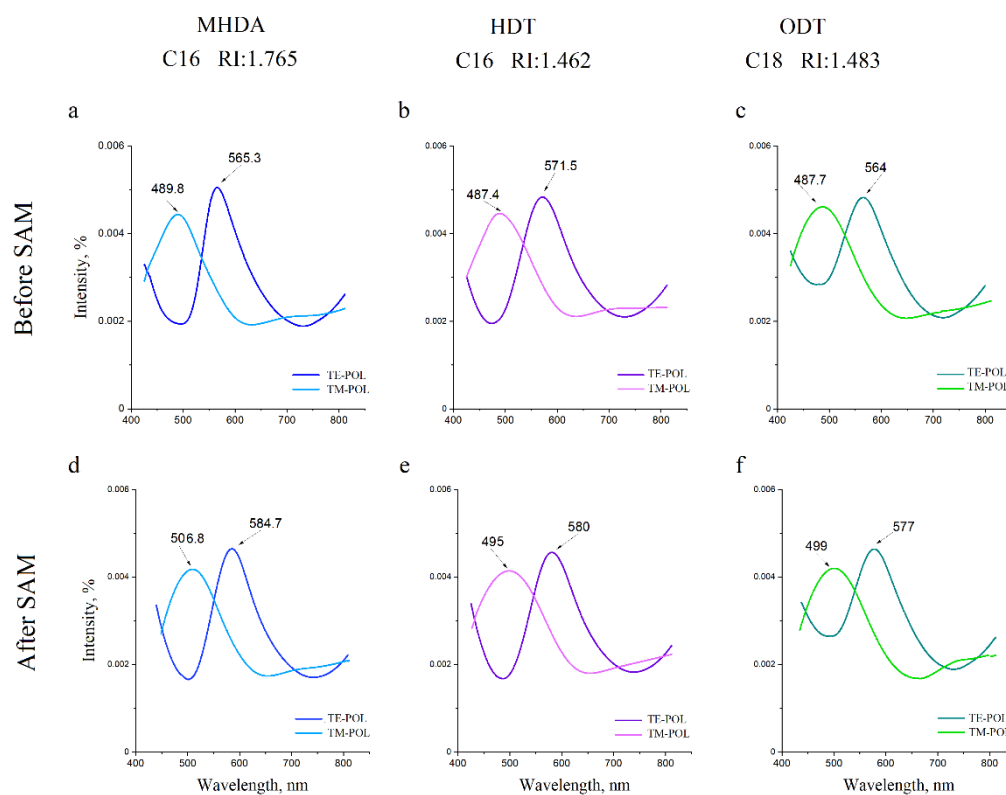
Figure 6.13 *Transmission spectra taken in air for three devices: (a, b and c) before and (d, e and f) after deposition of MHDA, HDT and ODT SAMs respectively.*

As expected, the spectra in Figure 6.13 reveal larger redshifts for the TE polarization mode, which is associated with the 450 nm periodicity. This effect was discussed earlier in the context of chemical sensing (see section 6.1.2). In addition, it is noted that the redshift is larger for SAMs with the same chain length, but different RI, compared to SAMs which have the same RI but different chain length SAMs. These results are entirely consistent with the predicted skin depth calculations (see Figure 6.10).

The red shift of the primary plasmon resonance peak provides a well-established means of tracking the formation of the SAM on the plasmonic device surface[20]. Using Eq. 6.7, the experimental SAM thickness can be determined from this peak shift. Once the SAM thickness, t_{SAM}^{exp} is extracted, the total SAM coverage within the measurement area can be estimated by using Eq. 6.8. A summary of the theoretically predicted and experimental results for the SPR response, as well as the experimental data for the SAM thickness and coverage is provided in Table 6.3.

SAM Type	# of C atoms	$R_{theoretical}$ (nm/RIU)		$R_{experimental}$ (nm/RIU)		t_{SAM}^{th} (nm)	t_{SAM}^{exp} (nm)		C_{SAM} (%)	
		TE	TM	TE	TM		TE	TM	TE	TM
MHDA	16	22.4	19.9	19.4	17	1.9	1.61	1.58	85%	83%
HDT	16	9.3	8.3	8.5	7.5	2.0	1.79	1.78	90%	90%
ODT	18	13.9	12.3	13	11.3	2.8	2.56	2.50	91%	90%

Table 6.3 *Theoretical and experimental comparison of the SPR response (Eq. 6.6.) and the SAM thickness (Eq. 6.7) as well as the coverage (Eq. 6.8) for TE and TM polarisation. Note that the theoretical SAM thickness, t_{SAM}^{th}, is given by the chain length (see Table 6.2).*

In general, long-chained SAMs (>18 C) such as ODT tend to form denser films [253]. This is supported by the experimental data based on the shift in the primary resonance peak position which shows a higher degree of coverage for the ODT then for the MHDA. The consistency in trends for R and the reasonable match between the theoretical and experimental values for R and for t_{SAM} provide significant confidence in the viability of

our plasmonic devices for detecting the adhesion of self-assembled monolayers. Having established that the shift of the primary resonance peak for our devices provides a means of detecting and characterising SAMs, we now explore whether optical barcoding based on the isosbestic points can be used to differentiate between the three different SAMs.

6.2.5 Using the isosbestic points for SAM detection

In section 6.2.6 we determined that the position of the resonance peak can be quantitatively analysed in order to extract the SAM thickness and coverage. Next, the goal was to explore how sensitive the isosbestic points are to deposition of the SAM, this is an extension of the work in using optical barcoding for chemical sensing presented in section 6.1.4. One key difference here, however, is that (unlike for chemical sensing) because the deposition of the SAM is an irreversible process a new plasmonic device needed to be fabricated for each of the three SAMs. The spectral data collected from the three plasmonic devices used for this study prior to deposition and following 24 hrs immersed in the SAM was presented in Figure 6.11. Whilst the data 'before SAM' spectra are very similar for the three devices, small changes in the conditions between the fabrication of the devices results in the primary resonance peak position changing by up to 6.2 nm. For this reason, the discussion here is focused on analysing the relative changes 'before SAM' and 'after SAM' for the three plasmonic devices, rather than comparing the absolute values for the optical barcodes between the different SAMs.

Figure 6.14 presents a summary of the position and intensities for the isosbestic points prior to SAM deposition (darker bars) and after 24 hours immersed in the SAM (lighter bars). In all but one case we note that the shift in position of the isosbestic point is

far greater than the differences in the absolute values for the isosbestic points between the

three different devices.
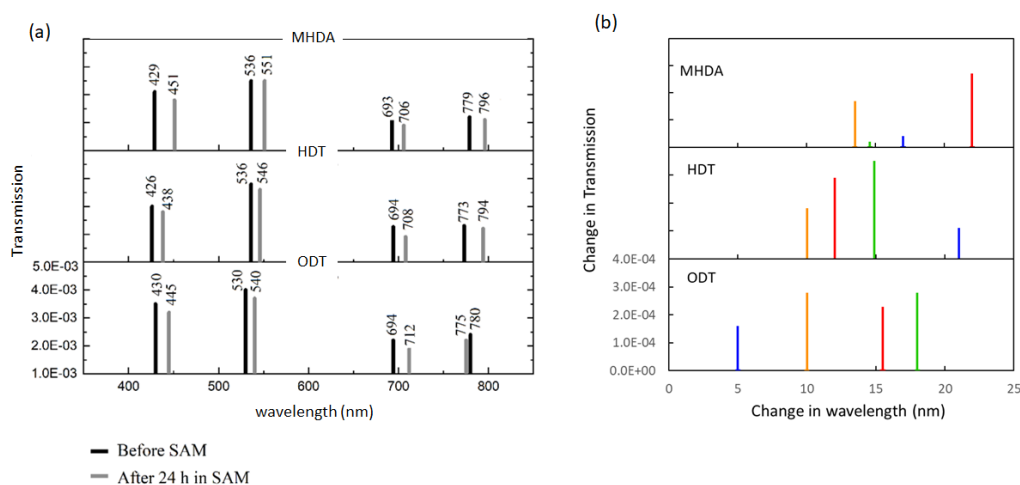
Figure 6.14 a) *A comparison of the 'before SAM' (vertical black lines) and 'after SAM' (vertical grey lines) and b) a summary of the change in position and transmission of isosbestic points for MHDA, HDT, and ODT.*

Figure 6.14a shows that there are four isosbestic points present in these spectra. Analysis of the data collected from the each of the three devices used to detect the presence of MHDA, HDT, and ODT reveals that relative to the initial spectra the isosbestic points undergo clear changes. Further, the relative change in both their position and intensity appears to be quite different for each of the three SAMs. Even taking into account the fact that small differences between the initial output of the devices could have an impact on the behaviour of the isosbestic points, the magnitude of the changes observed in these experiments indicate a clear distinction between the three different SAMs measured. For comparison the change in position of the main resonant peak positions measured in section 6.2.4 were $\Delta\lambda$ (TM/TE) = (17.0/19.4), (7.6/8.5), and (11.3/13.0) nm for MHDA, HDT, and ODT respectively. Hence, whilst the shift in resonant peak position enables a quantitative

interpretation of parameters such as the SAM coverage, the tracking of isosbestic points for molecular detection is extremely promising in terms of sensitivity and discrimination. In particular, with reliable and reproducible device fabrication measurement of the isosbestic points could enable specific molecules to be distinguished as they attach to the surface, without requiring any specific surface functionalisation.

6.2.6 Monitoring the progress of SAM formation

As a final stretch goal to detecting the presence and relative coverage of SAMs using plasmonic colour filters, experiments were performed that attempted to detect the very earliest stages of SAM formation during the first 60 mins that the devices were immersed in the ethanolic solution. The aim was to both try to determine whether it was possible to detect very low concentrations of SAM on the surface of the device, but also to attempt to characterise the SAM dynamics by monitoring the optical output of the devices. Experiments were carried out on HDT and MHDA as these two SAMs were revealed to have the largest differences in terms of their transmission spectra (section 6.2.4) due to their differing RIs.

To study the initial stages of SAM adhesion, the plasmonic devices were immersed in 1 mM ethanolic solution of MHDA and 1 mM HDT. At certain time points (10, 30, and 60 min) the samples were removed from the solution, washed in ethanol followed by deionised water and dried using N_2 gas prior to their transmission spectra being recorded. Once the optical data had been collected the samples were returned to the SAM solution and the measurement time restarted. Based on the published literature, the first 60 mins of adhesion for these SAMs is known to encompass a critical phase in their nucleation [21]. Figure 6.15 presents the spectral data collected for each of the two SAMs during these

measurements. A summary of the corresponding theoretically predicted and experimental results for the SPR response, as well as the experimental data for the SAM thickness and coverage is provided in Table 6.4.
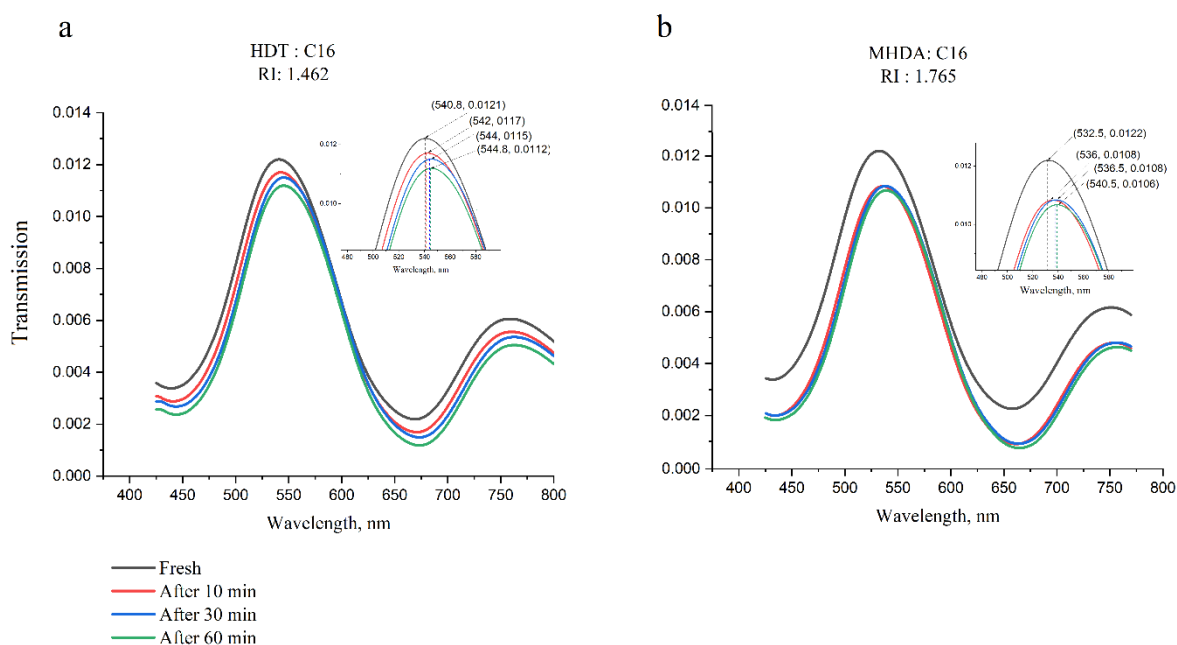
Figure 6.15 *Transmission spectra recorded in air before, and after 10, 30, and 60 mins immersion in a) HDT and b) MHDA ethanoic solutions.*

SAM	RI*	t_{SAM}^{th} (nm)	Time in SAM (min)			Time in SAM (min)		
			10	30	60	10	30	60
			t_{SAM}^{exp} (nm)			C_{SAM} (%)		
HDT	1.462	2.0	0.31	0.56	1.0	15.5	28.0	50.0
MHDA	1.765	1.9	0.34	0.38	0.7	17.9	20.0	36.8

* assuming $C_{SAM} = 100\%$

Table 6.4 *Theoretical and experimental comparison of SPR response (Eq. 6.6), SAM thickness (Eq. 6.7), and coverage (Eq. 6.8) for TE and TM polarisation. Note that the theoretical SAM thickness, $\bm{t_{SAM}^{th}}$, is given by the chain length (see Table 6.2).*

A qualitative assessment of the transmission spectra in Fig. 6.15 indicates that the initial formation behaviour of the two SAMs appears to be different during the first 60 mins. For example, based on this data, the HDT appears to show an immediate shift in the plasmon resonance peaks from the moment the devices are submerged in the SAM. By contrast, MHDA exhibits a large change after just 10 mins, but then shows very little variation in the optical output up to the 60 min mark. A potential explanation for this is that in spite of the fact that the two SAMs have the same head group and carbon chain length, their nucleation mechanisms may be different due to a different functional group (CH_3 vs COOH) being present [21]. Whilst the shift in plasmon resonance peak position indicates a consistent red-shift in line with expectations from spectra which were collected after 24 hrs immersion in the SAM solution, the magnitude of these changes (some of which are on the order of 0.5 – 1.0 nm) are close to the limit of detection. Hence, we next analysed the spectra in terms of their isosbestic points (e.g. similar to section 6.2.4) with the spectral analysis presented in Figure 6.16. (the dotted lines indicate the positions of the isosbestic points).
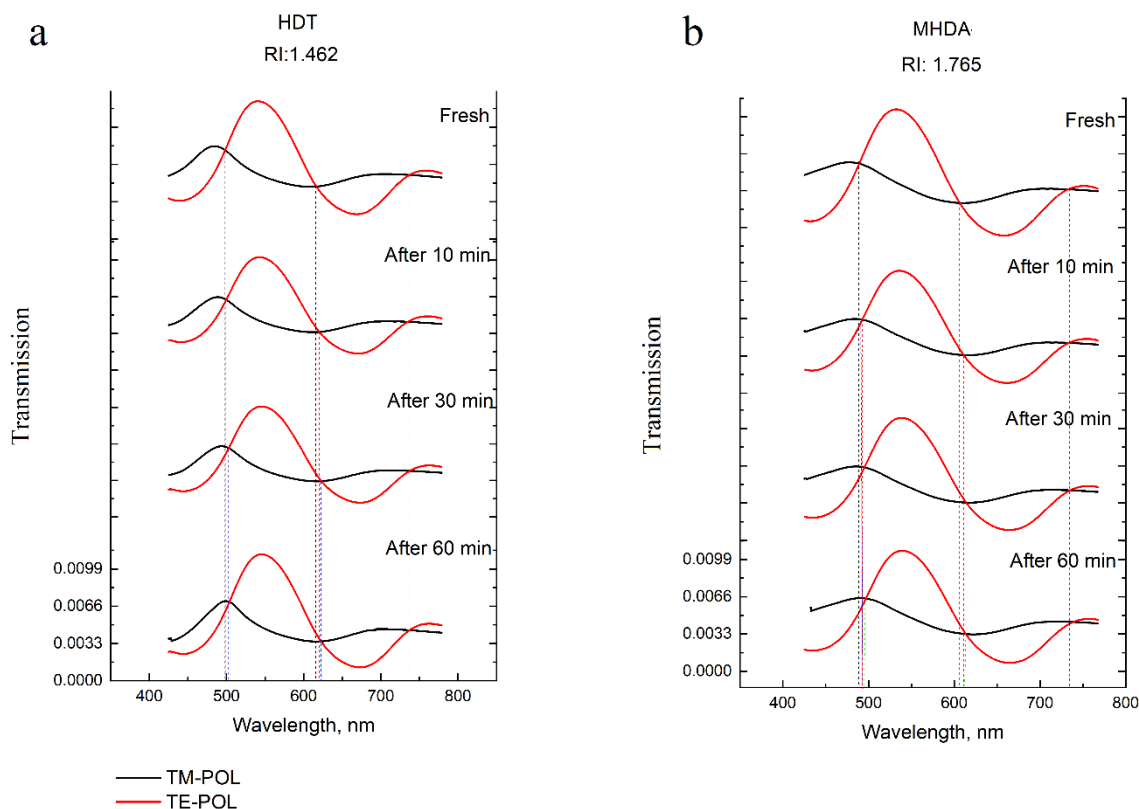
Figure 6.16 *Analysis of isosbestic points identified for a) HDT and b) MHDA at 10, 30, and 60 mins.*

The wavelength position and intensity of the isosbestic points corresponding to Figure 6.16 is summerised in Figure 6.17. Based on this analysis, it appears that even in cases where the shift in the main plasmon resonance peak between time points is < 1 nm, the resulting change in the isosbestic points, which make use of a larger spectral range, show a clear and distinct change. This preliminary data points to the fact that isosbestic points may be a useful means of tracking the progression of SAM formation and, more generally, molecular kinetics at the surface of plasmonic sensors provided a suitable control is established. It is important to note, however, that there are two key issues that remain to be solved before reliable spectral changes, at the level observed here, can be used to extract information regarding the molecular dynamics.

1) In order to be able to quantitatively compare the results between different SAMs, the repeatability, in terms of fabrication, of different devices needs to improve to the point that the resulting spectra are indistinguishable to the limit of resolution of the measurement.

2) The spectral measurements need to be made without moving or handling the sample. This is to avoid any potential issues with contamination or variability in output across the devices.

The first point can be addressed via a modification to the fabrication protocols utilising recent advances in lithography, this is discussed in a recent conference publication[22]. The second point could be addressed through a modification of the current microfluidics platform, where all of the washing and drying steps could be performed with the sample remaining *in-situ* without interfering with the spectral measurements.

Figure 6.17 *Comparison of the isosbestic barcodes for the HDT and MHDA SAMs corresponding to spectra collected after 10, 30, and 60 mins.*

6.3 Conclusion

Passive optical detection of variations in the dielectric properties of the local environment was demonstrated by using asymmetric periodic sub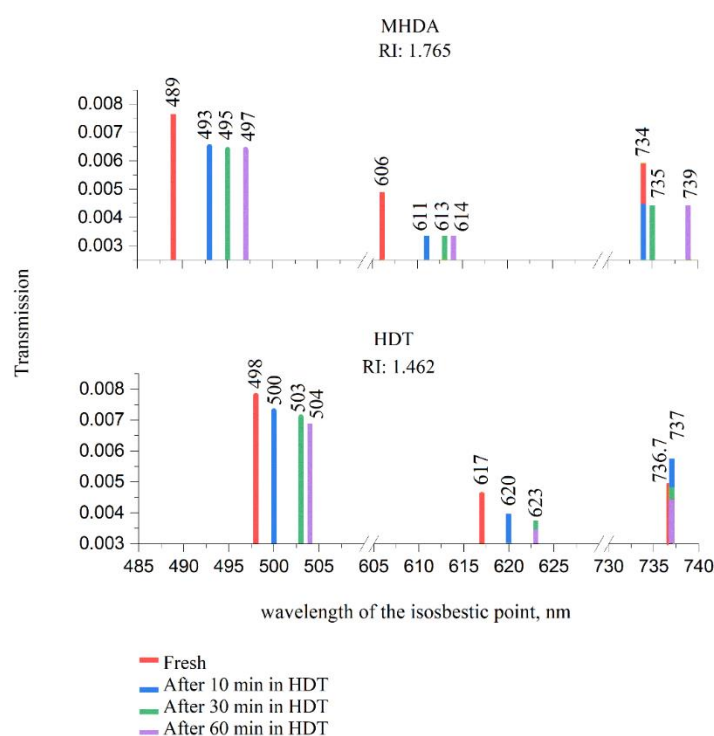wavelength metallic apertures fabricated in thin silver films. In terms of chemical sensing, by employing a microfluidic system, direct monitoring of the analyte RI was demonstrated using three different methods. The first method relied on using a spectrometer to monitor the resonant peak position in the transmission spectra, where the resulting resonance could be correlated to changes in the dielectric properties of the surrounding medium. It was found that whilst for some analytes (e.g. using TE polarization) this approach led to satisfactory results, for others this approach could lead to difficulties in interpretation because of the overlap and merging of different resonant modes. A second method used for direct detection of the analyte RI was to simply look at the colour change 'by eye' or under an optical microscope. It was found that a distinct colour change occurs for RI > 0.05 at the TE polarization. However, this approach also suffers from the same limitations in terms of ambiguity when resonance modes merge as discussed above. To overcome these limitations, a third approach was proposed and demonstrated, which takes into account the full spectrum. This method relies on analysis of the isosbestic points, which can be determined by using aperiodic arrays of apertures and by varying the incident polarisation vector. Based on the position and the intensity of these isosbestic points a 'barcode-like' signature can be established for each analyte.

In the second part of this chapter, polarization controlled dual pitch cross-shaped apertures were employed to monitor the formation of thiol SAMs. It was demonstrated that the position of the resonant peaks can be used not only to distinguish different types of SAMs, but also for a direct quantification of the SAM coverage. It was observed that the long-chained SAMs tended to form denser films, in line with the published literature[23].

Whilst this method gave satisfactory results following complete formation of the SAM, it was sometimes difficult to use it for the very earliest stages (i.e. < 60 mins) of SAM adhesion. To overcome this, the use of optical barcoding was once again explored in the context of molecular sensing. Whilst the results appear promising, future work will address issues around the consistency of device fabrication (enabling comparison of dynamics between different SAMs) and also around reliable measurement of very fine changes in the optical spectra.

6.4 References

1.   Baldelli, S., et al., *Surface enhanced sum frequency generation of carbon monoxide adsorbed on platinum nanoparticle arrays.* The Journal of Chemical Physics, 2000. **113**(13): p. 5432-5438.

2.   Becker, J., et al., *The optimal aspect ratio of gold nanorods for plasmonic bio-sensing.* Plasmonics, 2010. **5**(2): p. 161-167.

3.   Chen, H.-T., A.J. Taylor, and N. Yu, *A review of metasurfaces: physics and applications.* Reports on progress in physics, 2016. **79**(7): p. 076401.

4.   Roh, S., T. Chung, and B. Lee, *Overview of the characteristics of micro-and nano-structured surface plasmon resonance sensors.* Sensors, 2011. **11**(2): p. 1565-1588.

5.   Grande, M., et al., *Asymmetric plasmonic grating for optical sensing of thin layers of organic materials.* Sensors and Actuators B: Chemical, 2011. **160**(1): p. 1056-1062.

6.   Langley, D., et al. *Dual pitch plasmonic devices for polarization enhanced colour based sensing*. in *SPIE BioPhotonics Australasia*. 2016. International Society for Optics and Photonics.

7.   Balaur, E., et al., *Continuously tunable, polarization controlled, colour palette produced from nanoscale plasmonic pixels.* Scientific reports, 2016. **6**: p. 28062.

8.   Blaber, M., et al., *Plasmon absorption in nanospheres: A comparison of sodium, potassium, aluminium, silver and gold.* Physica B: Condensed Matter, 2007. **394**(2): p. 184-187.

9.   Knoben, W., S.H. Brongersma, and M. Crego-Calama, *Preparation and characterization of octadecanethiol self-assembled monolayers on indium arsenide (100).* The Journal of Physical Chemistry C, 2009. **113**(42): p. 18331-18340.

10.   Silbaugh, T.L., et al., *Selective oxidation of ethanol over Ag, Cu and Au nanoparticles supported on Li2O/γ-Al2O3.* Journal of Catalysis, 2018. **364**: p. 40-47.

11.   Sun, L., et al., *Ethanol-induced formation of silver nanoparticle aggregates for highly active SERS substrates and application in DNA detection.* The Journal of Physical Chemistry C, 2008. **112**(5): p. 1415-1422.

12.   Rodrigo, S.G., F.J. García-Vidal, and L. Martín-Moreno, *Influence of material properties on extraordinary optical transmission through hole arrays.* Physical Review B, 2008. **77**(7): p. 075401.

13.   Seo, M.A., et al., *Terahertz field enhancement by a metallic nano slit operating beyond the skin-depth limit.* Nature Photonics, 2009. **3**(3): p. 152-156.

14.   Sun, Y. and Y. Xia, *Gold and silver nanoparticles: a class of chromophores with colors tunable in the range from 400 to 750 nm.* Analyst, 2003. **128**(6): p. 686-691.

15.   Tam-Chang, S.-W., et al., *Self-assembled monolayers on gold generated from alkanethiols with the structure RNHCOCH2SH.* Langmuir, 1995. **11**(11): p. 4371-4382.

16.   Hong, K., et al., *Lower hole-injection barrier between pentacene and a 1-hexadecanethiol-modified gold substrate with a lowered work function.* Organic Electronics, 2008. **9**(1): p. 21-29.

17.   Ma, H., et al., *Electrochemical investigation of dynamic interfacial processes at 1-octadecanethiol-modified copper electrodes in halide-containing solutions.* Electrochimica acta, 2003. **48**(28): p. 4277-4289.

18.   Gupta, R.K., M. Srinivasan, and R. Dharmarajan, *Synthesis of 16-Mercaptohexadecanoic acid capped gold nanoparticles and their immobilization on a substrate.* Materials Letters, 2012. **67**(1): p. 315-319.

19.   Huidobro, P.A., et al., *Transformation optics for plasmonics.* Nano letters, 2010. **10**(6): p. 1985-1990.

20.   Perino, M., et al., *Development of a complete plasmonic grating-based sensor and its application for self-assembled monolayer detection.* Applied Optics, 2014. **53**(26): p. 5969-5976.

21.   Zhuang, J.-L., A. Terfort, and C. Wöll, *Formation of oriented and patterned films of metal–organic frameworks by liquid phase epitaxy: A review.* Coordination Chemistry Reviews, 2016. **307**: p. 391-424.

22.   Balaur, E., C. Sadatnajafi, and B. Abbey, *Large-Scale Fabrication of Optically Active Plasmonic Arrays via Displacement Talbot Lithography.* JPhCS, 2020. **1455**(1): p. 012005.

23.   Jacob, J.D.C., T.R. Lee, and S. Baldelli, *In situ vibrational study of the reductive desorption of alkanethiol monolayers on gold by sum frequency generation spectroscopy.* The Journal of Physical Chemistry C, 2014. **118**(50): p. 29126-29134.

CHAPTER 7

SUMMARY OF THESIS AND SUGGESTIONS FOR FUTURE WORK

7   INTRODUCTION

The key advantages of next generation metallic, nano-engineered metamaterials, over conventional optical components are based on their unique optoelectronic properties arising from induced plasmonic excitations [1-4]. These properties are due to the momentum coupling that occurs between incident photons and the mobile electrons at the interface between the nanopatterned metallic film and a dielectric medium [5]. Advances in nanofabrication techniques make it possible to tailor the optical response of plasmonic devices and enables their miniaturisation for a broad range of imaging and sensing applications [6-8].

7.1 Thesis Goals

The work presented in this thesis has investigated the interaction between light and metallic nanofabricated metamaterials. In particular, this study used cross-shaped nano apertures fabricated in silver thin films to create bimodal plasmonic colour filters which could be used for chemical and molecular sensing. The overarching goal of this thesis can be summarised as:

- The design and development of two-dimensional sub-wavelength periodic arrays of cross-shaped apertures in order to create plasmonic colour filters [9, 10].

- The investigation of diamond-like carbon as a novel protection layer to oxidation and degradation of the plasmonic devices [11].

- The application of bimodal plasmonic colour filters for direct optical imaging of ion implantation in thin films.

204

- The development of a novel optical chemical barcoding system to enable label-free RI sensing based on the optical output of bimodal plasmonic colour filters [12, 13].

- The study of SAM formation via analysis of the output of bimodal plasmonic arrays.

7.2 Outcomes of this work

- **Plasmonic colour filters**

In chapter 3, the influence of device geometry on the optical output of plasmonic colour filters was investigated. To better understand the influence on the optical response of the four key length scales (arm length, pitch, width and thickness) for these devices, different arrays of cross-shaped apertures were fabricated in thin silver films. First of all, it was observed that all structures exhibited two sets of plasmonic modes (one characteristic to the metal-substrate interface, and another to the metal-air interface) in their transmitted spectra. The influence of the substrate modes was noticeable in the output colour for the devices. It was observed that it is possible to tailor the impact of these modes primarily by changing the thickness of the metallic film. Furthermore, the pitch size was shown to have the greatest effect on the plasmon resonance modes; for example, increasing the pitch size resulted in a red-shift of the modes and a corresponding movement of the main plasmon resonance peak towards longer wavelengths. By changing the width of the aperture arms, the overall transmission intensity was varied, whilst the actual position of the resonant modes was mostly unchanged. Interestingly, by exploiting asymmetry in the aperture arrays and aperture arms, it was possible to produce polarization sensitive devices with a significantly expanded colour palette range. A continuous colour palette was achieved by fine tuning the periodicity of the arrays and the polarization of the incident light, whilst keeping the geometry of individual cross-shaped apertures constant. In addition, it was demonstrated that the same characteristics in terms of colour and polarisation sensitivity was maintained

even for very small array sizes (e.g. 4×4 or even 2×2 sets of apertures). To better understand the physics underlying these observations, the dispersion relations and FEM simulations were employed. It was demonstrated that the dispersion relations were able to predict the position of individual plasmonic modes, whilst FEM simulations could be used to recreate the overall shape of the transmission spectra.

- **DLC passivation**

In chapter 4 a novel solution for increasing the stability of the silver-based plasmonic devices was investigated. Deposition of an electron-beam induced Diamond-Like Carbon (DLC) film was demonstrated to be a convenient way to protect these devices from the effects of degradation and oxidative ageing. It was shown that a nanometre-thin conformal DLC layer was sufficient to protect silver-based plasmonic devices with negligible impact on the device performance. The oxidative aging effect was investigated under a range of different environmental conditions, including ambient conditions in air, under liquids, and also under highly corrosive conditions. It was demonstrated that the effectiveness of DLC to protect these devices depend on the DLC deposition conditions, with thicker films giving better protective performance.

- **Direct optical imaging of ion implantation in thin films**

In chapter 5, the application of the plasmonic nanopixel arrays to the direct optical detection of ion implantation was investigated. The aim was to probe local changes in the dielectric properties of a thin film of TiO_2 deposited on top of a bimodal plasmonic colour filter and doped with Ga+ ions. The observed colour and intensity contrast was related to the relative change of the refractive index of the implanted areas and plotted as a function of the ion implantation dose. Furthermore, it was demonstrated that the colour contrast could be varied by changing the polarization of the incident light. This was achieved by exploiting the asymmetric periodicity of the nanopixel array; the colour contrast having a direct

relationship to the pitch size. A higher contrast was observed for periodic arrays with effectively bigger pitch size. Monte-Carlo simulations and the Maxwell Garnett mixing formula were used to understand the effect of the ion implantation on the overall dielectric properties of the dopped TiO_2 films. The conclusion of this study was that Ga ions mainly reside as interstitials within the TiO_2 matrix after implantation. Therefore, ion implantation has only a small impact on the real part of the dielectric permittivity, and a higher impact on the imaginary part, experimentally demonstrated by a significantly higher optical absorption.

- **Chemical and molecular sensing**

In chapter 6, the use of silver-based plasmonic devices in context of chemical and molecular sensing was investigated. It was experimentally demonstrated that such devices are capable of detecting minute changes of RI of analytes. This was demonstrated by monitoring the plasmon resonance transmission spectra and the optical brightfield output, making the detection of RI by eye possible. By exploiting polarization sensitive arrays, a wider dynamic range was possible. Furthermore, a new approach to analysing and classifying spectral data from bimodal plasmonic arrays was demonstrated based on analysis of the spectral isosbestic points. The combination of three main characteristics of these points was used to generate a unique 'fingerprint' for different chemicals providing a greater degree of differentiation. Based on our qualitative assessment, the changes in both the position and intensity of the isosbestic points offers a novel method for analysing variation in the local RI of a wide range of different analytes.

The ability of the dual-pitched arrays to monitor SAM formation, was also investigated. A significant problem for SAM detection on silver plasmonic devices is the degradation of the surface due to immersion in ethanol; we were able to address this problem by adding a thin capping layer of Au. By measuring the SPR wavelength shift and

by employing the dispersion relation, it was possible to numerically determine the coverage and the thickness of the SAM. Because of their very small thickness (just a few nanometres), the sensitivity factor of plasmonic devices plays a crucial role in the investigation of the RI variations during SAM formation. To overcome this limitation, the optical barcoding method using the isosbestic points was employed and it was shown that this provided a clear differentiation between different SAM layers. The final stretch goal of this work was to attempt to characterise the dynamics of SAM formation and to also determine the ability of the plasmonic device to detect very low concentrations of SAM on the device surface. Although initial results were found to be promising, further data must be collected to verify these findings and will form part of future work.

7.3 Key contributions to knowledge originating from these studies

- Demonstrated the fabrication of bimodal, cross-shaped nano-aperture arrays and their sensitivity to a polarized light, which resulted in fine colour tuning in the optical range. Also, the interpretation of the key features in the optical transmission was performed by employing fundamental theoretical models (see chapter 3 [9, 10]).

- Optimised the stability of the silver based plasmonic colour filters with respect to oxidative aging and degradation by employing electron-beam induced DLC thin films (see chapter 4 [11]).

- Demonstrated the ability of the bimodal plasmonic colour filters for direct optical detection of ion implantation (see chapter 4).

- Demonstrated the ability of the bimodal plasmonic device to passively detect small variations in the local RI by incorporating the devices into a microfluidic system (see chapter 6.1 [12, 13]).

- Investigated the detection of small variations in SAM thickness and coverage of different SAMs using bimodal plasmonic device and the resulting isosbestic points determined from the plasmon resonance transmission spectra (see chapter 6.2).

7.4 Future work

Fabricating and optimising plasmonic nanoscale colour filters for biological sensing and molecular imaging requires additional development. Possible further work building on the outcomes of the current study can be classified in two sections: First, additional types of capping layers need to be explored, both to improve the overall performance but also to potentially functionalise the surface of the devices for greater specificity. Second, the incorporation of plasmonic devices into microfluidics for SAM detection should result in higher quality data and consequently even greater sensitivity.

Optimization of surface protection of plasmonic devices

Whilst thin layers of gold proved to be effective at protecting the silver plasmonic devices from the effective of oxidative aging, further improvements in the performance of the capping layer is still possible. For example, improved optical transmission and low electronic damping of the evanescent field generated by the plasmons within the silver nanofabricated layer may be possible by exploring different materials [14-16]. Further, in the context of molecular sensing, functionalisation of the surface layer should lead to a greater degree of specificity. For example, silane-based SAMs require oxide-based surfaces (such as silicon oxide, titanium oxide, etc.) to promote adhesion [17], whereas thiol-based SAMs work best with gold surfaces [18-20]. To promote adhesion, functionally tailored

surfaces, where specific layers are chosen based on their SAM-surface reaction properties need to be trialled. Future work will be focused on addressing these issues.

Enclosed microfluidic systems for real time molecular detection

Although microfluidic systems have shown promising results for chemical sensing[13], the reaction between the ethanol and PDMS (normally used for microfluidic fabrication) during SAM formation is still of a major concern. This is because this reaction leads to detachment of the PDMS from the substrate, substantially reducing the concentration of ethanolic solution during the measurement, and impacting the integrity of the microfluidic device. New approaches to microfluidic device fabrication are required to address this problem. This might involve designing systems that, for example, ameliorate the effects of chemical interaction between the PDMS and the substrate. Other transparent materials might also be considered that are less permeable to solvent solutions and still able to provide a superior adhesion to the substrate material. Furthermore, to avoid any errors during the plasmonic array fabrication for multiple analyte/SAM detection, high-quality, large area fabrication needs to be optimised further. In addition, dedicated microfluidic channels could be placed on the same substrate as the plasmonic sensor enabling accurate measurement of a control and analyte/SAM using the same sensor. Additionally, such enclosed systems would benefit from the fact that they provide a contamination-free environment that could be effectively cleaned by flushing the lines with e.g. ethanol, between measurements. A schematic showing the concept for such a setup is shown in Figure 7.1.
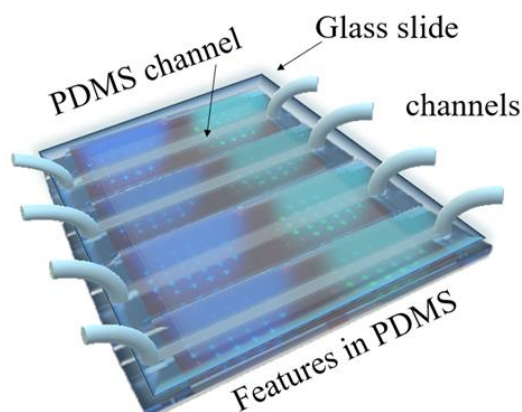
Figure 7.1 Schematic of a microfluidic device incorporating a plasmonic sensor with 8 inlets/outlets. The solutions and N_2 gas are introduced through the channel inlets. The inlets and outlets could be sealed during the measurement to prevent evaporation of the solution.

It would be straightforward that such systems could be used with either syringes or a peristaltic pump setup with automatic control of the input and output provided by using pneumatic or mechanic valves.

7.5 Summary

This thesis has explored the application of a range of plasmonic devices based on cross-shaped apertures in thin silver films. Plasmonic colour filters have been shown to provide high-accuracy and high dynamic range when asymmetries are introduced into the devices and the incident polarisation is exploited. When the output from bimodal plasmonic devices is analysed, features such as the isosbestic points can be exploited to provide even greater differentiation in terms of the sample refractive index. Achieving full colour transmission with polarisation control, even for nano-sized arrays, opens up a wide range of applications from local colour filtering to nanoscale sensing of localized changes in the sample refractive index.

7.6 References

1.   Kauranen, M. and A.V. Zayats, *Nonlinear plasmonics.* Nature photonics, 2012. **6**(11): p. 737.

2.   Luk'yanchuk, B., et al., *The Fano resonance in plasmonic nanostructures and metamaterials.* Nature materials, 2010. **9**(9): p. 707-715.

3.   Naik, G.V., V.M. Shalaev, and A. Boltasseva, *Alternative plasmonic materials: beyond gold and silver.* Advanced Materials, 2013. **25**(24): p. 3264-3294.

4.   Hess, O., et al., *Active nanoplasmonic metamaterials.* Nature materials, 2012. **11**(7): p. 573-584.

5.   Sreekanth, K.V., et al., *New Directions in Thin Film Nanophotonics.* Vol. 1. 2019: Springer.

6.   Zeng, S., et al., *Nanomaterials enhanced surface plasmon resonance for biological and chemical sensing applications.* Chemical Society Reviews, 2014. **43**(10): p. 3426-3452.

7.   Stewart, M.E., et al., *Nanostructured plasmonic sensors.* Chemical reviews, 2008. **108**(2): p. 494-521.

8.   Jakšić, Z., et al., *A consideration of the use of metamaterials for sensing applications: Field fluctuations and ultimate performance.* Journal of Optics A: Pure and Applied Optics, 2007. **9**(9): p. S377.

9.   Balaur, E., et al. *Optimisation of polarization controlled colour tuning using nanoscale cross-shaped apertures in silver films.* in *SPIE BioPhotonics Australasia.* 2016. International Society for Optics and Photonics.

10.   Balaur, E., et al., *Continuously tunable, polarization controlled, colour palette produced from nanoscale plasmonic pixels.* Scientific reports, 2016. **6**: p. 28062.

11.   Balaur, E., et al. *Electron-beam induced diamond-like-carbon passivation of plasmonic devices*. in *Micro+ Nano Materials, Devices, and Systems*. 2015. International Society for Optics and Photonics.

12.   Langley, D., et al. *Dual pitch plasmonic devices for polarization enhanced colour based sensing*. in *SPIE BioPhotonics Australasia*. 2016. International Society for Optics and Photonics.

13.   Langley, D.P., et al., *Optical chemical barcoding based on polarization controlled plasmonic nanopixels.* Advanced Functional Materials, 2018. **28**(4): p. 1704842.

14.   Im, H., et al., *Atomic layer deposition of dielectric overlayers for enhancing the optical properties and chemical stability of plasmonic nanoholes.* Acs Nano, 2010. **4**(2): p. 947-954.

15.   Rycenga, M., et al., *Controlling the synthesis and assembly of silver nanostructures for plasmonic applications.* Chemical reviews, 2011. **111**(6): p. 3669-3712.

16.   Larson, S., et al., *Dipole radiation-induced extraordinary optical transmission for silver nanorod-covered silver nanohole arrays.* The Journal of Physical Chemistry C, 2019. **123**(9): p. 5634-5641.

17.   Bogan, J., et al., *Nucleation and adhesion of ultra-thin copper films on amino-terminated self-assembled monolayers.* Applied Surface Science, 2018. **462**: p. 38-47.

18.   Liu, A., et al., *Gold nanostructures with near-infrared plasmonic resonance: Synthesis and surface functionalization.* Coordination Chemistry Reviews, 2017. **336**: p. 28-42.

19.   Chandekar, A., S.K. Sengupta, and J.E. Whitten, *Thermal stability of thiol and silane monolayers: A comparative study.* Applied Surface Science, 2010. **256**(9): p. 2742-2749.

20.   Rittikulsittichai, S., et al., *Bidentate aromatic thiols on gold: new insight regarding the influence of branching on the structure, packing, wetting, and stability of self-assembled monolayers on gold surfaces.* Langmuir, 2017. **33**(18): p. 4396-4406.